TOTAL ELECTRON CONTENT (TEC) VARIABILITY OF LOW LATITUDE IONOSPHERE AND ROLE OF DYNAMICAL COUPLING: QUIET AND STORM-TIME CHARACTERISTICS

By

Gebregiorgis Abraha

SUBMITTED IN PARTIAL FULFILLMENT OF THE
REQUIREMENTS FOR THE DEGREE OF
DOCTOR OF PHILOSOPHY
AT
ADDIS ABABA UNIVERSITY
ADDIS ABABA, ETHIOPIA
JANUARY 2014

© Copyright by Gebregiorgis Abraha, 2014

ADDIS ABABA UNIVERSITY
DEPARTMENT OF
PHYSICS

The undersigned hereby certify that they have read and recommend to the Faculty of Chemical and Physical Sciences for acceptance a thesis entitled "**Total Electron Content (TEC) variability of low latitude ionosphere and role of dynamical coupling: quiet and storm-time characteristics**" by **Gebregiorgis Abraha** in partial fulfillment of the requirements for the degree of **Doctor of Philosophy**.

Dated: January 2014

External Examiner: ______________________

Research Supervisor: ______________________
Dr Gizaw Mengistu

Examing Committee: ______________________

____

ADDIS ABABA UNIVERSITY

Date: **January 2014**

Author: **Gebregiorgis Abraha**

Title: **Total Electron Content (TEC) variability of low latitude ionosphere and role of dynamical coupling: quiet and storm-time characteristics**

Department: **Physics**

Degree: **Ph.D.** Convocation: **May** Year: **2014**

Permission is herewith granted to Addis Ababa University to circulate and to have copied for non-commercial purposes, at its discretion, the above title upon the request of individuals or institutions.

Signature of Author

THE AUTHOR RESERVES OTHER PUBLICATION RIGHTS, AND NEITHER THE THESIS NOR EXTENSIVE EXTRACTS FROM IT MAY BE PRINTED OR OTHERWISE REPRODUCED WITHOUT THE AUTHOR'S WRITTEN PERMISSION.

THE AUTHOR ATTESTS THAT PERMISSION HAS BEEN OBTAINED FOR THE USE OF ANY COPYRIGHTED MATERIAL APPEARING IN THIS THESIS (OTHER THAN BRIEF EXCERPTS REQUIRING ONLY PROPER ACKNOWLEDGEMENT IN SCHOLARLY WRITING) AND THAT ALL SUCH USE IS CLEARLY ACKNOWLEDGED.

This dissertation is dedicated for my Mother Tsehaynesh Zekarias regretfully she couldn't make the love gave to me ascertained in this educational achievement.

Table of Contents

Abstract

The low latitude ionosphere and its coupling to lower atmosphere such as (mesosphere, stratosphere and thermosphere)and high latitude ionosphere are investigated using observational and model data. The dominant modes of variability of low latitude ionosphere are linked to Equatorial Electrojet (EEJ), Counter Electrojet(CEJ) and Prereversal Enhancement(PRE). These are investigated using magnetometer data and EEJ models. The results of the analysis reveal that EEJ undergoes day and seasonal variations. From the daily variation analysis, the EEJ value at Addis Ababa sharply increases to its peak value from 9.00-13.00 LT and dies out around 18.00 LT. EEJ versus time graphs shows that the H-components of the magnetic field at Addis Ababa location varies by a factor of 2-4 times larger compared to Adigrat. Seasonally as both measurements and model data revealed, EEJ has significantly increased during E season compared to D and J seasons. Our observation also shows that counter CEJ are more frequent on solstices than equinoxes and on the contrary Morning Counter Electrojets (MCEJ) occurs more frequently on equinoxes than solstices. Apart from that the localized EEJ, CEJ and PRE, low latitude ionosphere is dynamically coupled to lower atmosphere and high latitude ionosphere that control both low latitude ionospheric dynamics and chemistry during both quiet and storm-time. In this regard, the storm-time low latitude ionospheric total electron content (TEC) variability and the influences of lower and high latitude ionsophere are investigated.

The TEC variation is characterized in relation to diurnal, seasonal, temporal, spatial and longitudinal behaviors. The diurnal characteristics of TEC can be explained in terms of the Diurnal, Semidiurnal,Terdiurnal and Quterdiurnal tides. The TEC

climatology from NeQuick and ionosonde is also compared during both quiet and geomagnetically disturbed days. Day time enhanced TEC value followed by night time depilation is a typical behavior of the ionosphere.

A geomagnetic storm occurred during January 22-25, 2012. The Disturbance storm time (Dst) values for the period shows that it is a moderate intensity geomagnetic storm. The geomagnetic storm is characterized by different indices and indicators. The Symmetric H component of ring current ($SYM-H$) value on January 22 shows a sudden increase to more than 50 nT at the Sudden Storm Commencement (SSC) and followed by sharp decrease to a value of -100 nT after which a recovering started. A second SSC on January 24 followed by a shock on January 25. These SSCs before the main storms on January 22 and 25 are evidences for the occurrence of Coronal Mass Ejection (CME). Moreover, the short recovery period, unlike that of Co-rotating Interaction Regions (CIR) driven geomagnetic storms, implies the geomagnetic storm is a CME-driven. The sudden jump of the solar wind dynamic pressure and the The southward Interplanetary Magnetic Field (IMF B_z) are also consistent with occurrence of CME. Our observational evidences of Proton fluxes of high energy ranges and increase in proton density are also other indicators for occurrence of CME. The high values Auroral Electrojet (AE) index on these dates implies ionospheric perturbation in response to the storm. This is also reflected in the Total Electron Content (TEC) change during the storm relative to quiet day TEC over the polar regions. The response of the ionospheric to geomagnetic storms is also investigated from amplitude modulation of wave components that account for the majority of TEC variance during the period. The diurnal and semidiurnal TEC variances account upto a maximum of 83% and 30% of the TEC variance over fairly exclusive ionospheric regions respectively. The diurnal variability dominates the subtropical latitude where the solar cycle is an important factor while the semidiurnal variance is limited to higher latitudes. The diurnal and semidiurnal TEC variances show hemispheric asymmetries. The stationary planetary waves also account for TEC variances that exceed semidiurnal TEC variance and exhibit hemispheric asymmetry

of opposite sign to diurnal TEC variance. These features of TEC variance are climatology of TEC variability irrespective of the storms. However, the impact of the geomagnetic storms are distinctly marked in the daily time series of amplitudes of diurnal and semidiurnal migrating tides and stationary planetary waves. The abrupt changes in amplitudes of diurnal (upto 5 TECU) and semidiurnal (upto 2 TECU) migrating tides are observed within the 20^oS-20^oN latitude band and along 20^oN respectively while that of stationary planetary wavenumber 1 is in the order of 3 TECU and is mainly localized along 20^oS.

Acknowledgements

I would like to express my sincere gratitude to my supervisor Dr Gizaw Mengistu who supported me, encouraged me and kept my sprints up all through my studies at Addis Ababa University, Ethiopia. His vast knowledge and experience shared will remain as base for my future research career. All his suggestions, comments, constant support and follow up during my research work and preparation of this dissertation was invaluable. I am also thankful to Dr Terry Bullett for the chance I got invitation from him to USA during the beginning of my research time and also expressed his interest in my work and supplied me some materials while I stayed with him in USA, which gave me a better perspective on my own results. My thanks goes to Dr Endawoke Yizengaw who provided me magnetometer data which are important to some of my results. I am highly indebted with Dr Lemi Demeyu and Dr Belayneh Mesfin, the former and current physics Department heads, for the opportunity they gave me to utilize research logistics. Special thanks to w/ro Tsilat Adnew the secretary of physics department for kind cooperation. The IGSSA people (Dr shemelis Fessaha, Dr Elias Lewi, Dr Atalay Ayele, Dr Getnet Mewa) were wonderful to me during my stay in Addis Ababa University and also they are helpful, positive and cooperative so they deserve a special thanks. I am grateful to acknowledge *Mekelle University*, for the consistent research fund support, which was crucial to the successful completion of this project. Of course, I am grateful to my parents for their patience and *love*. Without them this work would never have come into existence (literally).

Addis ababa, Ethiopia Gebregiorgis Abraha
May 20, 2014

Chapter 1

Introduction

Satellites, airline crews and passengers, pipelines, and electric power grids, are all susceptible to damage and degradation due to the harsh space environment [1, 2]. Over 500 operational satellites are currently orbiting the Earth. Many of these are commercial communications satellites that provide global news TV coverage, telephone connections, and credit card transactions. Governments operate many other satellites to provide weather images, navigational signals, land use information, and military surveillance. The basic interest in studying space weather is, therefore, primarily due to the rapid growth of commercial satellite communications, industry, and the development of continental-sized power and communication grids. With these developments, we have become more vulnerable to space weather storms through our reliance on high-tech information systems and our growing global interconnections. Most space weather effects affect the dynamics and composition of the ionosphere. The upper atmosphere, where most of the more energetic radiations are stopped, and which is heated by them , is is very responsive to solar activity variations as well as to the short-lived, intense and localized outbursts known as solar flair [3]. Therefore ionospheric plasma density is highly variable. Thus ionosphere is one of the main error sources in GPS positioning and navigation because radio frequencies are highly affected by electron density. Therefore it is important to understand the structure and composition of the ionosphere for the accurate prediction of space hazards.

The variability of the ionosphere can be monitored using space and ground based probing techniques. There are different techniques such as the global positioning system (GPS), which uses a linear combination of observable two frequencies to remove the effect for positioning. Another important method of probing technique is by broadcasting a range of frequencies, and measuring the time it takes for each frequency to be reflected. From this technique it is possible to estimate the concentration of free electrons and height of each ionized layer. For this purpose ionosonde is used. Ionosonde broadcasts a sweep of frequencies, usually in the range of 0.1 to 25 MHZ. As the frequency increases, each wave is refracted less by the ionization in the layer. So penetration of the wave continues further before it is reflected. As the wave approaches the reflection point, its group velocity approaches zero and this increases the time-of-flight of the signal.

GPS code and phase measurements can be processed inorder to estimate the TEC values. So the collected TEC values from GPS stations of Ethiopia and from global world data are compared with ionosonde data obtained from the newly installed ionosonde at welmera station near Addis Ababa and NeQuick data. The results of this comparison among these completely independent methods gives an indication of the GPS TEC accuracy. Magnetometers provide a magnetic field data and the data collected from magnetometers enables us to estimate EEJ, CEJ and the development of prereversal enhancements during post sunset time at dip magnetic equatorial regions.

The ionosphere is region of the upper atmosphere where electrons are in sufficient density to affect radio wave propagation. The electron density distribution over the this region is, therefore, very crucial for satellite communication and navigation systems. However, the distribution of these electrons over the ionosphere around the globe exhibits complicated longitudinal structure especially during increased solar activity. The equatorial plasma distribution is controlled by the neutral winds and electric fields. The neutral winds induce the hemispheric asymmetry of the ionosphere with respect to the magnetic equator, with large plasma flow (towards the hemisphere of stronger poleward wind) and stronger anomaly crest occurring in opposite hemispheres ([4] and references therein). The zonal electric field at the magnetic equator, being eastward during the day, creates a steady upward $E \times B$ plasma drift. This plasma rises until the pressure forces are high enough that it starts to slide down the magnetic field lines, assisted by gravity. This creates the ionization trough at the magnetic equator and plasma density enhancements (the EIA crests) at $\pm 15^o$ magnetic latitudes during geomagnetically quiet conditions (e.g. [5]). Just after sunset the eastward electric field is enhanced and the F-region plasma can drift to even higher altitudes leading to a phenomenon known as the fountain effect.

Ionospheric electron distribution is also affected by other geophysical process such as geomagnetic storms. Geomagnetic storms occur when there is a large sudden change in the solar wind dynamic pressure at the magnetopause. The geomagnetic Dst index is an excellent indicator of storm events. The main attribute of a magnetic storm is a clear decrease of the horizontal intensity of the magnetic field. The onset phase of a storm is often characterized by a short sudden increase of the Dst index [6]. During the main phase of geomagnetic storms, when the Interplanetary Magnetic

Field (IMF) turns southward and intensifies, the interplanetary electric field can penetrate to the low-latitude ionosphere for many hours without decay. The reconnection between southward IMF and the Earth's magnetic field leads to a strong dawn-to-dusk electric field which moves the equatorial F-region plasma upward enhancing the fountain effect: the fountain rises up to 800-1000 km altitude at the equator and covers about $\pm 30^o$ of Magnetic Latitude (MLAT). Solar photoionization replaces the uplifted plasma at lower altitudes, leading to an overall increase in the ionosphere total electron content (TEC) (e.g. [7, 8]). The phenomenon of the ionosphere dayside uplift due to super fountain effect (SFE) has been described for a number of intense geomagenetic storms (e.g.[9, 10, 11, 8, 12]) where the sudden drop of B_z IMF is observed in connection with a significant TEC increase above 715 km, exceeding 23 times the TEC level during geomagnetically quiet and/or moderate conditions. The disturbances in the ionospheric F2 region electron density are results of profound influences of geomagnetic storms. These disturbances could involve either enhancement or depletion in electron density depending on whether positive or negative ionospheric storms generate them. The enhanced magnetospheric energy and energetic particles input into the polar upper atmosphere during geomagnetic storms greatly modify the dynamic and chemical coupling processes of the thermosphere and ionosphere system, resulting in significant changes in electron density profile and total electron content (TEC). There is general consensus that negative ionospheric storms are possibly caused by changes in the thermospheric composition due to the heating of the thermosphere during the storms. One of the significant features of the negative phase is its equatorward propagation during the storm from auroral latitudes towards lower latitudes. In contrast, several mechanisms have been considered as possible sources for the ionospheric positive phases (e.g.[13]), which include the F2-layer uplifting due to vertical drift, plasma fluxes from the plasmasphere and downwelling as a result of the storm-induced thermospheric circulation [14]. The altered thermospheric circulation causes downwelling of the neutral species through constant pressure surfaces at low-middle latitudes equatorward of the composition disturbance zone, increasing the O density relative to N_2 and O_2. This increases NmF2 and TEC. The formation of positive phase can also be explained with the mechanism that at the time of geomagnetic storm during the sunlit hours the eastward electric field at the equatorial belt is suppressed. Due to this, the upward lift of plasma is reduced and positive phase developed at equator. Such type of increase is observed during main phase of storm (e.g. [9] and references therein).

At low latitudes, another important factor that influences storm-time behavior of ionosphere are electric field disturbances including prompt penetration electric field (PPE) and wind disturbance dynamo electric field (DDE). Under effects of the PPE and DDE, the equatorial ionization anomaly (EIA) can undergo drastic modifications resulting in large ionospheric disturbances at low latitudes. Occasionally, interplanetary electric field can continuously penetrate to the low latitudes ionosphere for many hours under storm conditions (e.g. [15, 16]). Dramatic changes in the ionospheric vertical TEC are observed owing to the intense disturbances electric field associated with magneto-ionosphere interactions [9]. The combined effects of wind field, the composition changes and electrodynamics make the ionospheric phenomena rather complex in this region. Several mechanisms may work together to produce the observed phenomenon and their relative importance may differ from case to case and phase to phase of the storm. For example, the propagation of negative and positive ionospheric storms is strongly determined by the thermospheric disturbance spreading speed. A large amount of energy is deposited in high latitudes during the storms and substorms, which can generate traveling atmospheric disturbances (TADs) in the thermosphere. The generated TADs propagate from high- to low-latitudes, even to the opposite hemisphere. The neutral winds perturbations associated with TADs can bring the plasma upward/downward along the magnetic field lines, resulting in ionospheric fluctuations, attracting attention from observation and model studies.

The low latitude ionosphere shows significant variations in structures with altitude, longitude, local time, season, solar cycle, and geomagnetic activities. Ionosphere-lower atmosphere coupling processes play significant roles in these variations. For example signature of planetary wave type oscillation (PWTO) observed in the ionosphere might be caused by different processes such as external forces like variations of solar and geomagnetic activity or are internally driven by vertically propagating waves from lower to higher altitudes. The drivers of atmospheric thermal tides is heating associated with absorption of solar radiation but the dynamics is determined by the coriolis and gravitational forces. The amplitude and phase of tides vary not only with local time but also with times such as annually, seasonally or even week to week [17, 18]. The Diurnal tide is the most prominent dynamics feature of the mesosphere and lower thermosphere (MLT) region. The MLT diurnal tide has migrating and non-migrating components. Migrating tides are produced by the effect of absorption of solar UV radiation by stratospheric ozone and tropospheric water vapor [18, 19] dominate at low-and mid-latitudes, and have zero or small amplitudes at high-latitudes originate primarily in the troposphere, The upward-propagating migrating tides control the large-scale dynamics of the upper mesosphere.

The ionospheric wind dynamo is considered as an important and the main mechanism in generation of ionospheric electric currents and fields. The disturbed ionospheric wind dynamo can be the generator of the equatorial ionospheric electric currents during geomagnetic storms in the aftermath of strong auroral heating. The magnetospheric electric field directly penetrating into the lowlatitude ionosphere can be another source of electric field. For instance, the disturbance electric fields could enhance the development or inhibition of the equatorial ionization anomaly. The positive and negative deviations during magnetic storms depend on the storm development phase. The large enhancement in foF2 values can be explained by the penetration of strong electric field at low latitudes [20]. The critical frequency foF2 at low latitudes were very different in periods when the B_z component turns to north (the quiet day conditions) and when B_z component turns on south (the main phase of magnetic storms). The ionospheric response to these storms are related to the changes in Dst index and B_z component of the interplanetary magnetic fields. The magnetic storm induced variations depend on the growth of ring current in the main phase of the storms. There is a uniform relationship between the solar events like solar flares, CME's and interplanetary disturbances. The IMF B_z is the most important parameter for the generation of geomagnetic storms, as the energy input into the magnetosphere depends on B_z orientation and its magnitude. About 90% of intense and very intense magnetic storms are found to be caused by intense southward turning of B_z with the interplanetary shocks.

In quiet conditions the B_y component of the electric field which participates in the $E \times B$ drift is eastward. In most cases during magnetic disturbances B_y decreases at the equatorial zone and that leads to a reduction of the downward drift and so to the positive phase. However, during severe disturbances there may happen an increase in B_y with corresponding increase in the downward drift and corresponding negative phase [21, 22]. However, analyzing a very strong storm of November 6, 2001 (Dst-min = -300 nT), [23] showed that NmF2 temporary decreases in response to the penetration of the eastward electric field before beginning to increase. At the same time, TEC started to increase almost immediately. Jin and Maruyama [24] investigated possible mechanisms of this effect using numerical simulation. They showed that the effect in NmF2 could occur under the electric field magnitude greater than several $\frac{mV}{m}$ and is caused by two processes accompanying the uplifting of the F2-peak: increased diffusion fluxes in the topside ionosphere and the plasma motion under the $E \times B$ drift. The TEC increase was attributed to the extra plasma production below the uplifted F2-layer peak.

In the conventional scenario of ionospheric storms, the negative storm phases with plasma density decreases are caused by neutral composition changes, and the positive storm phases with plasma density increases are often related to atmospheric gravity waves. However, recent studies show that the global redistribution of the ionospheric plasma is dominated primarily by electric fields during the first hours of magnetic storms. Storm-time electric fields have significant effects on the redistribution of the global ionospheric plasma. An eastward electric field will move the dayside ionospheric plasma to high altitudes with lower recombination rate, resulting in increases of the plasma density. Huang et al [25] use this mechanism to explain the generation of a positive ionospheric storm at middle latitudes. The numerical simulations of [26], using the ionospheric model SAMI2, have successfully reproduced the positive storm and verified the interpretation of [25]. On the other hand, neutral wind disturbances can cause similar changes in the ionospheric electron density. Enhanced storm-time Joule heating in the auroral zone launches atmospheric gravity waves that travel to low-latitudes. The equatorward traveling atmospheric waves move the ionospheric plasma particles upward along the magnetic field lines and result in increases of the electron density. When atmospheric waves reach the equatorial region, the disturbance wind dynamo will produce electric fields and cause electron density perturbations.

The ionosphere response to the moderate geomagnetic storms of 22-25 January 2012 and the spatio-temporal variability of this response such as TEC enhancement is another scientific problem addressed in the dissertation. The geomagnetic storms are first characterized using various indices and indicators. The collective ionospheric response is then also assessed based on various indices. The impact of the storms on the dominant coherent spatio-temporal variations of ionospheric TEC is investigated. In this regard, the modulation of the diurnal and semidiurnal tides in TEC which account for much of the TEC variation is analyzed.

The main objective of this work is to investigate the low latitude ionosphere and its coupling to lower atmosphere and high latitude ionosphere using observational and model data. The dominant modes of variability of low latitude ionosphere are linked to equatorial electrojet, counter electrojet and prereversal enhancement. The other objective of this study is to investigate the ionospheric diurnal, seasonal, spatio-temporal variability of the low latitude ionosphere using observational GPS data. Apart from this the NeQuick electron density is compared with ionosonde electron density for both quiet and disturbed days. The equatorial electrojet, its counter electrojet, the prereversal enhancement mechanisms and seasonal dependence of the electrojet are also analyzed in chapter 6.

The dissertation is structured as follows. Chapter 1 covers introduction on background of existing understanding and problem definition of the research; chapter 2 highlights basics of ionospheric physics; chapter 3 gives description of available ionosphere probing techniques while chapter 4 describes various data and methodologies used in the dissertation; and chapter 5 assesses the capacity of a climatological TEC NeQuick model by comparing with recently installed ionosonde at Addis Ababa. Chapters 6-8 cover investigation of EEJ, CEJ, and PRE and geomagnetic storms and dynamical coupling prevalent during the storm, and conclusions respectively.

Chapter 2

Physics of the ionosphere

2.1 What is the need to study the ionosphere?

The rapidly varying ionospheric currents cause rapid time variation in the magnetic field on the surface of the earth as well as on the upper atmosphere at different levels. The change in geomagnetic field in turn induces a current according to Faraday's law and is given by: $\frac{\partial \vec{B}}{\partial t} = - \bigtriangledown \times \vec{E}$. When these currents flow in man made conductive networks they are called magnetically induced currents and these induction effects can felt in gas pipelines buried underground and under sea telecommunication cables power grids and can damage these systems. We can imagine our world with out electricity, the society depends on electricity for everything such as communication, banking and business transaction to basic necessities like food and water. One serious fact to the reliability of electric power is geomagnetic storm, which induces huge current fluctuation in the upper atmosphere. This current induces magnetic flied in the surrounding space and this in turn modifies the intensity of the magnetic field of the earth. This modification by itself is resulted in producing additional current to trigger voltage fluctuation in transformers. The ionospheric current fluctuations can be measured using ground and space based magnetometers.

The other important thing we need to study the ionosphere is, the ionosphere, the ionized part of the atmosphere, affects modern technologies such as civilian and military communications, navigation systems and surveillance systems, etc. For many communication and navigation systems, this arises because the systems use signals transmitted to and from satellites, which must therefore pass through the ionosphere. For the most reliable communication and navigation it is necessary to correct the signals for effects imposed by the ionosphere. To do that the properties of the ionosphere, such as its variability with respect to magnetospheric disturbance, time of day, season of the year, and solar cycle variability must be well understood using different observing techniques. Radio wave propagation is modified in a number of ways by the effects of the integrated electron density along the ionospheric ray path between the satellite and the receiver, the total electron content (TEC). In consequence, TEC is a key parameter in the description of the impact of the ionized atmosphere on the propagation of radio signals. Therefore, understanding the variability of TEC is crucial for the operation of many applications, including navigation satellite systems like Global Positioning System (GPS), Global Navigation Satellite System (GLONASS). TEC can be measured by a number of essentially standard techniques, including Faraday rotation, group delay, and dispersive carrier phase. The TEC estimation technique from GPS satellite signal group delay and dispersive carrier phase advance is the popularly used method. Therefore, using data from both ground-based GPS receivers and the GPS receivers on Low Earth Orbit (LEO) satellites, GPS TEC measurements become one of the best for observing the entire vertical extent of the ionosphere (i.e. both the bottomside and topside ionosphere), especially for correcting satellite navigation systems. The Incoherent scatter RADAR, SUPPERDAN radar, and ionosondes measurements are also important ionospheric observations, mainly the bottom side ionosphere.

2.2 Structure and composition of the ionosphere

Ionosphere is the region of the upper atmosphere where free electrons occur in sufficient density to have an influence on the propagation of radio frequency electromagnetic waves. Its ionization mostly depends on activity of the sun. Its density varies according to the sunspot cycle, the season, and global locations polar, auroral zones, mid-latitudes, and equatorial regions. Most of its ionization is produced by x-ray and ultraviolet radiation from the sun. As earth rotates, ionization increases in the sunlit atmosphere and decreases on the shadowed side. Fig. 2.1 represents an ideal ionosphere formation during day time. The ionospheric electron density N at a given altitude and location depends on the solar EUV fluxes, the neutral composition, and dynamical effects of neutral winds and electric fields. In a region extending from a height of about 50 km to over 600 km, some of the molecules of the atmosphere are ionized by radiation from the Sun to produce an ionized gas. This region is called the ionosphere. Ionization is the process in which electrons, which are negatively charged, are removed from (or attached to) neutral atoms or molecules to form positively (or negatively) charged ions and free electrons. The plasma parameters in the earth's ionosphere display a marked variation with altitude, latitude, longitude, universal time, season, solar cycle, and magnetic activity. This variation results not only from the coupling, time delays, and feedback mechanisms that operate in the ionosphere-thermosphere system, but also from the ionosphere's coupling to the other regions in the solar-terrestrial system, including the sun, the interplanetary medium,

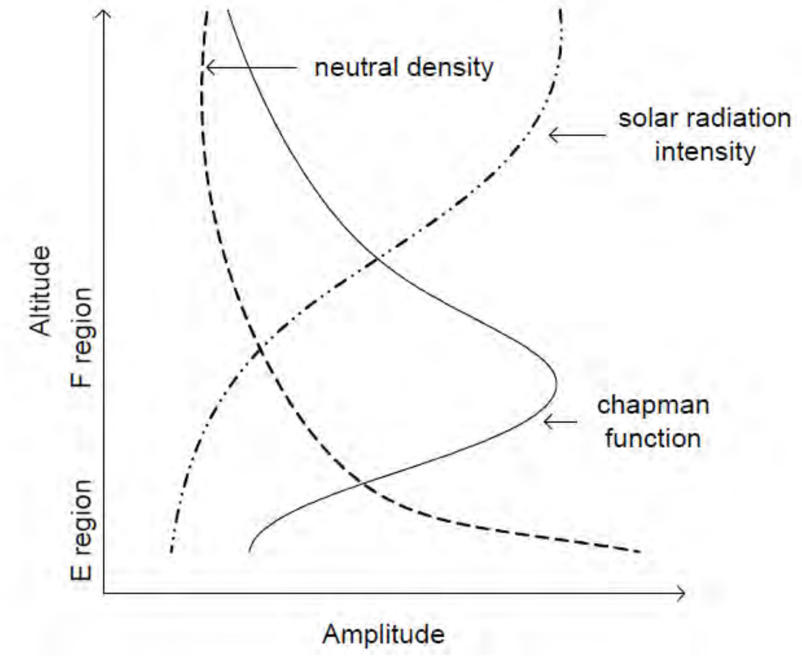

Figure 2.1: Ionosphere formation

the magnetosphere, and the mesosphere. The primary source of plasma and energy for the ionosphere is solar EUV, UV, and X-ray radiation; but magnetospheric electric fields and particle precipitation also have a significant effect on the ionosphere. The strength and form of the magnetospheric effect are mainly determined by the solar wind dynamic pressure and the orientation of the interplanetary magnetic field (IMF). Also, tides and gravity waves that propagate up from the mesosphere directly affect the neutral densities in the lower thermosphere, and the variation of these waves then affects the plasma densities. The different external driving mechanisms, coupled with the radiative, chemical, dynamical, and electro-dynamical processes that operate in the ionosphere, act to determine the global distributions of the plasma densities, temperatures, and drifts. The net value of free ions and electrons in the ionosphere is determined by the rate at which specific species of ions recombine with electrons to form neutral atoms through a process called recombination. In the process two types of recombination are involved.

i. Radiative recombination in which electrons combine directly with ions to form neutral atoms and emitting a photon to conserve energy and momentum:

$$X^+ + \bar{e} = X + h\nu \text{ eg. } O^+ + \bar{e} = O + h\nu$$

ii. The other possibility of reducing free electrons and ions is dissociative recombination which is a two stage process. In the first stage ions interact with neutral molecule replacing one of the atoms in the molecule and forming neutral atom and positively charged molecular ion

$$X^+ + Y_2 = XY^+ + Y \text{ eg. } N^+ + O_2 = NO^+ + O$$

In the second stage, electrons combine with the newly formed molecular ions, forming two neutral atoms

$$XY^+ + \bar{e} = X + Y \text{ eg. } NO^+ + \bar{e} = N + O$$

The dissociative recombination rate is about 1000 times faster than that of radiative recombination because the molecular ions have shorter lifetime than atomic ions. Due to this fact production is rapidly reduced at night and reduces plasma concentration. During the night time the O+ ion survives at higher altitudes and that is why night time communication is possible [27]. In the ionosphere different gas atoms and molecules are more abundant in some regions of the neutral atmosphere than others so ionization and recombination of these different species result in different electron density structures which form different layers. The layers are called D, E and F

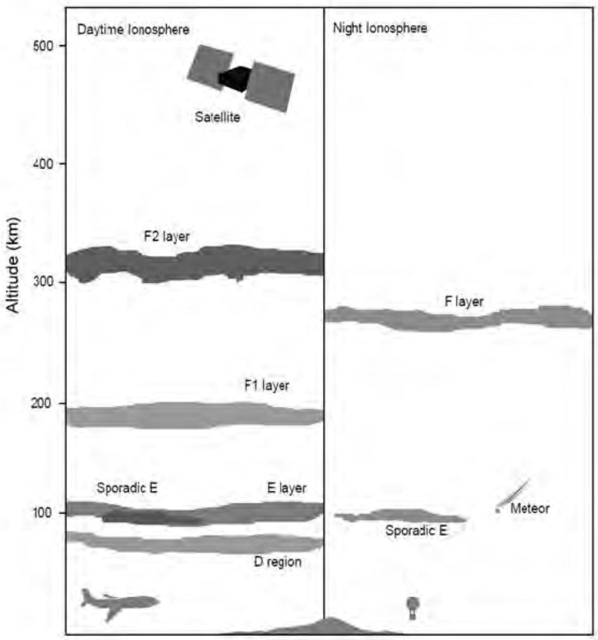

Figure 2.2: Day and night structure of the ionospheric layers

regions (see Fig. 2.2). The vertical structure of the ionosphere is governed by two equilibrium conditions, photochemical equilibrium and diffusive equilibrium, which play a vital role in the formation of the ionospheric regions at different heights. The E and $F1$ regions are formed due to chemical equilibrium, while the topside region of the ionosphere is due to diffusive equilibrium, and the $F2$ region is a transition between these two equilibriums.

2.3 Chapman production function theory

The generation mechanism of the ionosphere theoretically for the first time was described by Sydney Chapman. In his theory there are a number of simplifying assumptions that are made to make the problem tractable. The assumptions made in his work are described as follows:

1. The source of ionization is photo-ionization by absorption of solar radiation. This radiation is modeled as having as a single value for absorption cross-section and absorbing atmospheric gas is assumed to have a single constituent which is planar, horizontally stratified and in hydrostatic equilibrium. The vertical profile of the neutral gas obeys the equation given by $n_x(h) = n_0 \exp - \frac{h-h_0}{H_n}$ where n_0 is the neutral density at a reference height h_0 and $H_n = \frac{kT_n}{m_n g}$ is the exponential scale height of the neutral gas;

2. Chapman theory avoids the complex nature of the radiative transfer of energy through the neutral gas folding all photon details in to the photon absorption cross-section σ and using the ionization probability η to convert the energy absorbed in to the number of electrons released from the neutral gas. The rate of electrons per production q a given by Eq. (2.3.1)

$$q = \eta \sigma n_e I \tag{2.3.1}$$

where I is the intensity of radiation. The intensity of radiation depends on the line of sight (s):

$$-\frac{dI}{ds} = \sigma n_n I \tag{2.3.2}$$

It is also known that electron density is proportional to the rate at which radiation is absorbed:

$$q = -\eta \frac{dI}{ds} \tag{2.3.3}$$

Production rate reaches maximum, so differentiating Eq. (2.3.1) becomes

$$\frac{dq}{ds} = n\sigma(n_e \frac{dI}{ds} + I \frac{dn_e}{ds}) = 0 \tag{2.3.4}$$

The height h and the line of sight s can be related as

$$\frac{dh}{ds} = -\cos\chi \tag{2.3.5}$$

Therefore

$$\frac{1}{n}\frac{dn}{ds} = -\frac{1}{n}\frac{dn}{dh}\cos\chi \tag{2.3.6}$$

For the peak or maximum production we have

$$\sigma H n_m \sec\chi = 1 \tag{2.3.7}$$

or

$$\sigma N_{mn} = 1 \tag{2.3.8}$$

where N_{mn} is the integrated peak density and is given by $N_{mn} = \int_{\infty}^{s_m} n_n ds$ along the limit of sight up to the position of the peak s_m. The ionization radiation is described by the optical depth τ and arises naturally in the expression for intensity at position s along the line of sight relative to the intensity at infinity. Therefore the intensity can be obtained from Eq. (2.3.2) and rearranging this and integrating we have:

$$\ln(\frac{I(s)}{I(\infty)}) = -\sigma\int_{\infty}^{s} = -\sigma N_n s \tag{2.3.9}$$

or

$$I(s) = I(\infty)\exp(-\sigma N_{ns} = I(\infty)\exp(-\tau) \tag{2.3.10}$$

At the peak, $\sigma N_{ns} = \sigma Nnm = 1$; so the peak is the altitude where the optical depth is unity. Now we return to the analysis of the production rate q. The peak production rate is

$$q_m = C\sigma n_m Im = C\sigma(C\sigma H\sec\chi)^{-1} I(\infty)\exp(-1) = \frac{CI(\infty)\cos\chi}{H\exp(1)} \tag{2.3.11}$$

Given the neutral-gas altitude profile $n_n = n_0 \exp(\frac{-(h-h_0)}{H})$, we can determine the height of production peak h_m by writing

$$\sigma H n_m \sec\chi = 1 = \sigma H n_0 \exp(-(\frac{(h_m - h_0)}{H}) \sec\chi \tag{2.3.12}$$

solving for h_m we can determine the dependence of the radiation intensity I on h by using the earlier expression for I(s) and noting that N_{ns} is the integrated density along the line of sight:

$$I(h) = I(\infty) \exp[-\sigma n_0 H \sec\chi \exp(-\frac{h_m - h_0}{H})] \tag{2.3.13}$$

so the dependence of the production rate q on h is given by

$$q = C\sigma n_n I = C\sigma n_0 I(\infty) \exp[-\frac{(h-h_0)}{H} - n_0 \sigma H \sec\chi \exp(-\frac{(h-h_0)}{H})] \tag{2.3.14}$$

With the value of $CI(\infty) = q_{max} \frac{\exp 1H}{\cos\chi}$, Eq. (2.3.14) can be written as:

$$q = q_m \exp[1 + \frac{h_m - h}{H} - \exp(\frac{(h_m - h)}{H})] \tag{2.3.15}$$

We can also show the following relation

$$\frac{h_m}{H} = \frac{h_{m0}}{H} + log(\sec\chi) \tag{2.3.16}$$

where h_{m0} is the maximum of production at overhead sun. Using $q_{m0} = \frac{q_m}{\cos\chi}$ and $z = \frac{h-h_{m0}}{H}$ we have:

$$q(h) = q_{m0} \exp(1 - z - \exp(-z)) \tag{2.3.17}$$

This describes the rate of production [28, 29]. In a steady state and if plasma transport is neglected, the electron continuity equation is reduced to $q_e = L_e = \alpha n_e^2$. An α function is employed in this case since the loss of ionization content is assumed to behave quadratic in the E region ionosphere which is initially rich in molecular gases but also a small percentage of atomic constituents of the neutral atmosphere. Now if we solve n from $q_e = \alpha n_e^2$, and insert the value of q from Eq. (2.3.17) in to the value of n, the electron density profile becomes

$$n_e(h) = n_{mE} \exp(\frac{1}{2}(1 - z - \sec\chi exp(-z))) \tag{2.3.18}$$

where $n_{mE} = \sqrt{\frac{q_{m0}}{\alpha}}$ is the E region peak density. This is the plasma density function describing the vertical zenith and angle dependence of densities when the plasma is in photochemical equilibrium.

2.3.1 The D-layer

The D layer ranges from about 50 km to 90 km altitude above the earth. This region is the weakest region in terms of electron density distribution. Ionization is due to the layman alpha-hydrogen radiation at 121.5 nm ionizing nitric oxide. At high solar activity periods hard X-ray ($< 1nm$) ionize N_2 and O_2 in this region. The maximum electron density at noon reaches $1.5 \times 10^4 cm^{-3}$. Due to high rate of recombination rates in this region and low net ionization, high frequency radio waves are not reflected by the layer. The D-region is mainly responsible for HF absorption around 10 MHz and the absorption is higher at day time than night time. This layer greatly diminishes after sunset, but remains due to galactic cosmic rays.

2.3.2 The E-layer

The E-layer ranges from 90 km up to 140 km and the peak value of the electron density at day time is about $1.5 \times 10^5 cm^{-3}$ and less than $10^4 cm^{-3}$ during night time. The E region is dominated mainly by ionized molecular oxygen (O_2^+) and NO+.

Ionization of the E layer is due to soft X-rays (1-10 nm) range and ultraviolet (UV) solar radiation in the range 100 - 150 nm range. While night time electron density exists due to electron and meteor bombardment. Sometimes sporeadic E is observed during day time but sporeadic E is not common to see in the night time.

2.3.3 The F-layer

The F region is the uppermost of the ionospheric regions and stretches from 140 km upwards, although current convention is to use the term ”ionosphere” to refer to the region up to 1000 km altitude and the term ”plasmasphere” to refer to the region of ionization above 1000 km. The F1 and F2 layers are the sub-component layers of the F layer.

2.3.4 The F1-layer

The F1 layer is a daytime phenomenon and forms in the altitude range 140 to 210 km. The free electron density is about 10 times that of the normal E region. Most radio waves propagating at oblique incidence that can penetrate the E region can also penetrate the F1 layer, so it has little effect on radio communications. The F1 layer peaks at 210 km with noon peak electron density of $2.5 \times 10^5 cm^{-3}$, and disappears at night when combining with F2 layer to form the night time F layer. Ionization of atomic oxygen (O) by Lyman continuum or by He emission lines is probably accompanied by N_2 ionization which disappears after sunset. Most of the ionization is in a molecular form and disappears by dissociative recombination.

2.3.5 The F2 layer

The F2 layer is the highest layer in the ionosphere and also, normally, has the highest free electron density. This enhanced free electron density in spite of the fact that the extremely low density of the atmosphere at these heights means that the recombination rate is reduced significantly. However, even though the rate of ionization production is very low in the F region and is decreasing with height, the loss due to recombination decreases even faster with height. The end result is that the electron density increases with height until diffusion becomes dominant, causing the electron density to then decrease with height, and hence the F2 peak is formed at about 300 km with peak electron density values of $10^6 cm^{-3}$ at noon and $10^5 cm^{-3}$ at night times. The F2 layer's height and electron density is highly variable and large daily, seasonal and sunspot cycle variations are combined with the general behavior. Ionization is due to extreme ultraviolet radiation (EUV) (10-100 nm) solar radiation of atomic oxygen (O).

2.3.6 The topside region and the protonosphere

The topside ionosphere is the region above the $F2$ peak extended from about 600-1000 km where the atomic Oxygen is dominant. In this region transport processes are the principal processes but production and loss are insignificant because the decrease in intensity of neutral particles increases diffusion processes. The electron density decreases exponentially with altitude in this region. Above the topside region, the region where lighter ions (H^+ and He^+)dominate is called the plasmasphere or protonosphere. This region is fully ionized region.

2.4 Ionospheric variations

The sun is the main source of ionization energy in the ionosphere. The ionosphere naturally varies with time of day, season and geographic position. The following major variation are discussed in brief.

2.4.1 Diurnal variation

The day and night electron density of the ionosphere is not the same. Night tine electron densities are much lower than day time electron density because in night time the recombination rates are higher in the absence of ionization sources. The day time electron density reaches its peak value at noon hours.

2.4.2 Seasonal variation

The ionosphere exhibits strong seasonal and solar cycle variations because the main source of ionization and energy for the ionosphere is photo-ionization. Therefore, whenever there is a change in solar zenith angle or the solar radiation fluxes, the ionosphere will change. The ionosphere's seasonal variation is related to a solar zenith angle change, while its solar cycle variation is related to a change in the solar EUV and X-ray radiation fluxes. However, the ionospheric variations are not always simple because the ionosphere is closely coupled to the thermosphere, which also undergoes seasonal and solar cycle changes. For example, Lee et al [30] during the solar cycle 23, investigated that large daytime electron density in winter than in summer called the seasonal anomaly which occurs mainly at midlatitudes and is more pronounced in the northern hemisphere than in the southern hemisphere. This phenomenon, which is called the seasonal anomaly, occurs because of the seasonal changes in the neutral atmosphere. Specifically, the summer-to-winter neutral circulation results in an increase in the O/N_2 ratio in the winter hemisphere and a decrease in the summer hemisphere. The increased O and decreased N_2 densities in winter act to increase the O+ densities, due to the relative increase in the production rate and decrease in the loss rate. This effect is more than enough to offset the tendency for decreased O+ densities due to a larger solar zenith angle. The net result is that the O+ densities in winter are larger than those in summer at F region altitudes. In turn, the higher electron densities in winter result in lower electron temperatures, which show the inverse relationship between the electron density and temperature. Also, it should be noted that the neutral helium density displays a strong seasonal dependence and this leads to a seasonal dependence for He+. According to the Chapman ionization theory, n_e in the ionosphere should behave in a way that is controlled by the solar zenith angle; that is, for the seasonal variation, n_e should be greater in summer than in equinox, and smallest in winter. However, previous studies have revealed some interesting "anomalous" features, which are quite different from the prediction of the Chapman ionization theory. Historically, when the behaviors of the F2 layer were significantly deviated from the solar zenith angle dependence as the Chapman ionization theory predicted, they were called "anomalies." Typical anomalies in the F2 layer n_e are the so-called seasonal anomaly or winter anomaly (that the daytime values of mid-latitude peak n_e of the F2 layer, NmF2, are greater in winter than in summer), annual anomaly or non seasonal anomaly (take the Northern and Southern hemispheres as a whole, NmF2 in December is greater than in June at both daytime and night), semiannual anomaly (greater NmF2 at equinox than at solstice), equatorial ionization anomaly (EIA, the equatorial anomaly is within approximately $\pm 20^0$ of the magnetic equator ([31] and references therein)

2.4.3 Latitudinal variations

The diurnal and seasonal behaviors observed the sun's position relative to the atmosphere plays significant role in latitudinal variation in the ionospheric electron density because the solar zenith angle (χ) measured from the observer's local vertical to the sun determines the intensity of ionization. This shows that as the solar zenith angle becomes smaller the ionosphere exposes to higher radiation rates and ionization becomes larger. For example the sun's zenith angle at the tropic of capricorn ($23.5^0 S$) at noon on March, southern Autumn equinox will be 47^0 with expected lower ionization rates and electron densities than at the tropic of cancer when the sun will be vertically overhead ($\chi = 0$)

2.4.4 Ionospheric variability due to geomagnetic storms

Technology dependence has become increasingly vulnerable to adverse space weather. These adverse conditions are represented by power failures due to geomagneticaly induced currents in power lines, failures in communications and GPS guided air craft navigation and landing systems. To a large extent the study of geomagnetic storms in the equatorial and mid latitude regions of the African sector are not yet understood well. Ionospheric storms represent an extreme form of space weather with important effects on ground-and space-based technological systems. Geomagnetic storms are developed when the ring currents are intensified. As we know the total field is given by $F_T = F_M + F_I - F_R$. Where F_M is the main field due to the rotation of the outer liquid core plus anomaly fields of earth's lithosphere, F_I is field due to the ionospheric Sq currents and F_R is the field due to ring current. So when the ring current is intensified, the total field decreases and geomagnetic storm is occurred. Geomagnetic storms are major disturbances of the magnetosphere that occurs when the interplanetary magnetic field turns southwards and remains southwards for a prolonged time. The turning of the interplanetary magnetic field to the northward direction restores to its prestorm state. These phenomena are driven by highly variable solar and magnetospheric energy inputs to the earth's upper atmosphere, which continue to provide a major difficulty for attempts now being made to simulate the detailed storm response of the coupled neutral and ionized upper atmospheric constituents using increasingly sophisticated global first principle physical models. Several major programs for coordinated theoretical and experimental study of these storms are now underway. These are beginning to bear fruit in the form of improved physical understanding and prediction of ionospheric storm effects at high, middle, and low latitudes. Large geomagnetic storms are usually caused structures in the solar wind having specific futures such as long duration of strong southward interplanetary magnetic field (IMF) impinging on the earth's magnetosphere which cause geomagnetic disturbances or coronal mass ejections (CMEs), an eruptive solar phenomena in which huge amount of plasma about $10^{15}g$ and magnetic energy about $10^{32} - 10^{33}erg$ are ejected by the sun at high speed reaching more than 1000 km/s. Geomagnetic storms, in which the global geomagnetic field intensity decreases on the order of tens to hundreds nT, are large scale phenomena in the solar wind-magnetosphere-ionosphere coupling. Geomagnetic storms develop when solar wind-magnetosphere couplings are intensified by solar wind disturbances coming out through coronal holes and coronal mass ejections

(CMEs). Basically there are two major types of storms: CME driven geomagnetic storms and CIR driven geomagnetic storms. The geomagnetic storms driven by both are not the same. The characteristics of the storms driven by both CME and CIR are not the same type. The storm driven by the fast CMEs are usually very intense with $Dst < -100nT$, while the storm driven by CIRs are usually weaker and their main phase has irregular profile and long recovery phase lasting many days to weeks and cause high intensity long duration continuous activity. Magnetic storm starts with sudden increase of the intensity of the geomagnetic field horizontal component, called Storm Sudden Commencement (SSC). The southward interplanetary magnetic field reconnection in the day side magnetosphere, rapidly injecting magnetic field and particle energy into the earth's magnetosphere and modifying the large scale ring current system. As a result of reconnection, it leads to aurora formation, geomagnetic storm phenomena, and enhanced ring current system. A number of studies have shown that the magnitudes and different phases of geomagnetic storms depend on solar wind speed, enhanced ring current, the magnitude of the interplanetary magnetic field, and the direction of the interplanetary magnetic field. Few concepts are presented to facilitate understanding what causes geomagnetic storms and ionospheric disturbances.

Coronal mass ejections

Coronal mass ejections (CMEs) are tremendous amount of bubbles of electrified gas that streaming away from the sun. They can carry as much as 10 billion tons of solar material and usually travel at speeds between 500 and 1500 km/s, taking 2 or 3 days to cross the 150 million km which is the distance between sun and earth. CMEs can occur at any time during the solar cycle, but increase in daily frequency from about 0.5 during solar minimum years to about 2.5 around solar maximum. Fast CMEs, those which outpace the ambient solar wind, give rise to large geomagnetic storms when they encounter the earth's magnetosphere [32]. Such storms can result from the passage either of the CME itself or of the shock created by the fast CME's interaction with the lower-moving solar wind. Geomagnetic activity associated with CMEs can dramatically disrupt electrical and communications systems. CMEs can create voltage surges in electric power grids, disrupt radio communications and navigation systems, prevent normal satellite operations, and threaten the safety of astronauts [2, 1]. In 1997, for example, a geomagnetic storm shut down a satellite that provided television broadcasts. In 1998 another storm disrupted a Galaxy IV satellite that supported automated cash machines and airline tracking systems. Geomagnetic storms are also known to affect mobile phone operations and wireless internet services. CMEs may be accompanied by X-rays, EUV and radio bursts. The importance of X-ray flare peak is indicated by a class number with each class assigned according to the flux (E) measured in the 0.1-0.8nm range by the Geostationary Operational Environmental Satellite (GOES). The major class definitions are

- C-class: $10^{-6}W.m^{-2} < E < 10^{-5}W.m^{-2}$;
- M-class: $10^{-5}W.m^{-2} < E < 10^{-4}W.m^{-2}$; and
- X-class: $E > 10^{-4}W.m^{-2}$

Solar wind and the interplanetary magnetic field

The region between the sun and the planets has been termed the interplanetary medium. Although once considered a perfect vacuum, this region is extremely turbulent and dominated by the solar wind. The solar wind is a plasma of charged particles coming out of the sun in all directions at very high speeds (250-1000 km/s, i.e., about 600,000-2,000,000 miles/hour). It varies with the changing conditions on the sun. The solar wind is responsible for the anti-sunward tails of comets and the shape of the magnetic fields around the planets. It can also have significant effects on the flight paths of spacecraft. The earth's magnetic field is very similar to the pattern formed when iron filings align around a bar magnet. Under the influence of the solar wind, however, these magnetic field lines are compressed in the sunward direction and stretched out in the downwind direction. This creates the magnetosphere, a complex, teardrop-shaped cavity around earth. The Van Allen radiation belts are within this cavity, as is the ionosphere, a layer of earth's upper atmosphere where photoionization by solar x-rays and extreme ultraviolet rays create free electrons. The earth's magnetic field senses the solar wind by its speed, density, and magnetic field strength. Since the solar wind varies over time scales as short as seconds, the interface that separates interplanetary space from the magnetosphere is very dynamic. Normally this interface, called the magnetopause, lies at a distance of about 10 earth radii in the direction of the sun. However, during periods of elevated solar wind density or velocity, the magnetopause can be pushed inward to within about 6.6 earth radii. As the magnetosphere extracts energy from the solar wind the internal processes produce geomagnetic storms.

Ring current

Electrically charged particles trapped in earth's magnetic field experience an equatorial drift motion resulting in westward flowing ring current in the equatorial plane. The ring current is one of the major current systems in the earth's magnetosphere. It circles the earth in the equatorial plane and is generated by the longitudinal drift of energetic (10 to 200 keV) charged particles trapped on field lines between $L \sim 2$ and 7. Basically the interconnection between southward interplanetary magnetic field and earth's magnetic field leads to strong dawn-to-dusk electric fields and this overall increase in magnetosphere convection and causes intense ring current buildup and storms [33]. During geomagnetic storms, ring current particle fluxes are dramatically increased, with the peak enhancements occurring in the inner ring current (at $L < 4$). The quiet-time ring current consists predominantly of H+, while the storm-time ring current also contains a significant component of ionospheric O+, whose contribution to ring current energy density may even exceed that of H+ for brief periods near the maximum of particularly intense storms. The formation of the storm-time ring current has been attributed to two different processes: (i) the injection of plasma into the inner magnetosphere during the expansion phase of magnetospheric substorms and (ii) increased convective transport of charged particles from the nightside plasma sheet deep ($L < 4$) into the inner magnetosphere as a result of an intensification of the earth's dawn-dusk convection electric field during extended periods of strong southward IMF. The present understanding of ring current formation tends to favor the enhanced convection model over the substorm plasma injection model; however, it is recognized that substorms, while not the primary driver, nonetheless play a significant role in the growth of the storm-time ring current (e. g., by energizing ions in the near-earth plasma sheet prior to their transport into the ring current). The storm-time growth of the ring current lasts from 3 to 12 hours and constitutes the ”main phase” of a magnetic storm. Following this main phase, the ring current begins to decay, returning to its pre-storm state in two to three days. Full recovery can require as long as a month in the case of major geomagnetic storms. During the storm recovery phase, particle transport into the ring current slows, allowing various loss processes to reduce ring current particle fluxes to their quiet-time level. The primary loss process during both the main and recovery phases is charge exchange with neutral hydrogen atoms in the geocorona. The storm level of geomagnetic storms can be characterized using different geomagnetic indices.

Disturbance storm time index

The Dst is a geomagnetic index which monitors the world wide magnetic storm level. It is constructed by averaging the horizontal component of the geomagnetic field from mid-latitude and equatorial magnetograms from all over the world. Negative Dst values indicate a magnetic storm is in progress, the more negative Dst is the more intense the magnetic storm. The negative deflections in the Dst index are caused by the storm time ring current which flows around the earth from east to west in the equatorial plane. The ring current results from the differential gradient and curvature drifts of electrons and protons in the near earth region and its strength is coupled to the solar wind conditions. Only when there is an eastward electric field in the solar wind which corresponds to a southward interplanetary magnetic field (IMF) is there any significant ring current injection resulting in a negative change to the Dst index. Thus, by knowing the solar wind conditions and the form of the coupling function between solar wind and ring current, an estimate of the Dst index can be made.

The planetary K_P index

The planetary K_p index is derived using an average of the horizontal component of the magnetic field (H) or D-component (if D is more disturbed than H) observations from a network of geomagnetic observatories distributed around the glob located between 48^0 and 63^0 geomagnetic latitude. The three hourly K_p provides a measure of magnetic deviation from the regular daily variation during the three hour period [34]. The information about magnetic activity is provided through a semi-logarithmic numerical code that varies from 0 to 9, with the different numbers corresponding to different magnetic activity levels.

The Solar quiet (Sq) current system and the dynamo electric field

The Sq current is driven by solar EUV radiation, not only produces the ionization in the E region but also heats the atmosphere and produces winds. Geomagnetic field measurement show that a regular daily variation in magnetic field of the ionosphere as first studied by Schuster [35], arises due to the ionospheric wind dynamo. The Sq current typically extends from 90 km to 200 km, but it maximizes at about 150 km where Pedersen current maximizes. How this occurs is important when discussing the development of the equatorial electrojet [36, 37].

On the earth's sun lit side, solar radiation heats the thermosphere near the equator causing it to expand so that there exist a local high pressure at the equator due to expansion and lower pressure towards the poles [38, 39, 40]. This pressure gradient leads to thermospheric winds flowing away from the equator. As a result, the neutral winds tend to drag the ionosphere plasma towards the poles. The Sq current system is created through the effect of Faraday's law. When applying faraday's law, however, we are concerned with the radial component of the earth's magnetic field (B_z) which is the normal component of the conducting E-layer and the earth.

When the E region plasma sheet is located above the magnetic dip equator, the earth's magnetic field lines are nearly horizontal parallel to the surface and minimizes the z-component of the $\vec{B}$ field and the amount of flux passing through the sheet. However as the thermosphere wind drags the E region plasma sheet towards the north pole, the magnitude of B_z and the flux through the sheet increases and as a result $\frac{\partial B_z}{\partial t}$ increases and points towards the earth's surface. Now applying Faraday's law (Eq. (2.4.1)) a counterclockwise electric field "vortex" is generated in the northern hemisphere:

$$\vec{\bigtriangledown} \times \vec{E} = -\frac{\partial \vec{B}_z}{\partial t} \tag{2.4.1}$$

This electric field in turn produces a counterclockwise electric current in the E-region near the magnetic equator [41]. So both the electric field and the current points towards the east direction during the day time. On the other hand in the southern hemisphere the overall electric field is clockwise so again the electric filed and current points eastward near the dip magnetic equator. The resultant eastward electric field in the equatorial E region is called the dynamo electric field. On the night side of the earth a thermal low at the equator reverses the flow of current to westwards.

Equatorial electrojet

Studies of earth's magnetic field have shown strong daily variations even during quiet days. These variations have been attributed to the solar quiet (Sq) and lunar (L) systems, which leads to the equatorial E region current called equatorial electrojet [40].

The electric field associated with this electrojet current is the basis for the vertical $E \times B$ drift motion that cause the fountain effect and equatorial anomaly. Now it is important to study how the electrojet is formed and how it leads to the $E \times B$ drifts [34]. Basically the E region of the earth's ionosphere is the most conducting layer. The altitude from 100-130 km in the E region is located in the dynamo region. The parameter used to specify the ionospheric conductivity is called the magnetization ratio given by Eq. (2.4.2):

$$\frac{\nu_{jn}}{\omega_j} = \frac{\nu_{jn}}{\frac{|e_j|B}{m_j}} \tag{2.4.2}$$

where j is either electrons or ions; ν_{jn} is collision frequency of j with neutrals; ω_j is the gyrofrequency of j; B is the magnitude of magnetic field and e_j is the charge of ion or electron. When electrons or ions are said to be magnetized i.e ($\frac{\nu_{jn}}{\omega_j} << 1$), they move with out the effect of collision. On the other hand when the motion is dominated by collision ($\frac{\nu_{jn}}{\omega_j} >> 1$), and ions or electrons move as if there were no magnetic field present [42]. Magnetization of a particle also depends on both the altitude and mass of the particle. At the D-layer because the neutral density very high, the collision is more dominant so $\frac{\nu_{jn}}{\omega_j} >> 1$ for both ions and electrons. So we get unmagnetized particles and both move parallel to the driving force, for example along an imposed electric field or neutral wind.

When the magnetization ratio for ions and electrons approaches 1, the particle is said to be in the transition region. In this case there are motion in both parallel and perpendicular to the driving forces. The mass difference between ions and electrons makes transition at lower region for electrons than for ions. Electrons begin their transition at about 75 km while ions begin at about 125 km altitude. At about 150 km altitude which is the upper boundary of the E region, because of the rapid decrease of the neutral density the ionization ratio is very small for both ions and electrons. So both particles are magnetized. The E region dynamo is located between 90 and 120 kms, and in this region ions are unmagnetized while electrons are magnetized, that is $(\frac{\nu}{\omega})_i > 1$ and $(\frac{\nu}{\omega})_e < 1$ during the day time but during the night time the E layer ionization almost disappears and the F layer dynamo at around 300 km carries most of the current despite the small value of $(\frac{\nu}{\omega})_i$ at these height [43]. But below this region both are unmagnetized and in both cases they can move together. In the dynamo region, therefore, there is a relative motion between ions and electrons resulting maximum current and high conductivity. For this reason the E region is considered as a highly conducting plasma sheet sandwiched between the non conducting D and F regions. Here there are two important currents to be explained in order to explain for the formation of the equatorial electrojet, which are both perpendicular to the magnetic field. These are namely the Pedersen and Hall currents, where the former is parallel to the driving force example the electric field while the latter is perpendicular to the magnetic and electric fields.

Formation of the electrojet

Within the dynamo region at the magnetic equator, the magnetic field lines are parallel to the surface and directed towards the north. The dynamo electric field is eastwards and is perpendicular to the the northward magnetic field. The electrons in this are magnetized and experience an $E \times B$ drift motion in the upward direction, where as ions are not magnetized and move along the applied forces including along the electric field in the east ward direction. This east ward dynamo electric field produces an up ward $E \times B$ electron Hall motion with in the E-region [36]. When the upward moving electrons encounter the non-conducting plasma, they form a boundary layer between the regions as the dynamo region is sandwiched by the D and F regions. Since ions are not magnetized they form Pedersen motion and move parallel to the applied eastward electric field. Therefore there is a resultant polarization electric field upwards due to charge separation.

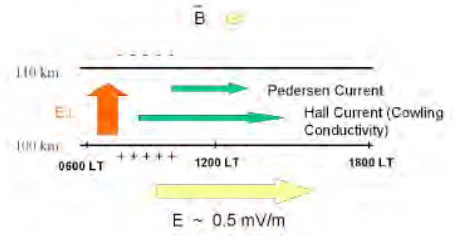

Figure 2.3: Equatorial electrojet, electric fields and current systems
(source: Anderson et al [36])

With in the range of $\pm 3^0$ magnetic latitude, charge separation can be maintained due to the horizontal nature of the magnetic field near the magnetic dip equator. But outside this region charge separation can not be maintained due to enough vertical components of magnetic field lines for the build-up charge to drain. When the induced polarization electric field is crossed with the northward magnetic field, a new Hall current is produced in addition to the eastward Pedersen current and produces what is known as Cowling conductivity at the magnetic equator. So the eastward Pedersen current and the eastward Hall current due to the charge separation sum up to create a substantial eastward current known as equatorial electrojet. The above explanation

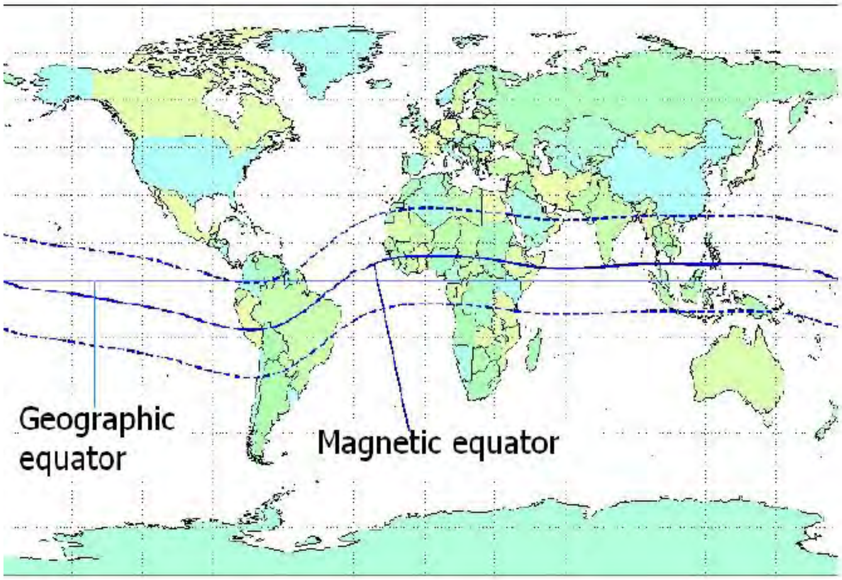

Figure 2.4: Magnetic equator and geographic equator representations (source: Rabiu power point presentation at ISWI/MAGDAS School 2011)

can be explained mathematically as follows. The current density can be expressed as:

$$\vec{J} = \hat{\sigma} \bullet \vec{E} \tag{2.4.3}$$

where the conductivity tensor $\hat{\sigma}$ at the magnetic equator is given by

$$\begin{pmatrix} \sigma_P & 0 & \sigma_H \\ 0 & \sigma_0 & 0 \\ -\sigma_H & 0 & \sigma_P \end{pmatrix} \tag{2.4.4}$$

From Eq. (2.4.3) the horizontal and vertical components of the current density vector are given by

$$J_x = \sigma_P E_x + \sigma_H E_z \tag{2.4.5}$$

$$J_z = -\sigma_H E_x + \sigma_P E_z \tag{2.4.6}$$

The total vertical current vanishes since the upward Pedersen current is nullified by the downward Hall current [43]. So from Eq. (2.4.6), solving for E_z we have:

$$E_z = \frac{\sigma_H}{\sigma_P} E_x \tag{2.4.7}$$

Now inserting Eq. (2.4.7) in to Eq. (2.4.5) we get

$$J_x = \sigma_P (1 + \frac{\sigma_H^2}{\sigma_P^2}) E_x \tag{2.4.8}$$

where $\sigma_P(1 + \frac{\sigma_H^2}{\sigma_P^2})$ is called Cowling conductivity [44].

Equatorial anomaly and the fountain effect

The ionosphere at equatorial latitudes is characterized by a trough in the latitudinal distribution of ionization at the magnetic equator with crests near $\pm 17^0$ magnetic latitude. This feature is called the Equatorial Anomaly. It results from the east-west electric field at the magnetic equator giving rise to an upward $E \times B$ plasma drift during daytime where E is the electric field and B the magnetic field. This upward drift drives the plasma across the magnetic field lines to higher altitudes [42, 45]. The plasma then diffuses downwards along the magnetic field lines under the influence of gravity and pressure gradient forces. The net result is the formation of a plasma fountain, centered at the magnetic equator, which transfers plasma from the equatorial region to higher latitudes. The crest-to-trough ratio in the peak electron density is typically around 1.5 near noon and around 3.5 during the afternoon period when the $E \times B$ drift velocity is high. The latitudinal locations of the crests increase with increasing upward $E \times B$ drift, which vary with solar and magnetic activity. The crests in both hemispheres occur at lower latitudes and become weaker with increasing altitude. Above about 800 km altitude the equatorial anomaly disappears;

there is a single crest at the magnetic equator. The neutral wind causes the equatorial anomaly to be asymmetric about the magnetic equator. The equatorial ionization anomaly is caused by the eastward electric field transporting plasma upwards across the magnetic equator and subsequently diffusing downward and outward along the field lines towards higher latitudes under the influence pressure gradients and gravity. In the direction parallel to the magnetic field, above about 180 km altitude, the ionosphere plasma is controlled by ambipolar electric fields, pressure gradients and collision with the neutral atmosphere. Below 180 km plasma transport becoms less important owing to more rapid chemical processes [46].

H-component of the magnetic field

The variations of this magnetic field can wattribute the electric currents flowing in the earth's ionosphere and ring currents in the magnetosphere. Magnetometers simply measure the three components of the disturbances of the magnetic field: The H-component (horizontal intensity), D-component (Declination) and Z-component (the vertical intensity). These three components together give the magnitude and direction of the magnetic field. Fig. 2.5 describes the three components of the earth's magnetic field.

The H-component of the earth's magnetic field is required to estimate the equatorial electrojet [47]. When the H-component of the magnetic field data extracted from the magnetometers at some degrees off the equator is subtracted directly from data of the H-component of the magnetic field at the magnetic dip equator, then the difference in H is therefore contribution to the electrojet. This contribution is in turn is related directly the eastward electric field that generates the equatorial electrojet current.

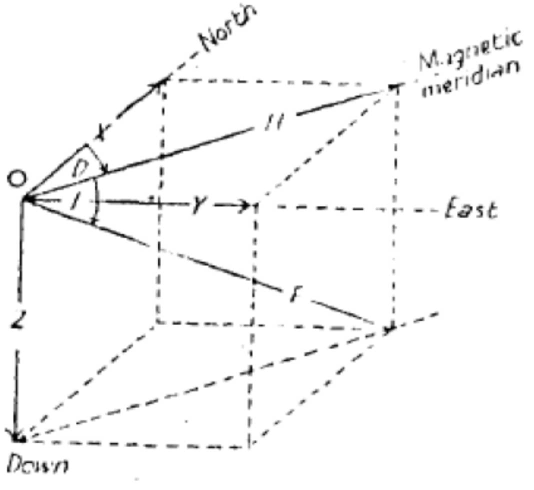

Figure 2.5: Vector components and angles associated with the geomagnetic field (source: Rabiu power point presentation at ISWI/MAGDAS School 2011)

When we subtract to find $\triangle H$ we are eliminating the values of Sq currents and D_{st} ring current contribution of The H-component of the magnetic field [48].

2.5 The earth's dipole field

Electric currents in the earth's core produce magnetic field around the earth. Observations of the geomagnetic fields through decades indicate that the electric current flowing between the earth's surface and space is negligible. The main geomagnetic field is modeled according to the assumptions of Maxwell's equations. Magnetic field is a conservative force field and can be written as the negative gradient of a scalar geomagnetic potential field:

$$\vec{B}(\varphi, \lambda, r, t) = \nabla V(\varphi, \lambda, r, t) \tag{2.5.1}$$

The geomagnetic potential can be expanded in spherical harmonics [49]:

$$V(\varphi, \lambda, r, t) = a \sum_{n=1}^{\infty} (\frac{a}{r})^{n+1} \sum_{m=0}^{n} [g_n^m(t) \cos m\varphi + h_n^m(t) \sin m\varphi] P_n^m(\sin(\varphi)) \qquad (2.5.2)$$

where a=6371 km is called radius of the earth, φ, λ and r are latitude, longitude and radius in geocentric spherical reference frame. $P_n^m(\sin(\varphi))$ is normalized associated Legendre function. $g_n^m(t)$ and $h_n^m(t)$ are time dependent Gauss coefficients of degree n and order m. In gauss coefficients the degrees from 1 to 8, they are assumed to have quadratic in time:

$$g_n^m(t) = g_n^m + \dot{g}_n^m(t - t_0) + \frac{1}{2}\grave{g}_n^m(t - t_0)^2 \qquad (2.5.3)$$

$$h_n^m(t) = h_n^m + \dot{h}_n^m(t - t_0) + \frac{1}{2}\grave{h}_n^m(t - t_0)^2 \qquad (2.5.4)$$

where g_n^m, $\dot{g}_n^m$,$\grave{g}_n^m$, h_n^m, $\dot{h}_n^m$, and $\grave{h}_n^m$ are constants and time is given in decimal year and t_0 is the reference date of the model. The degrees from 9 to 12 have linear dependence on time and the degrees of higher orders are constants. The International Geomagnetic Reference Field (IGRF) which is updated every 5 year is the most common main field model which has degree of 10 and order of 10. There are other models with diverse degree and order. For example, the Potsdam magnetic model of the earth (POMME-3-1) by [50], attains degree of 90 and order of 90. The magnetic field of the earth is always changing and a series of the spherical harmonics have to be updated from year to year. In 150 years of data, it is observed that the dipole moment is changing throughout. We noticed that there has been a decreasing trend in $M0$ and that the decrease in fact is stronger now than it has been throughout this period. If this tendency continuous, the magnetic field will disappear within about 2000 years time [51].

The dipole magnetic potential V at a point p whose vector position relative to the dipole center r is given by

$$\frac{M \bullet \hat{r}}{r^3} = \frac{-M \sin\theta}{r^2} \tag{2.5.5}$$

where M is magnetic moment and θ is the dipole latitude.

The radial (vertical component Z of the field), reckoned positive when inward, is given by

$$Z = -\frac{\partial V}{\partial r} = -\frac{2M \sin\theta}{r^3} \tag{2.5.6}$$

While the tangential field H, lies in the magnetic meridian through p directed north and is given by

$$H = \frac{1}{r}\frac{\partial V}{\partial \theta} = -\frac{M \cos\theta}{r^3} \tag{2.5.7}$$

Similarly the magnetic dip or also called inclination I, measured positive when directed below the horizontal, is given by

$$\tan I = \frac{Z}{H} = 2\tan\theta \tag{2.5.8}$$

The total field is given by

$$B = \sqrt{H^2 + Z^2} \tag{2.5.9}$$

2.6 Transport processes in the ionosphere

The charged particles in the ionosphere are highly affected by the external magnetic field of the earth. This is because the earth's magnetosphere and ionosphere are linked via the external magnetic field of the earth and the strong interaction between charged particles and field lines results in capturing the particles and impose restriction for their motion in the ionosphere. Transport processes are governed by diffusion processes in a gravity fields, thermospheric winds and electric fields [49].

2.6.1 Neutral winds

Under quiet conditions the temperature of the upper atmosphere is greater near the sub-solar and is lower in the nightside. This result in pressure difference that drives a horizontal neutral wind from dayside towards the nightside is shown in Fig. 2.6. The Sq, the solar quiet diurnal variation, one of the currents in the ionosphere is produced by currents in the ionosphere driven by the winds. The Sq current is driven by solar EUV radiation, which not only produces the ionization in the E-region but also heats the atmosphere and causes the wind. The primary component that drives the Sq current is the diurnal tide (1,-2), which has a small phase progression with altitude. The solar diurnal tide has 24 hours and covers the earth's circumference at

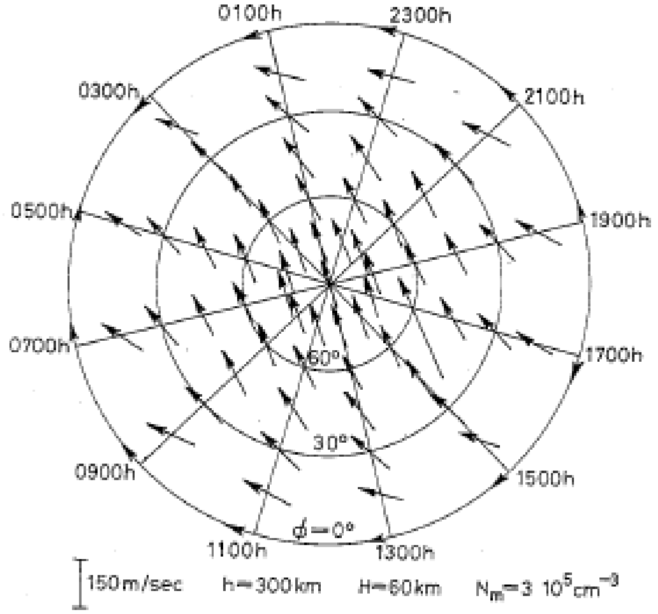

Figure 2.6: Atmospheric wind system in the northern hemisphere (Source: The solar terrestrial environment, J. K. Hargreaves)

the observer's latitude in 24 hours. Such tide has wave number 1. The semi-diurnal tide has a period of 12 hours but covers the earth's circumference in 24 hours and has a wave number 2.

2.6.2 The electromagnetic drift

The conductivity of the ionosphere varies with height and reaches its maximum at about about 102 Km (E-region) called the central dynamo layer or the conducting plasma layer. The conducting plasma layer is moved across the earth's magnetic field under the influence of mainly the sun and the moon. The magnetic field fluctuation which we observe at the earth's surface is the results of more or less permanent current systems in the earth's ionosphere and magnetosphere.

2.6.3 Atmospheric gravity waves

According to Schunk and Nagy [34] atmospheric gravity waves (AGWs) are classified into three groups. These are the largest scale which propagate in a global scale, the smallest scale which relates to acoustic waves that do not play an important role in the atmosphere and the third group are the atmospheric waves which are produced by buoyancy in the atmosphere called atmospheric gravity waves.

AGWs have typically a localized source and can travel vertically as well as horizontally with limited range of wavelengths. Gravity waves are caused by a variety of sources, including the passage of wind across terrestrial land forms, interaction at the velocity shear of the polar jet stream and radiation incident from space. They are found to affect atmospheric tides in the middle atmosphere and terrestrial weather in the lower atmosphere.

2.7 Solar disturbance and geomagnetic storms

The solar increase in the solar wind energy accompanied by an increase in the solar proton radiation or an increase in the velocity and concentration solar charged particle radiation in the polar upper atmosphere, leads to not only producing electric currents but also heats polar upper atmosphere. So the solar disturbances affect the electron density of the ionosphere. The most significantly perturbations occurs in the F-region particularly near the peak electron density. The mid latitude F2-region responses to geomagnetic storms in three phases: 1. an initial or positive phase in which the peak electron density increases with respect to the pre-storm condition which lasts after few hours; 2. negative phase in which the peak electron density decrease with respect to the the pre-storm conditions which may last several days; and 3. the recovery phase in which the ionosphere returns to its original condition.

A geomagnetic storms can cause thermospheric winds that can generate currents and can change the composition of the upper atmosphere.

2.8 Ionospheric currents

The flow of currents in the upper atmosphere was confirmed by ground based magnetic field fluctuations recorded by magnetometers as early as the 1880's. These currents are caused by the differential drifts among the various constituents of plasma. The differential drifts are due to the disparity in the response by the plasma components to interactions with force fields such as electric fields, geomagnetic fields, gravitational fields, neutral atmospheric wind fields, plasma pressure gradient fields etc. Due to the presence of magnetic field ionospheric currents are anisotropic hence ionospheric conductivities are direction dependent. The ionospheric current system is a result of a dynamo action of the horizontal wind system and the electrical conductivity of the ionosphere in the presence of the electrons and ions. The concentration of ionospheric current near the magnetic equator is a result of the high value of electrical conductivity of the upper atmosphere at the dip equator, which arises from an inhibition of hall current due to the horizontal configuration of the earth‘s magnetic field and the horizontal stratification of the ionosphere [52, 44]. A charged particle in a constant magnetic field experiences a force perpendicular to its motion. The resulting trajectories of ions and electrons in the magnetosphere are a complex superposition of motions as each particle travels in a spiral around a magnetic field line, bounces back and forth between the North and South Poles, and drifts around the planet, with electrons drifting east and protons drifting west. The origins of the irregularities of the geomagnetic fields are associated with interaction between the solar winds and the magnetosphere, and the coupling process between the magnetosphere and high latitude ionosphere through magnetic field lines are generally considered as a disturbance field with regular solar quiet currents. They are accounted for through the indexes like Dst, AE, EU, etc. The absorption of EUV and x-ray radiations by O_3 in stratosphere and molecular O_2 in the low thermosphere generates thermospheric neutral winds. These charged particles are carried through the geomagnetic fields by the neutral with a velocity via collision and these processes generate electric fields and currents in the dynamo region of the ionosphere [53, 54]. Generally the current density in the ionosphere is given by the Ohm's law which is expressed as Eq.(2.8.1):

$$\vec{J} = \bar{\sigma}(\vec{E} + \vec{v_n} \times \vec{B}) \tag{2.8.1}$$

It is easy to show that the current density can be projected in a referential associated with the geomagnetic field lines and it can be summarized as

$$\vec{J} = \sigma \vec{E_{\parallel}} + \sigma_p(\vec{E_{\perp}} + \vec{v_n} \times \vec{B}) + \sigma_H \frac{\vec{B}}{B} \times (\vec{E_{\perp}} + \vec{v_n} \times \vec{B}) \tag{2.8.2}$$

where

$\sigma_0 = N_e e^2(\frac{1}{m_e \nu_e} + \frac{1}{m_i \nu_i})$ is parallel conductivity; $\sigma_p = \frac{N_e e}{B}(\frac{\nu_e \Omega_e}{\nu_e^2 + \Omega_e^2} + \frac{\nu_i \Omega_i}{\nu_i^2 + \Omega_i^2})$ is Pedersen conductivity; $\sigma_H = \frac{N_e e^2}{B}(\frac{\Omega_e^2}{\nu_e^2 + \Omega_e^2} - \frac{\Omega_i^2}{\nu_i^2 + \Omega_i^2})$ is Hall conductivity; $\Omega_e = \frac{eB}{m_e}$ is the gyro frequency of the electrons; $\Omega_i = \frac{eB}{m_i}$ is the gyro frequency of the ions; $\nu_e = \nu_{en} + \nu_{ei}$ is collision frequency of electrons with neutrals and ions; $\nu_i = \nu_{in} + \nu_{ie}$ is collision frequency of ions with neutrals and electrons [53].

The above currents give rise to the production of the world wide current called the global solar quit current. The polarization electric fields are generated so as to preserve divergence free currents in the ionosphere. Electric fields generate by the wind dynamo mechanisms derive current and set the ionospheric plasma into vertical and horizontal motion.

The parallel (longitudinal), Pedersen and Hall currents respectively flow in the direction parallel to the magnetic field, perpendicular to the magnetic field but parallel to the electric field and perpendicular to the both magnetic and the electric fields.

2.9 Formation of electric fields in the ionosphere

Polarization electric fields are generated so as to preserve divergence free currents in the ionosphere. Electric fields generated by the wind dynamo mechanisms that drive currents and set the ionospheric plasma into vertical and horizontal motion. These electric fields are vertical electric fields and the terminator electric fields. In the E-region the Pedersen and Hall conductivities are both important and have separate

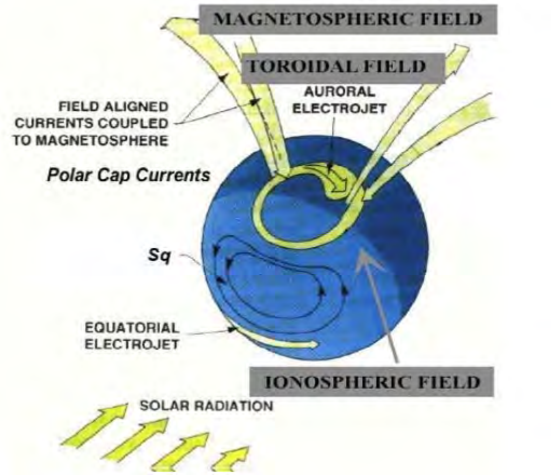

Figure 2.7: Current systems in the Ionosphere (Source: NASA/GSFC and the Danish space research Institute(DSRI))

consequences. The neutral wind moves the ions in the direction of the wind, in regions where the Hall conductivity dominates. Electric fields result from accumulation of polarization charges wherever the wind driven current has a divergence. In the region where the Pedersen conductivity is important during the daytime the poleward wind drives a westward current with the accumulation of positive and negative polarization charges at the dawn and dusk terminators, respectively [42, 36].

2.9.1 The terminator electric fields

On the day side of the earth, the sun heats the neutral gases found in the upper atmosphere. Heating makes expansion and the neutral gas expansion produces Pedersen currents $E = \sigma_p(U \times B)$ for both E and F regions [27]. The Pedersen current flowing towards the morning sector is mainly carried by ions. Electrons are left behind ions since they are magnetized. So the positive charges are accumulated at the dawn terminator and negative charges accumulate at the dusk terminator. This happens because the conductivities fall sharply beyond the morning and evening terminators. The Divergence free current free requirement in the plasma opposes net charge accumulation at the terminators by setting up a zonal electric field and hence the polarization electric field is directed from dawn to dusk terminators and its direction is east ward during day time and west ward during night time [55]. The Diurnal zonal polarization electric field produced by the current termination mechanism produced in the E and F regions is called the terminator electric field. This field undergoes seasonal and solar cycle variations with larger magnitude during equinoxes and solar maximum conditions. There is a phenomena observed that the zonal electric field of the equatorial ionosphere is enhanced around sunset before westward polarity reversal called prereversal enhancement.

2.9.2 Vertical polarization electric field

Earlier works such as [53, 27, 42] show that during quiet times, zonal drifts are westward producing upward electric field and eastwards producing downwards electric fields. The upward Pedersen current flowing in the F region driven by eastward wind field is given by $\sigma_p uB$ where $u = U.\hat{x}$ which represents the projection of the wind vector in the zonal direction [55]. The vertical current given by $\sigma_p uB$ is divergent because of the finite thickness of the pedersen conductivity layer. The vertical polarization electric field, E_p, developed to keep the current divergent free is given by Eq. (2.9.1):

$$E_p = -\frac{uB \sum_p^F}{\sum_P^E + \sum_p^F} \tag{2.9.1}$$

where $\sum_p^E$ and $\sum_p^F$ are magnetic field line integrated E and F region Pedersen conductivities respectively [42].

2.9.3 The height variation of conductivity

The conductivity depends on the ratio of gyro-frequency to collision frequency $(\frac{\omega}{\nu})$. Since the ratio between the Hall and Pedersen conductivities for a given electron or ion density is just $(\frac{\omega}{\nu})$ therefore it is strongly height dependent because the ratio $(\frac{\omega}{\nu})$ is not the same at different heights. Note that in the Hall conductivity $\sigma_H = \frac{N_e e^2}{B}(\frac{\Omega_e^2}{\nu_e^2+\Omega_e^2} - \frac{\Omega_i^2}{\nu_i^2+\Omega_i^2})$ the electron and ion terms are opposite sign, so the total Hall conductivity depends on the difference between the electron and ion conductivities not on their sum. This time it is well accepted that daytime eastward zonal component of the dynamo electric field in the electrojet region drives an eastward Pedersen current and an upward Hull current [56]. The formation of this upward Hull current is responsible for the development of the vertical polarization electric field. The Hall conductivity peaks at E-region, the Pedersen conductivity peaks higher and the direct conductivity continues to increase with height. The Hall conductivity is small in the F-region because the electron and ion components almost cancel out there. The Fig. 2.8 below illustrates the height variation of the direct, Pedersen and Hall conductivities in the ionosphere and it is directly plotted using the IRI2012 model.

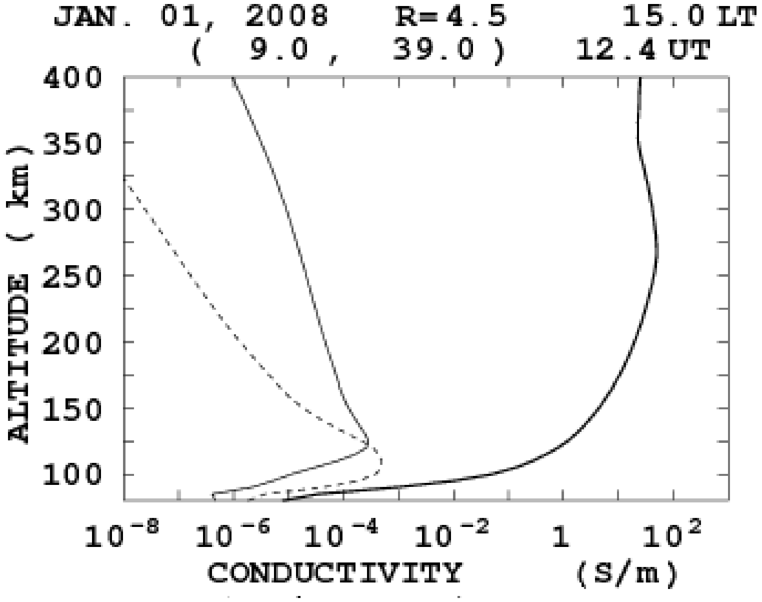

Figure 2.8: The daytime height profile of the ionospheric conductivity. It is calculated using IRI2012

Chapter 3

Ionosphere Probing Techniques

3.1 Global Navigation satellite System (GNSS)

The Global Positioning System (GPS) is a constellation of navigation satellites operated by US Department of Defence (DOD). GPS became operational since 1980 and consists of at least 24 operational satellites distributed in 6 orbital planes with 4 satellites per plane. The satellites are placed at an altitude of 20200 Km above the earth with 12 hrs orbital period and 55^0 orbital inclinations. The time, velocity and position of GPS satellites are continuously monitored by ground based networked radars and up to 12 satellites are visible at a time. GPS satellites transmit their individual ephemeris on two carrier frequencies in the L-band for civilian users f1=1575.42 MHz (L1) and f2=1227.60 MHz (L2). Each GPS signal consists of three components namely carrier, code and navigation data. These three components of the signal are derived coherently from one of the frequencies of the atomic clocks aboard the satellite. The frequency of the atomic standards aboard a satellite is 10.23 MHz. GPS signals, like other electromagnetic waves, are affected by the electrically charged ionised plasma in the upper Atmosphere.

Global'naya Navigationnaya Sputnikovaya Systema (GLONASS) is the Russian navigation system equivalent to GPS. Again its constellation is composed of 24 satellites with an orbital inclination of 64.8^0 and an orbital radius of 25500 km. Also GLONASS satellites transmit signals on the L1 and L2 frequency bands, each satellite transmits its signal with different frequency offset. So to distinguish from from GPS carriers G1 and G2 are used. Like the GPS, GLONASS is also a dual-use, i.e for civilian and military purposes.

Galileo is the European global navigation satellite system. Unlike the GPS and GLONASS, Galileo is under civilian control. The Galileo satellite constellation will consist of 30 satellites (27 operational and 3 non-functional). The satellites are orbiting at an altitude of 23222 Km at inclination of 56^0.

Compass is a Chinese satellite navigation system which is presently under development. The system is a dual system which will provide two navigation services (an open services for commercial users and for an Authorizesd persons). Compass consists of constellation of 30 non-stationary satellites, 5 geostationary satellites and 3 more satellites in geosynchronous orbit. The first non-stationary satellites are in three orbital planes with an inclination of 55^0 at an orbital radius of 27900 km. While the Geosynchronous once are at an altitude of 3585 km and inclination 55^0.

3.1.1 Ionospheric effects on electromagnetic waves

The ionosphere is a dispersive medium, thus a linear combination of observable on the two frequencies is needed to remove this effect for positioning. On the other hand the dispersive property provides an opportunity to measure directly the ionospheric electron content along the ray path. The travel time of an electromagnetic wave through a medium with refractive index n is given as

$$t_{travel} = \int_{raypath} \frac{1}{c_{medium}} dr \tag{3.1.1}$$

where c$_{medium}$ is the speed of light in media. The phase refractive index as a function of the frequency is

$$n^2 = 1 - \frac{\omega_p^2}{\omega^2} \tag{3.1.2}$$

where $\omega_p^2 = \frac{Ne^2}{\varepsilon_0 m_e}$ is the plasma frequency

Solving Eq. (3.1.2) for small n and Taylor expansion, we have

$$n = 1 - \frac{\omega_p^2}{2\omega^2} = 1 - \frac{Ne^2}{8\pi\varepsilon_0 m_e f^2} \tag{3.1.3}$$

and using $A = \frac{e^2}{8\pi\varepsilon_0 m_e} = 40.3\frac{m^3}{s^2}$ we can write

$$t_{travel} = \frac{1}{c}\int_{raypath} 1 - \frac{AN(\vec{r})}{f^2} d\vec{r} \tag{3.1.4}$$

The ionospheric phase delay relative to wave propagation in a vacuum is

$$I_{phase} = t_{travel}^{medium} - t_{travel}^{vacuum} = -\frac{A}{cf^2}\int_{raypath} N(\vec{r})d\vec{r} \tag{3.1.5}$$

The minus sign in Eq. (3.1.5) indicates the phase is advanced so Eq. (3.1.3) has the form

$$n_g = 1 + \frac{\omega_p^2}{2\omega^2} \tag{3.1.6}$$

where n_g is the group refractive index. Therefore the average group is delayed by

$$I_{group} = t_{travel}^{medium} - t_{travel}^{vacuum} = \frac{A}{cf^2}\int_{raypath} N(\vec{r})d\vec{r} \tag{3.1.7}$$

Thus the group delay is equal to the negative of the phase advance [57]. The phase of the GPS carrier wave is advanced by the same amount of time that the information in a wave group is delayed. The latter integral in Eq. (3.1.5) and (3.1.7) is simply the electron density integrated along the ray path from satellite to receiver, which is called the Total Electron Content (TEC). Therefore TEC can be calculated as [58]:

$$TEC = \int_{raypath} N(\vec{r})d\vec{r} \tag{3.1.8}$$

The total electron content along the GPS ray path from a satellite to a receiver is known as slant TEC (STEC). TEC is the number of electrons in the slant column with unit squared cross-section in the ionosphere along the signal path. It is expressed in TECU (TEC-Units) with $1TECU = 10^{16} electrons/m^2$. The STEC can be obtained from the difference between the pseudo ranges (P1 and P2), and the difference between the phases (L1 and L2) of the two GPS signals ([59] and references therein). The relevant equations are

$$STEC_{co} = [(\frac{f_2^2}{f_1^2 - f_2^2})\frac{2f_1^2}{K}](P_2 - P_1) \tag{3.1.9}$$

$$STEC_{ph} = [(\frac{f_2^2}{f_1^2 - f_2^2})\frac{2f_1^2}{K}](L_1\lambda_1 - L_2\lambda_2) \tag{3.1.10}$$

where f_1 and f_2 are GPS signal frequencies and are equal to 1.57542 GHz and 1.2276 GHz, respectively, $K = 80.62\ m^3s^{-2}$ is a constant that relates plasma frequency to electron density, λ_1 and λ_2 are the wavelengths corresponding to f_1 and f_2.

3.1.2 Single layer ionosphere approximation

The TEC is valid for line of sight from the receiver on the ground to the satellite. The ionosphere may be considered as a thin single layer surrounding the earth at a fixed height from the earth for which all the free electrons in the ionosphere are assumed to be concentrated in a single layer thin shell at the height of the main electron concentration in the ionosphere. In addition to that if we assume there are no lateral or horizontal electron density gradients, the vertical TEC (VTEC) can be simply mapped to the slant TEC:

$$STEC = \frac{1}{\cos z} VTEC \tag{3.1.11}$$

where z is the satellite zenith angle at the point of intersection of the line of sight with that of the spherical single layer ionosphere called the ionospheric piercing point (IPP) and the multiplier $\frac{1}{\cos z}$ is called the obliquity factor. The vertical projection of IP on the ground is referred as the sub-ionospheric point (SIP). The satellite zenith angle at the receiver location $z^{'}$ and at the ionospheric pierce point is related by

$$\sin z = \frac{R}{R+H} \sin z' \tag{3.1.12}$$

where H is height of the ionospheric single layer from the earth and R is the radius of the earth.

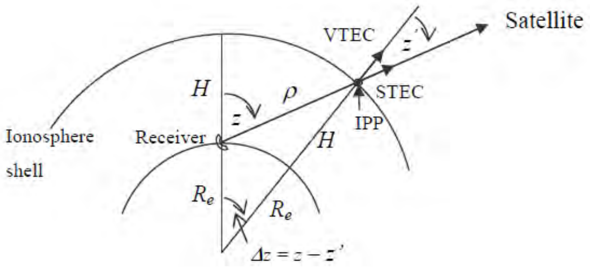

Figure 3.1: Slant to vertical TEC mapping function geometry

3.2 Conventional ionospheric measurements: the ionosonde

The conventional instrument for measuring the virtual height of the ionosphere is a sweep-frequency pulsed radar device called the ionosonde. An ionospheric sounding consists of vertical sweep of the ionosphere by a predetermined frequency band ($< 30MHz$) with a sweep duration from few seconds (e.g. 10 second) to few minutes. During reflection electron density values are calculated from reflected radio waves corresponding to the density dependent critical frequency (f_p) of the ionized plasma and density heights are inferred from the time delay of the reflected radio waves. The ionosonde provides estimates electron density maxima of each layer and the estimated altitude at which the density occurred, as a function of time. The ionosphere is a dispersive medium so the electromagnetic wave reflection depends on the signal frequency of the wave. In the presence of magnetic field of the earth, the ionosphere is doubly reflecting medium, and two modes of propagation exist for which names, ordinary and extraordinary. Assuming collision of ions with neutrals is negligibly small, the refractive index from the Appleton and Hartree [49] is well explained and can be expressed as:

$$\mu^2 = 1 - \frac{X(1-X)}{(1-X) - \frac{1}{2}Y_T^2 \pm [\frac{1}{4}Y_T^4 + (1-X)^2 Y_L^2]^{\frac{1}{2}}} \qquad (3.2.1)$$

where μ is the complex refractive index, $X = \frac{\omega_p^2}{\omega^2}$, $Y = \frac{\omega_H}{\omega}$, $Y_T = Y \sin\theta$, and $Y_L = Y \cos\theta$

Assuming plasma is horizontally stratified, a wave vertically incident on the ionosphere is reflected at a level where $\mu^2 = 0$ and this occurs for ordinary wave, where $X = 1$. The relation between the electron density and the critical frequency is given by

$$N_e = \frac{4\pi^2 m f^2 \varepsilon_0}{e^2} \qquad (3.2.2)$$

where N_e is the electron density (number of electrons per cubic meters); f is frequency of radio wave which $f = f_p$; where f_p is the plasma frequency, e and m are charge and mass of electron respectively; ε_0 is permittivity of vacuum which is $8.85 \times 10^{-12} F.m^{-1}$. The ionosonde consists of transmitter and receiver with coupled tuning circuits, which is a sweep in frequency usually in a frequency range of $0.5 - 25MHz$. After the RF signals have been reflected by the ionosphere they are received and processed by the receiver to produce ionograms. The basic information in the received signal in the transit time for passage between the ionospheric layers and the earth, frequency, amplitude, phase polarization, doppler shift and spectrum shape. From these quantities, we can obtain an ionogram, which is a plot of the virtual height of reflection versus frequency. Assuming the wave speed to be equal to that on free space, the time of flight of a radio signal at a particular frequency indicates the virtual height (h') of the reflecting layer. The 2D plot of h' as a function of radio frequency is called the ionogram. The virtual height is always higher than the real height (h) because of the group and phase delays of radio waves traveling through out the ionized medium [49].

Limitations all ionosondes is that they can give information on the ionosphere only up to the height of maximum ionization of the F2 layer, again unless one extends end of the sweep (to at least 250 KHz), by an increasing the height of the transmitting antenna tower and using relatively higher power not much information can be obtained from the D region. Because low frequency radio waves are absorbed by the D region. During sudden ionospheric disturbances (SIDs) and intense polar cap precipitation of solar energetic particles, D region ionization can become so intense that HF radio communication is completely blacked out so information from ionosonde is limited.

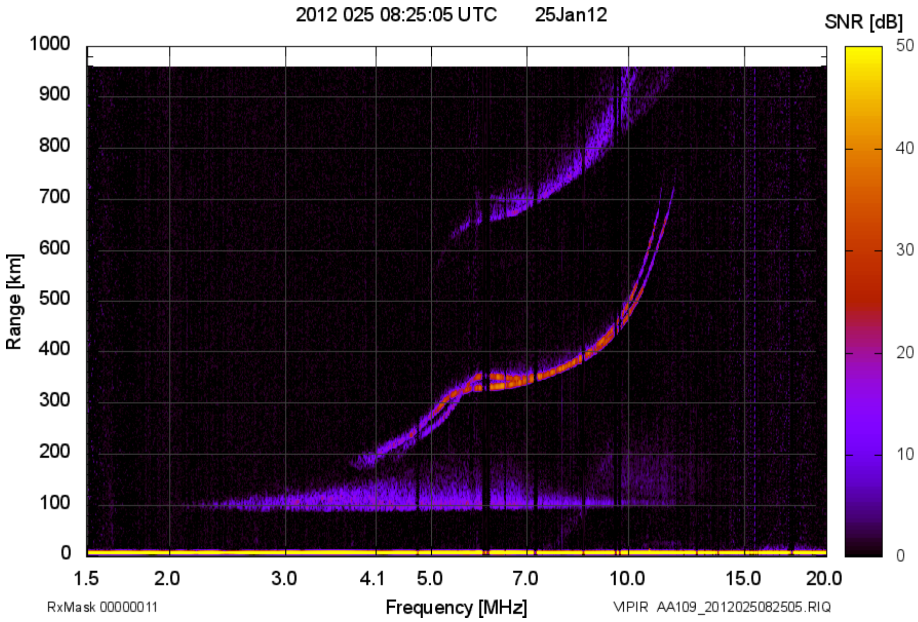

Figure 3.2: Ionogram recorded at Welmera station for the day 25/01/2012 at 8:25 UT

Chapter 4

Data and methodologies

4.1 Data

The observational and model data used are described as follows. TEC data are used to study the ionospheric seasonal, diurnal variability and an input data for the NeQuick electron density. The TEC data are downloaded from UNAVCO data home page http://facility.unavco.org/data/gnss/perm-sta.php. The NeQuick2 Model is free available at ICTP. The ionosonde data is obtained from the newly installed HF-viper radar at Welmera site. The data consists of height of reflection of waves and frequency reflected at the given height. Then the electron density is calculated from the frequency-electron density relating equation. The observed changes of geomagnetic field during geomagnetic storm are essentially a consequence of strong and rapid magnetospheric processes and changes under solar wind action. The geomagnetic storms can be classified according to different Dst index levels as: weak for $-50nT \leq Dst \leq -30nT$; moderate for $-100nT \leq Dst \leq -50nT$ and intense for $Dst < -100nT$ (e.g. [60, 61] and references therein). The data for Dst index is downloaded from wdc.kugi.kyoto-u.ac.jp/dst_realtime/presentmonth/index.html. The Dst value for geomagnetically quite days prior to storm occurrence is greater than -20 nT

whereas the Dst values during the storm period fall in moderate storm category. The EEJ is characterized using magnetometer data collected from two station of magnetometer observatories. The Intermagnet magnetometer data is available at the World Data Center, Kyoto and AMBER magnetometer data is collected from Adigrat observatory. The magnetometer data consists of X, Y, and Z components of magnetic field recorded by the instrument at every minute. The EEJ2 model is downloaded from the web site: http://www.geomag.us/models/EEJ.html. The model is used to generate EEJ current data. The data on solar wind parameters such as plasma flow, pressure/solar wind pressure (PSW), solar wind speed (Vsw), interplanetary electric field (IEF)Esw, the H-component of symmetric ring current (SYM-H), H-component of asymmetric ring current (ASY-H) indices, the auroral electrojet (AE) are downloaded from the database available with coordinated data analysis web page (http://cdaweb.gsfc.nasa.gov/istp public/). It contains the values of the interplanetary magnetic field (IMF) and solar wind parameters measured by various spacecrafts (ISEE3, IMP8, etc.) near the earths orbit. The correction of time delay of about 51 minutes between locations of the spacecrafts and the magnetopause is incorporated in the temporal evolutions of solar wind parameters. The TEC used in this study is obtained from database maintained by NASA JPL. The critical frequency $foF2$ and height hmF2 observed for few hours on January 25, 2012 by new ionosonde instrument at geomagnetic equator over Addis Ababa are used to compliment analysis based on observed TEC to characterize the ionospheric response to the storms over this longitude sector for the first time.

4.2 Data analysis methodologies

The ionospheric electron density model NeQuick is a profiler‘which uses the peaks of the E-layer, F1-layer and F2-layer as anchor points related to the ionospheric characteristics routinely scaled from ionograms ($foF2, M(300)F2, foF1, foE$). NeQuick is a three dimensional and time dependent ionospheric electron density model developed at the Aeronomy and radiopropagation laboratory at the Abdus Salam International Center for theoretical physics (ICTP), Trieste, Italy and the Institute for Geophysics, Astrophysics and Meteorology of the University of Graz, Austria [62]. The electron density at any location is computed based on the characteristic parameters of the anchor points at a given location and time of the ionosphere. The formulation of the NeQuick model is based on the Epstein layer so we need to explain the Epstein layer. The Epstein layer is an electron density function is built on Epstein function and is represented by the following expression [63, 64, 65]

$$n(h) = \frac{4n_{max}}{(1+\exp{(\frac{h-hmax}{B})})^2}\exp(\frac{h-h_{max}}{B}) \tag{4.2.1}$$

where $n(h)$ is the electron at height h, n_{max} is the peak electron density, h_{max} the height of the peak electron density and B is the thickness of the layer.

The electron density of the Epstein layer is a symmetric function and has a parabolic form around the height of the electron density. Better results from NeQuick model are obtained by considering different values of the thickness of the bottom and top parts of the Epstein layer associated to each ionospheric region (E,F1, F2) [66]. Based on this, the formulation of NeQuick for the bottom side ($h \leqslant h_{max,F2}$) is based on the five semi-Epstein layers. These are two semi-Epstein layers from E region (top and bottom), two for the F1 region(top and bottom) and for the bottom of F2 region. But

NeQuick does not take any characteristic parameters of the D region in to account. The electron density at any given height less than the height of peak electron density of the bottom side of F2 region is computed by summation of the three semi-Epstein layers. Thus

$$n(h) = \sum_{E,F1,F2} n_i(h) \tag{4.2.2}$$

where $n_i(h) = \frac{4A_i}{(1+\exp(z_i))^2}\exp(z_i)$.

In Eq. (4.2.2) the expression for Z_i and A_i are defined as in tables 1-3 for each semi-Epstein layers.

height interval (km)	B	Z_{F2}	A_{F2}
$h \leq 100$	$B_{bot,F2}$	$\frac{h-h_{max,F2}}{B_{bot,F2}}$	$A_{max,F2}$
$100 \leq h \leq h_{max,E}$	$B_{bot,F2}$	$\frac{h-h_{max,F2}}{B_{bot,F2}}$	$n_{max,F2}$
$h_{max,E} \leq h \leq h_{max,F1}$	$B_{bot,F2}$	$\frac{h-h_{max,F2}}{B_{bot,F2}}$	$n_{max,F2}$
$h_{max,F1} \leq h \leq h_{max,F2}$	$B_{bot,F2}$	$\frac{h-h_{max,F2}}{B_{bot,F2}}$	$n_{max,F2}$

Table 1. The Epstein layer associated to the bottom of F2.

height interval (km)	B	Z_{F1}	A_{F1}
$h \leq 100$	$B_{bot,F1}$	$\frac{h-h_{max,F1}}{B}\exp\frac{10}{1+2\lvert h-h_{max,F2}\rvert}$	$n_{max,F1} - n_{F2}(h_{max,F2})$
$100 \leq h \leq h_{max,E}$	$B_{bot,F1}$	$\frac{h-h_{max,F1}}{B}\exp\frac{10}{1+2\lvert h-h_{max,F2}\rvert}$	$n_{max,F1} - n_{F2}(h_{max,F2})$
$h_{max,E} \leq h \leq h_{max,F1}$	$B_{bot,F1}$	$\frac{h-h_{max,F1}}{B}\exp\frac{10}{1+2\lvert h-h_{max,F2}\rvert}$	$n_{max,F1} - n_{F2}(h_{max,F2})$
$h_{max,F1} \leq h \leq h_{max,F2}$	$B_{top,F1}$	$\frac{h-h_{max,F1}}{B}\exp\frac{10}{1+2\lvert h-h_{max,F2}\rvert}$	$n_{max,F1} - n_{F2}(h_{max,F2})$

Table 2. The Epstein layer associated to the bottom E

height interval (km)	B	Z_E	A_E
$h \leq 100$	$B_{bot,E}$	$\frac{h-h_{max,F1}}{B}\exp\frac{10}{1+2\lvert h-h_{max,F2}\rvert}$	$n_{max,E} - n_{F1}(h_{max,E}) - n_{F2}(h_{max,E})$
$100 \leq h \leq h_{max,E}$	$B_{bot,E}$	$\frac{h-h_{max,F1}}{B}\exp\frac{10}{1+2\lvert h-h_{max,F2}\rvert}$	$n_{max,E} - n_{F1}(h_{max,E}) - n_{F2}(h_{max,E})$
$h_{max,E} \leq h \leq h_{max,F1}$	$B_{top,E}$	$\frac{h-h_{max,F1}}{B}\exp\frac{10}{1+2\lvert h-h_{max,F2}\rvert}$	$n_{max,E} - n_{F1}(h_{max,E}) - n_{F2}(h_{max,E})$
$h_{max,F1} \leq h \leq h_{max,F2}$	$B_{top,E}$	$\frac{h-h_{max,F1}}{B}\exp\frac{10}{1+2\lvert h-h_{max,F2}\rvert}$	$n_{max,E} - n_{F1}(h_{max,E}) - n_{F2}(h_{max,E})$

Table 3. The Epstein layer associated to the bottom F1

The semi-Epstein layers for the top side of the E and F1 layers are lowered to zero at the peak of F2 region due to the exponential factor in the formulation of Z_E and

Z_{F1} to avoid secondary maxima in the vertical profile of the electron density.

Although the NeQuick model for the top side of the F2 layer is a semi-Epstein layer, it has a height dependent thickness parameter. The electron density in the F2 layer is computed by [66] for $h_{max,F2} \leq h$ as

$$n_{topside}(h) = \frac{4n_{max,F2}}{(1+\exp(z_i))^2}\exp(z) \tag{4.2.3}$$

The expression for z is defined by Eq. (4.2.4) as follows:

$$z = \frac{h - h_{max,F2}}{H[1 + \frac{rg(h-h_{max,F2})}{rH+gh_{max,F2}}]} \tag{4.2.4}$$

In fact the denominator represents the height dependent thickness parameter for the top side of F2 region and H is the scale height given by

$$H = \frac{B_{top,F2}}{v} \tag{4.2.5}$$

where

$$v = (0.041163x - 0.183981)x - 1.424472 \tag{4.2.6}$$

and

$$x = \frac{B_{top,F2} - 150}{100} \tag{4.2.7}$$

In Eq. (4.2.4), Leitenger et al [67] use the factor $r = 100$ and $g = 0.125$ is a height gradient for the scale height H for which the value of $rH + g(h_{max,F2})$ restricts the scale height increase in the top side of F2 region.

In NeQuick , the peak electron densities of the three regions (E, F1, and F2) are calculated in electrons per cubic centimeter using the equation

$$n_{max,X} = 1.24 \times 10^4 (f_{0X})^2 \tag{4.2.8}$$

where X stands for E, F1 or F2. The peak height of the E region is fixed at about 120 km while peak heights for F1 and F2 regions depend on the peak electron densities of the regions will be explained as follows.

The peak height of F2 region is determined from ionosonde parameters of f_0E, F_0F2 and $M(3000)F2$:

$$h_{max,F2} = \frac{1490\mu}{M + \triangle} - 176km \tag{4.2.9}$$

where the quantities μ and $\triangle$ are defined as follows:

$$\mu = M\sqrt{\frac{0.0196M^2 + 1}{1.2967M^2 - 1}} \tag{4.2.10}$$

$$\triangle = \left\{ \begin{array}{lll} \frac{0.253}{\frac{foF2}{foE} - 1.215} - 0.012 & ; & \text{if} f0E \neq 0 \\ -0.012 & ; & \text{if} f0E = 0. \end{array} \right\} \tag{4.2.11}$$

The thickness parameters take different values for top and bottom anchor points. The thickness parameters for the bottom of Epstein layer E region is $B_{bot,E} = 5km$ and the top side of the Epstein layer of the E region $B_{top,E} = 7km$ during night time if F1 is not present. But in the presence of F1 during day time $B_{top,E} = 0.5B_{top,E}$ in km. For the bottom side semi-Epstein layer of the F1 is given by $B_{bot,F1} = 0.7B_{top,F1}$ while the thickness value of top side of F1 is calculated using Eq. (4.2.12):

$$B_{top,F1} = \frac{h_{max,F2} - h_{max,F1}}{ln(4\frac{n_{max,F1} - nF2(h_{max,F2})}{0.1N_{max,F1}})} \tag{4.2.12}$$

In the semi-Epstein layer of the F2 region, the thickness parameter of the bottom side depends on the value of the peak electron density, $n_{max,F2}$ and the maximum vertical gradient of the electron density $max(\frac{dn}{dh})$ in the ionosphere. Therefore the thickness parameter for the bottom side of F2 is expressed by Eq. (4.2.13).

$$B_{bot,F2} = \frac{0.385n_{max,F2}}{max(\frac{dn}{dh})} \tag{4.2.13}$$

The data set used in the study consist of minutes values of geomagnetic elements: X, Y and Z recorded at the Observatories. The horizontal component of the geomagnetic field intensity H is calculated using conversion formula, $H = (X^2 + Y^2)^{\frac{1}{2}}$. This data is again averaged to hourly mean values. The data were analyzed for geomagnetically quiet days to analyze the diurnal variation of EEJ. The concept of local time was used in the analysis. The observatories are 3 hrs ahead of Greenwich mean time and thus, the baseline value is defined as the average of the 4 hours flanking local midnight (20, 21, 22, 23hrs) UT because 1 hr local time (LT) in Ethiopia is 22 hrs universal time in (UT) and these values are equivalent to (1, 2, 23, 24 hrs) LT . The base line values used for our purpose are:

$$H_0 = \frac{H_{20} + H_{21} + H_{22} + H_{23}}{4} \tag{4.2.14}$$

The hourly departures of H from the midnight baseline values is obtained by subtracting the midnight base line values for a given hourly values of the day [68, 69]. So for time t=1:24 hours, we have $\triangle H_t = H_t - H_0$. The hourly departure is further corrected for non-cyclic variation $\triangle c = \frac{\triangle H_1 - H_{24}}{23}$ [70] in our case $\triangle c = \frac{\triangle H_{22} - H_{23}}{23}$. So the linearly adjusted at the 24 hours time is given by $Sq_t = \triangle H_t + (t-1) \triangle c$ which describes the solar daily variation in H called solar quiet daily variation in H. The EEJ is now calculated using the parameter $EEJ = Sq_{AAE} - Sq_{ADI}$. Where Sq_AAE and Sq_ADI are Sq currents at Addis Ababa and at Adigrat respectively.

The geomagnetic disturbance during 22-25 January 2012 is characterized using observational data analysis such as the variations of the SYM-H, AE index, the solar wind proton speed (V_p), the interplanetary magnetic field (B_z, proton temperature, proton density, flow pressure, proton flux events, percentage deviation of vertical TEC with respect to median TEC of a few geomagnetically quiet days before the storms, variation of the h_mF_2 as observed by ionosondem spatial variation of time of abrupt TEC changes and modulation diurnal and semidiurnal tides in TEC in response to the geomagnetic storms. The Global variation of TEC during ionospheric perturbation is studied by creating differential maps explained by Eq. (4.2.15).

$$DTEC = (\frac{TEC - TEC_{median}}{TEC_{median}}) \times 100\% \tag{4.2.15}$$

The TEC data covers a period from January 13 to February 4, 2012. The median TEC is evaluated from a period covering January 13-20, 2012. The TEC differential maps are analyzed based on TEC maps of temporal resolution of 15 minute as well as based on daily mean maps.

Atmospheric tides, planetary waves and gravity waves play significant role in dynamic features of the Mesosphere and Lower Thermosphere (MLT) region by transporting energy and momentum horizontally and vertically upward and also providing dynamical linkage between the lower atmosphere and the MLT region. Atmospheric tides are the global response of the atmosphere to the periodic forcing of solar heating; propagate westward following the motion of the Sun with periodicities equal to the solar day and its sub-harmonics (i.e., 24, 12, 8, 6, 4, 3, 2 hr, etc). Tides are classified as migrating and non-migrating. The non-migrating tides lead to strong longitudinal variations in amplitude and phase of diurnal tide, whereas the migrating tides contain diurnal, semidiurnal, terdiurnal and other higher harmonics. The diurnal (24 hr period) tide is mainly excited by the direct absorption of the sun light by water vapor in the troposphere and the stratosphere, whereas the semidiurnal tide (12 hr periods) is caused by ozone heating in the upper stratosphere and the lower mesosphere.

Studies of the diurnal and the semidiurnal tides and its influences in the mesospheric region at various geographical locations have been made using lidar, airglow emissions and space-based airglow observations. However, how these waves are modulated by the geomagnetic storm was not given due consideration.

One way to understand the ionospheric response to geomagnetic storm is to investigate how the dominant coherent mode of spatio-temporal variation of the amplitude of the atmospheric tides is modulated by the storms. The diurnal and semidiurnal modes are the dominant modes of TEC variation in relation with photoionization during all times. However, the geomagnetic storms may modulate these modes of variations. To investigate the modulation, we investigated the temporal variation of amplitudes of westward propoagating diurnal and semidiurnal tides. To assess whether these two tides account for much of TEC variability and then justify further analysis to see impact of geomagnetic storms in them, we employed Multitaper-multivariate Singular Value Decomposition (MTM-SVD) statistical spectral method. MTM-SVD is a spectral technique which produces a spectrum of variance within which significant narrow band peaks are identified [71, 72]. The method can isolate independent modes of variability superimposed on a noise background of stochastic variability. It has been widely used in climate research to isolate transient and episodic variation from regular cyclic and secular long term changes. Moreover, the MTM-SVD method has also been used to investigate joint spatio-temporal variability of climate drivers and climate signal [71, 72, 73, 74, 75, 76, 77]. This method identifies the frequencies that are statistically significant among a large number of normalized independent series (e.g., multiple grid points), that is, those that contribute with a significant fraction of the total data variance. The (MTM-SVD) transforms the data series from the time to the spectral domain, using a multitaper spectral analysis. For this, a small number of (K) Slepian tapers are applied on the data series, in order to obtain K independent spectral estimates of the data series by the calculation of the tapered Fourier transform at a given frequency as:

$$Y_k^{(m)}(f) = \sum_{n=1}^{N} W_n^{(k)} x_n^{(m)} \exp i2\pi f \Delta t \tag{4.2.16}$$

Where Δt is the time interval and $W_n^{(k)}$ is the k^{th} member in an orthogonal sequence of K Slepian tapers. The Slepian tapers are mutually orthogonal, the spectral estimates are statistically independent leading to multiple degree of freedom and better accuracy compared to most of the standard spectral techniques. To isolate spatially-coherent narrow band processes, a matrix $A(f) = [Y(m)_1, Y(m)_2, ...Y(m)_k]$ is constructed from the spectral estimates for each frequency point f as

$$A(f) = \sum_{k=1}^{K} \lambda u_k(f) * v_k^{'}(f) \tag{4.2.17}$$

into K orthogonal M-vectors u_k, that represent the complex empirical orthogonal functions (CEOFs) in the spatial domain, and K orthonormal vectors v_k that represent the CEOFs in the spectral domain. The prime in Eq. (4.2.17) represents transpose. Then a complex SVD is performed on A matrices. The resulting normalized singular values from the first mode ($\frac{\lambda_1^2}{\sum \lambda^2(f)}$) are proportional to the variability on each sampling frequency f and are used to build the power spectra of local fractional variability (LFV). The two dominant modes of TEC variability namely diurnal and semidiurnal tides used to assess the ionospheric response to geomagnetic storm influences are extracted from global GPS TEC data covering January 13 to February 4, 2012. The extraction is based on linear two dimensional (time-longitude) least squares fitting method ([78] and references therein) with a window of 4-day moved through the time series with a step of 1-day in order to obtain daily values of the wave characteristics. The following components are included in the fitting: (i) zonal mean

TEC, (ii) linear trend term, (ii) migrating 12-hrs (W2) and 24-hrs (W1) tides as well as other higher harmonics, (iv) the first four modes of the stationary planetary waves (SPWs) (i.e. SPWs with zonal wavenumbers 1, 2, 3 and 4) and (v) the vacillation terms to describe oscillations of the zonal mean at all frequencies in (ii) above

The time and longitude coupling in a rotating atmosphere through thermal heating and their response can be expressed by the tidal wave equation

$$\sum_{s=-L}^{s=L}\sum_{n=1}^{n=N} A_{n,s}(\theta,h)\cos(n\omega t + s\lambda - \Phi_{n,s}(\theta,h)) \tag{4.2.18}$$

Where t=time in UT hours, ω = rotation rate of the earth=$\frac{2\pi}{day}$, λ =longitude, n=1, 2, 3, ..., which denotes subharmonic of the day, $A_{n,s}$ = Amplitude of the wave, s integer zonal wave number, h =altitude and $\phi_{n,s}$ is the phase. The local time can be related to the universal time (UT) by:

$$t_{LC} = t + \frac{\lambda}{\omega} \tag{4.2.19}$$

therefore the tidal wave component in equation(4.2.18) can be expressed in the form:

$$A_{n,s}(\theta,h)\cos(n\omega t_{LC} + (s-n)\lambda - \Phi_{n,s}(\theta,h)) \tag{4.2.20}$$

Eq. (4.2.20) enables us to identity clearly whether the tidal wave is migrating or non-migrating tide. For example when $s = 0$ the oscillating wave does not propagate with longitude and is called standing wave or zonally symmetric wave. On the other hand the condition $s \neq 0$ means the tidal global wave propagation is westward for $s > 0$ and eastward propagation for $s < 0$.

A wavelet is defined as a series of functions $\psi_{u,s}(t)$ derived from a function W(t) by shifts in the translations and dilations that act on the frequency variable as follows

$$\psi_{u,s}(t) = \frac{1}{\sqrt{s}}\psi(\frac{t-u}{s}), s \neq 0, u, s \in R \tag{4.2.21}$$

where W is a so-called mother wavelet, and s and u denote the dilation and translation parameters, respectively. If $f(t)$ is an energy-limited signal, then the continuous wavelet transform can be expressed as

$$W(u,s) = \frac{1}{\sqrt{s}} \int_{-\infty}^{+\infty} f(t)\psi^{*}(\frac{t-u}{s})dt \tag{4.2.22}$$

The signal to be analyzed are discrete. Therefore, the continuous form of the wavelet should be changed in to a discrete form [79].

If $A_0(n); n \in Z$ denotes a discrete signal of ionospheric TEC, the decomposition can be calculated by

$$A_j(n) = \sum_{k \in z} h_k A_{j-1}(n - 2^{j-1}k) \tag{4.2.23}$$

$$D_j(n) = \sum_{k \in z} g_k D_{j-1}(n - 2^{j-1}k) \tag{4.2.24}$$

and the reconstruction of the original signal A_0 uses a discrete dyadic wavelet transform. The calculation can then be performed by

$$A_{j-1}(n) = \sum_{k \in z} \tilde{h}_k A_j(n - 2^{j-1}k) + \sum_{k \in z} \tilde{g}_k D_j(n - 2^{j-1}k) \tag{4.2.25}$$

where j=(=1,...,J) are the times of decomposition, $\{h_k\}k \in Z, \{g_k\}k \in Z$ and $\{\tilde{h}_k\}k \in Z, \{\tilde{g}_k\}k \in Z$ are discrete filters and conjugate filters obtained from the basic function $\psi(t)$ and the corresponding scaling function $\psi_{u,s}(t)$, respectively. A_j and D_j are called the discrete approximation and the discrete detail at the j^{th} level or at the resolution of 2^j with respect to A_0, respectively. A_j is the low frequency part of signal A_0 with a frequency lower than 2^{-j}, and D_j is the high frequency part of the signal with the frequency between 2^{-j} and 2^{-j+1}. For the decomposition of each GIM pixel, the A_j and D_j values are the different frequency components of the original ionospheric signal.

We also employed the Eliassen-Palm (EP) flux diagnostics to see weather the heat flow is correlated or not. The separation of the flow into its zonal average and the deviations there from has been a dominant paradigm for analysis of the general circulation. EP theory provides an elegant frame work with which to understand the eddy-mean flow interaction. The EP flux can be written in pressure coordinates on the sphere as

$$F = \{F_{(\phi)}, F_{(p)}\} = a\cos\phi\{-\overline{u'v'} + \psi\frac{\partial\bar{u}}{\partial p}, -\overline{u'w'} - \psi[\frac{\partial(\bar{u}\cos\phi)}{a\cos\phi\partial\phi} - f]\} \tag{4.2.26}$$

where

$$\psi = \frac{\overline{v'\theta'}}{\frac{\partial\bar{\theta}}{\partial p}} = -\frac{\overline{v'T}}{(\frac{k\bar{T}}{p} - \frac{\partial\bar{p}}{\partial p})} \tag{4.2.27}$$

In the above expression as explained (see e.g. [80, 81]), the quantities ϕ, p, represent the latitude and pressure, (u, v, w) represent the velocity in (longitude, latitude, pressure) coordinates. The others θ is the potential temperature, T is the temperature, a earth's radius, f is coriolis parameter and k is the ratio of the gas constant to the specific heat at constant pressure. The overbars represent zonal Eulerian averages at constantϕ and p while the prims denote departure thereform. The isobaric divergence of F is given by

$$\nabla \cdot F = \frac{\partial(F_{(\phi)}\cos\phi)}{a\cos\phi\partial\phi} + \frac{\partial F_{(P)}}{\partial p} \tag{4.2.28}$$

F may be regarded as of the net rate of transfer of wave activity from one latitude and height to another and leads to the conservation equation related to F and this can be written as

$$\frac{\partial A}{\partial t} + \nabla \cdot F = D + \varepsilon \tag{4.2.29}$$

where A can be regarded as conservable motion of local wave activity called density of wave activity. So that $\frac{\partial A}{\partial t}$ represents wave transience and D represents conservative effects like dissipation or forcing in the wave while ε is non linear effect and vanishes for purely linear waves.

Eq. (4.2.29) is not conservative form. However, it can be transformed by involving further terms representing exchange of energy between the waves and the mean flow [81, 80, 82, 83]. In this case F appears in a transformed version of the mean flow equation. Therefore the Eulerian-mean flow of the zonally -averaged zonal momentum equation is:

$$\frac{\partial \bar{u}}{\partial t} = \{-(\frac{\partial(\bar{u}\cos\phi)}{a\cos\phi\partial\phi} - f)\bar{v} - \frac{\partial \bar{u}}{\partial p}\bar{\omega}\} + \{-\frac{\partial(\overline{u'v'}\cos^2\phi)}{a\cos^2\phi\partial\phi} - \frac{\partial(\overline{u'\omega'})}{\partial p}\} + \bar{X} \tag{4.2.30}$$

where $\bar{X}$ is any mean non conservative force. By introducing the residual mean meridional circulation.

By introducing the residual mean meridional circulation

$$\bar{v^*} = \bar{v} - \frac{\partial\psi}{\partial t}, \bar{\omega^*} = \bar{\omega} + \frac{\partial(\psi\cos\phi)}{a\cos\phi\partial\phi} \tag{4.2.31}$$

one can obtain the transformed mean zonal momentum Eq (4.2.32):

$$\frac{\partial \bar{u}}{\partial t} = \{-(\frac{\partial(\bar{u}\cos\phi)}{a\cos\phi\partial\phi} - f)\bar{v^*} - \frac{\partial \bar{u}}{\partial p}\bar{\omega^*}\} + \{\frac{1}{a\cos\phi}\nabla\cdot F\} + \bar{X} \tag{4.2.32}$$

The objective of this work is to calculate Eliassen-Palm (EP) Flux and divergence for use as diagnostic tools of wave activity between 10-1 hPa pressure level and plot in the meridional plane, arrows representing the EP flux vector F and contours of the divergence with the help of a general description of the wind and temperature data profile.

Chapter 5

GPS and ionosonde observations of total electron content (TEC)

5.1 TEC as a parameter for diurnal variation

The slant TEC measured at every 1-min interval from the data of the GPS receivers are used to study temporal and spatial variations of TEC in the Ethiopian region. The diurnal variation of the electron density can be studied using TEC parameters. Fig. 5.1 shows the diurnal variation of the TEC on one particular day. TEC value has its maximum at noon time and is very low during night time. The plot shows TEC versus time for low latitude ionosphere from 3^0 to 17^0 latitude for day 4 January 2012 at elevation mask angle 15^0 at Addis Ababa. The TEC variation is not only time dependent it also depends on latitude. The variations with low nighttime TEC value and peaks at noontime is the typical behavior of the ionosphere. As the sun is the main source of ionization most TEC variations are resulted due to the activity of the sun. However, the modifications of the atmosphere from below can not be neglected. So the influence of atmospheric forces from below in modulating the Global TEC is explained.

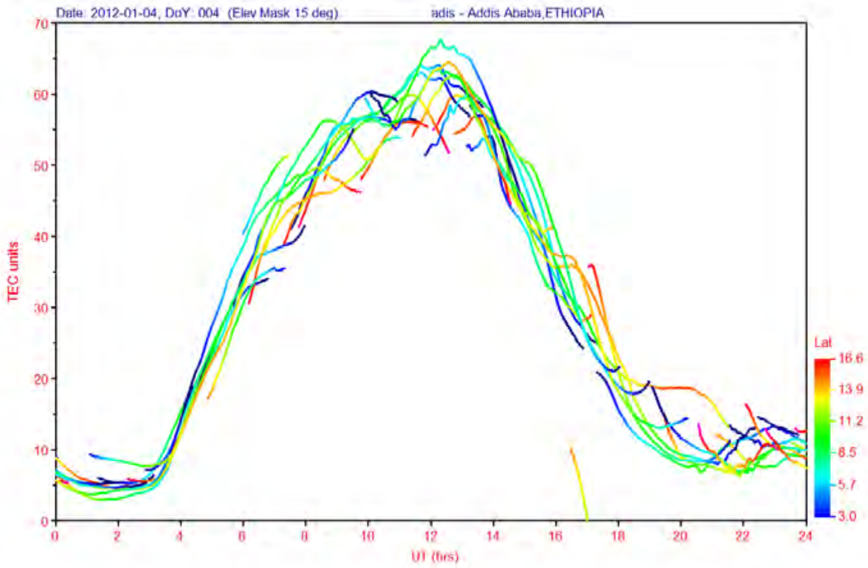

Figure 5.1: Mass plot of TEC from SCINDA GPS station at Addis Ababa

The global TEC is analyzed from the world map TEC value to observe the time dependence of the ionosphere. For example Fig. 5.2 represents global diurnal variation of TEC. At t=0 hr in UT maximum TEC is stratified over west African region all the way to through the Atlantic Ocean up to east American regions which is day time at these regions and Asia and Pacific ocean show small TEC value which are dusk time zone. 4 hrs later the TEC is migrated to the west and covers Atlantic ocean, central America regions and some parts of the Pacific ocean leaving Indian ocean dark with very small TEC value. After 8 hrs Pacific ocean has maximum TEC leaving Africa under darkness. After 12 hrs the Pacific ocean has maximum TEC value and Atlantic ocean becomes the least TEC value region which is exactly opposite to the event at 0 hr time. This result clearly shows noon hour TEC is synchronously moving westward

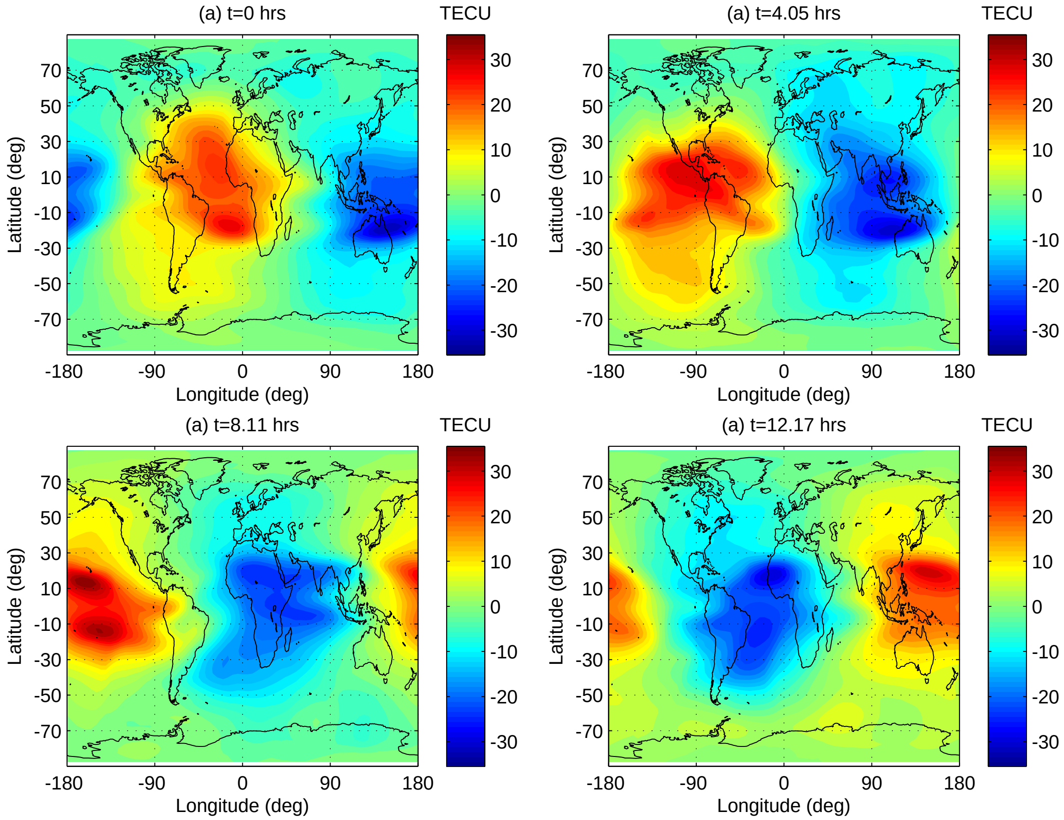

Figure 5.2: The Diurnal variation of TEC

with the sun over the 24 hrs interval of time. It should also be noticed that the peak electron density crests reach 30 TECU with trough at the geomagnetic equator. This is the typical behavior of the equatorial ionization anomaly of the noon hour time. The semidiurnal global TEC variation was also analyzed during the quiet days. The Fig 5.3 shows the global semidiurnal variation of TEC phases. In this regard two peaks every 2 hrs are shifting along the longitude every 12 hours. This may be modulated by the semidiurnal tidal oscillation in the stratosphere. The westward two peaks motion of the TEC every two hour covers the whole globe in every 12 hrs and

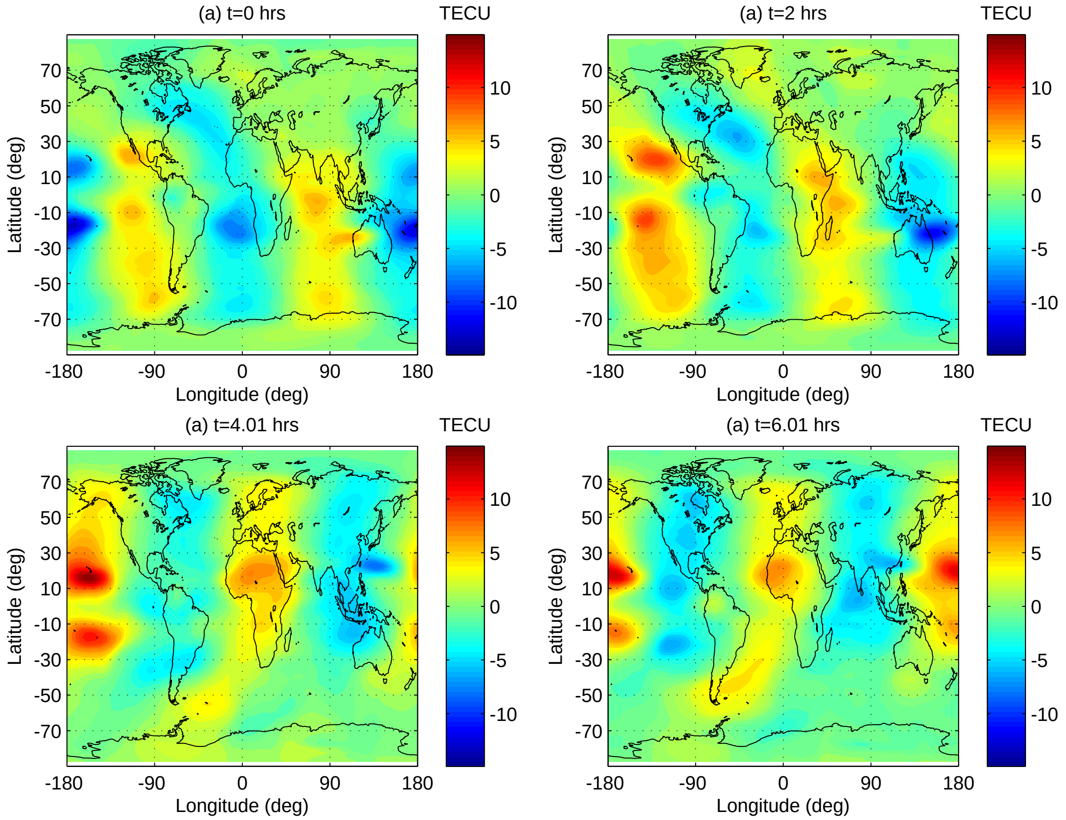

Figure 5.3: The Semidiurnal variation of TEC

this is modulated by the westward migrating semidiurnal tides. These tides are originated from the lower thermospheric regions. As observed in the diurnal variation the maximum TEC value has two peaks with trough at the geomagnetic equator. The peak TEC value at the crests is about 10 TECU.

Terdiurnal westward wave number 3, TW3 signature in ionospheric total electron content (TEC) is analyzed as follows. Our investigations are based on the global ionospheric maps. The absolute amplitude of TEC modulated by TW3 exhibits maximum values in the magnetic equatorial region, which reaches about 6 TECU under

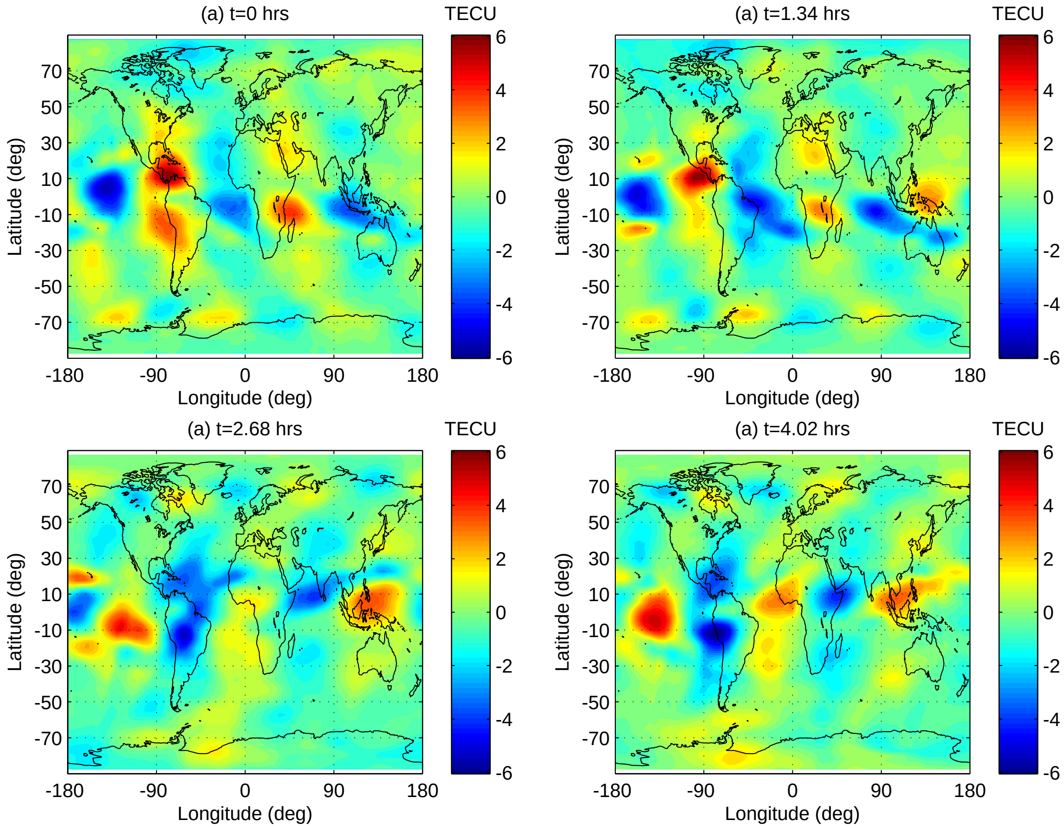

Figure 5.4: The teridiurnal variation of TEC

high solar activity during our observation time. Fig. 5.4 represents the TEC modulated by wave number 3. The absolute amplitude of TW3 exhibits maximum values in the magnetic equatorial region, which reaches about 6 TECU and at high latitude regions the maximum TEC value reaches 2 TECU. The global structure of TW3 signature in TEC should shed some light on the coupling between the ionosphere-thermosphere and the lower atmosphere.

The four peaks of TEC observed in Fig. 5.5 show a westward motion every 1 hour shows during the cycle of 6 hrs. The distribution of this TEC along the a given longitude does not show significant change. The four peaks of TEC are separated by 90^0 each and we find four enhanced peaks along longitude circle. The peak TEC value at the equatorial ionization anomaly is about 3 TECU. The main source of these four peaks during a cycle of every 6 hrs is TEC modulated due to the westward wave number 4.

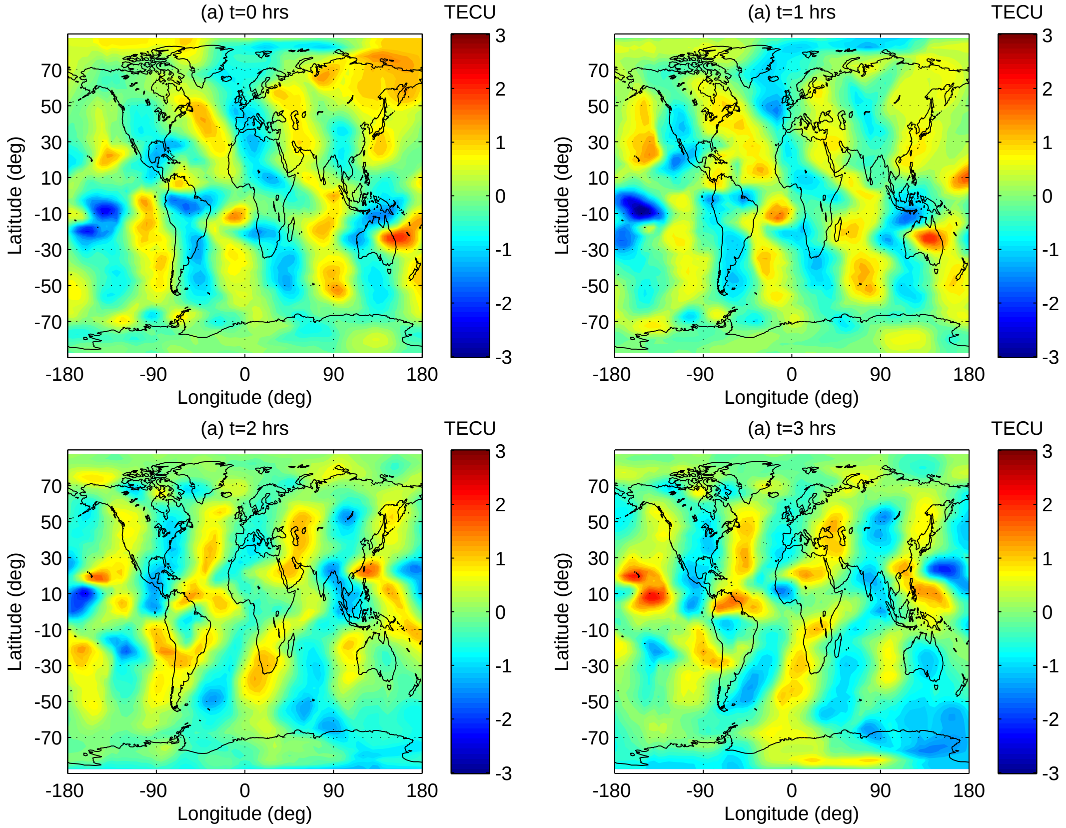

Figure 5.5: The quaterdiurnal variation of TEC

5.2 Seasonal variation of TEC

The TEC value depends on seasons. Fig. 5.6 are plots of TEC versus time for six days selected from six months for a single GPS receiver station located at 3 N latitude and 18 E longitude, a place called Arba Minch in southern part of Ethiopia. We use this particular place because of the continuous data availability for six months. The plots

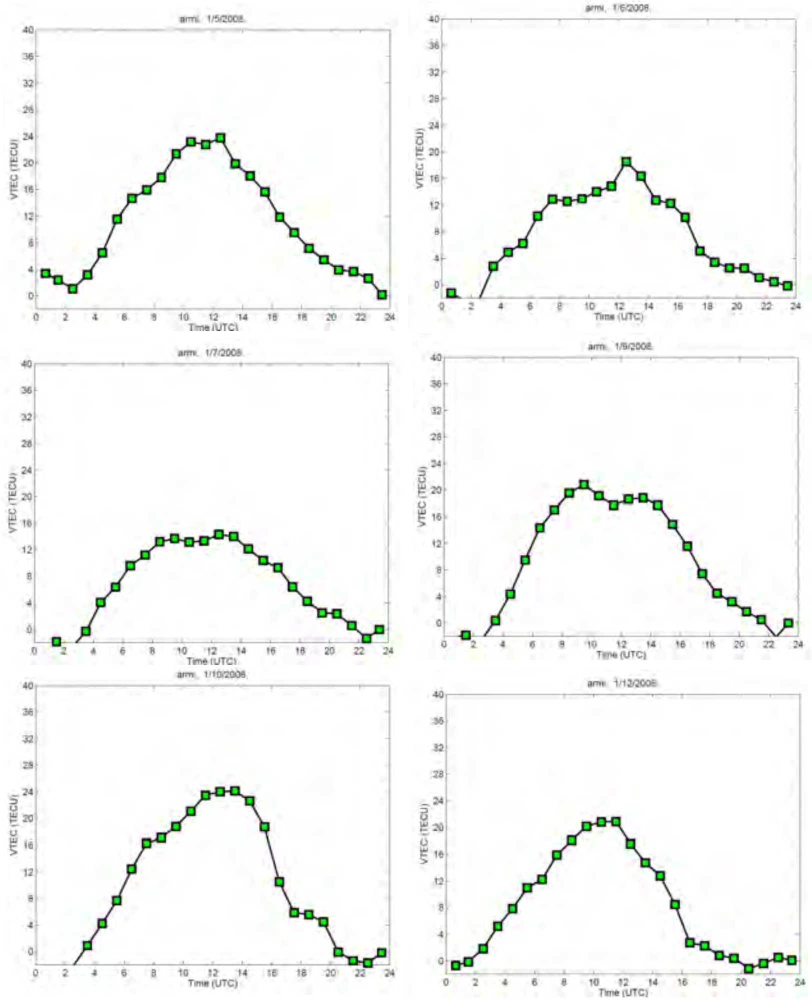

Figure 5.6: The vertical TEC values on May 1 (top-left), June 1(top right), July 1 (middle left), September 1 (middle right), October 1(bottom left), December 1,(bottom right) respectively

show that there are significant VTEC differences in both magnitude and pattern over 6 months period. The daytime TEC value is larger than the nighttime values. But the occurrence time of the maximum/minimum ionosphere TEC values varies with seasons. In all months the TEC value is maximum near noon and of all months the highest TEC is obtained in the month October where the time is around noon and its value is about 26 TEC units and its minimum is at the month 7 about 15 TEC units. The position of the sun relative to the equator affects the ionization process in the ionosphere because the intensity of ionization depends on the solar zenith angle. That is when the sun is at different positions the solar zenith angle changes so the rate of production will be changed. When the sun is at horizon the intensity reaching the equatorial ionosphere is relatively small compared to the intensity reaching at the equatorial ionosphere from the overhead sun.

5.3 Latitudinal variation of TEC

TEC values for different regions of Ethiopia are compared for the same Day of year (DOY). The Fig. 5.7 show the latitudinal variation plots of TEC for a typical day at different latitudes of Ethiopia. Table 4. below represents the locations of GPS receivers of Ethiopia in geographic latitude and longitudes and one GPS station from Uganda used for relative comparision.

Station name	Latitude	Longitude
Addis Ababa	9.034^0	38.766^0
Arba Minch	6.062^0	37.561^0
Mekelle	13.29^0	39.28^0
Semera	11.779^0	41.009^0
Mbarara	-0.601^0	30.73^0

Table 4: GPS station locations in latitude and longitude

A time series of the vertical TEC (VTEC) for 2008 at different stations of Ethiopia is analyzed. The solar-geographical reference frame is adopted to estimate the TEC model parameters. The X-axis and Y-axis represent the local time for the day and the VTEC value respectively in each panel. Each panel represents VTEC variations in a day in the corresponding month (1st of the 7th month/2008). The Figs. (5.7) show a time series of 24 hrs which is diurnal VTEC variations for a single day over three stations of Ethiopia and over one station of Uganda. By comparing all the panel, one can see that there are significant VTEC differences in both magnitudes and patterns over day one of July/2008. The maximum VTEC is obtained at the day time near noon. For further comparison we have also observed one GPS station outside Ethiopia at further south located at Uganda latitude -0.601^0 and longitude 30.73^0. As it is known the intensity of the sun's radiation is influenced by the angle of the sun's rays striking the atmosphere, maximum TEC is observed from Mekelle station and the Minimum is from Mbarara station. So at noon time the intensity of light from the sun is relatively large compared to the other hours of the day. Thus photo-ionization processes are maximum and maximum TEC is obtained at noon time. During the night time the value of TEC is very small because electrons lost as a result of the recombination processes and also due to ion drifts mechanisms. However, the TEC value everywhere is not the same at the same time. To see the latitude variation of TEC, we considered the TEC values at different locations of Ethiopia for the same day. Fig. 5.7 are the measured TEC values from GPS receivers at Arba Minch (south of Ethiopia), Mekelle (north of Ethiopia), Semera (north east of Ethiopia) and Mbarara at Uganda out of Ethiopia which at 0.601^0 south respectively. As it is clearly seen in the graphs the maximum TEC value at Arba Minch is about 15 TECU while that of Mekelle is about more than 17 TECU. The main reason for the fluctuation observed here is due to the position of the sun. The sun appears to move northward during the northern spring. Its declination reaches a maximum equal to the angle of the Earth's axial tilt (23.44^0) on the June solstice, then decreases until the December solstice, when its value is the opposite of (-1 times) the axial tilt. This variation produces the seasons. During the June solstice (also called the summer solstice in the Northern Hemisphere), all locations north of the equator have day lengths greater than twelve hours, while all locations south of the equator have day lengths less than twelve hours. So when the sun is above the northern hemisphere, the solar zenith angle relative to the reference point is small so the ionization radiation is large. Therefore, on July 1 the sun is on the northern hemisphere. So Mekelle is relatively on the northern hemisphere near to equatorial ionization anomaly region compared to Arba Minch which is nearly at equator. For comparison we also used the Mbarara GPS station at Uganda outside Ethiopia southwards and the value of TEC from that station is very low 12 TECU which supports the latitude dependence of TEC.

5.4 TEC climatology from NeQuick and comparison to ionosonde observations

NeQuick2 model is an empirical model uses the effective ionization level (A_z) as an impute value to compute electron density from STEC values by means of numerical integration along the ray path. The Model prediction of the electron density

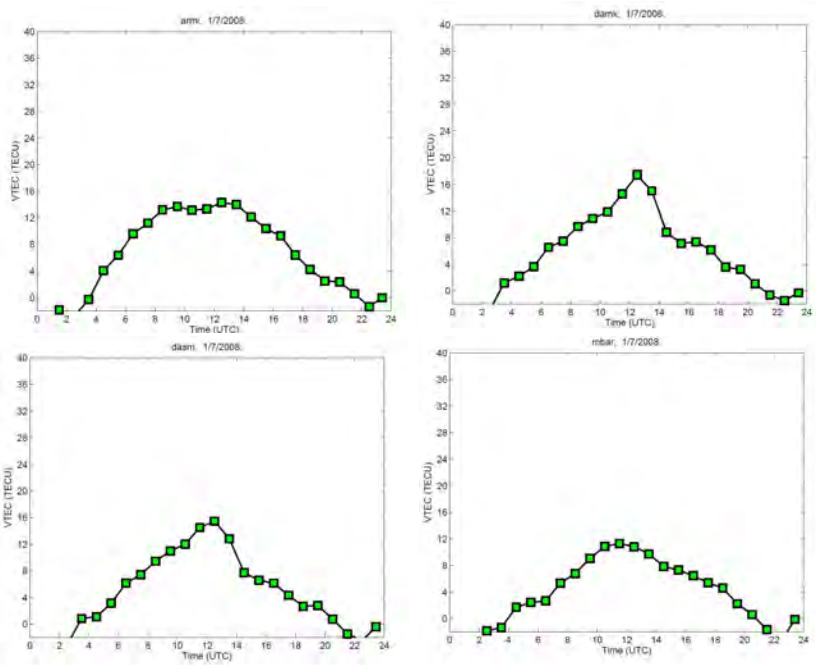

Figure 5.7: Diurnal variation of TEC as observed at stations of Arba Minch (top left), Mekelle (top right), Semera (bottom left), Mbarara (bottom right) respectively on July 1, 2008

distribution at a given time can be plotted as a function of height. The Model predicts that the maximum electron density is obtained at noon time and the minimum electron density is obtained at night time as indicated in Fig. 5.8. However, in the east African sector due to lack of instruments the performance of NeQuick and other models is not evaluated very well. For the first time Nigussie et al [84], tried to model the east African equatorial ionosphere using TEC data ingestion technique into NeQuick2 model for low solar activity of the year 2007, and they have shown that NeQuick2 has the capability of describing the characteristics of low equatorial ionosphere in the African sector and the result can be improved well by assisting the model with data ingestion. NeQuick2 is the modified version of NeQuick ionospheric electron density Model developed at ICTP, Trieste Italy later improved by [63] in

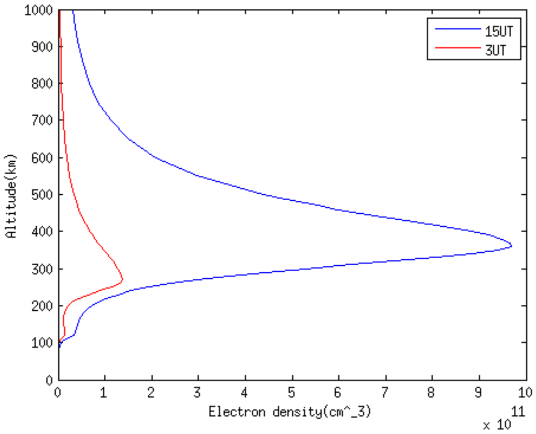

Figure 5.8: Electron density vertical distribution for day time at 15 UT blue color and for night time 3 UT red color at Addis Ababa on day 12 Jan/2012

collaboration with University of Graz of Australia [58, 65]. It is designed for use in trans-ionospheric propagation and includes routines to compute slant total electron content (STEC) values by means of numerical integration along the ray path. The details are explained in the previous section. The predicted electron density is then compared with ionosonde derived electron density profile. However, the topside ionospheric electron density can not be measured by ionosonde. So only the E and F regions are compared for quiet and disturbed days depending on the data availability. In the present study we restricted to specific days 12, 16, 25, and 27 of January 2012 because our ionosonde data is only limited to these days only. First we checked the Disturbance storm time (Dst) index, and we found that there was a moderate geomagnetic storm on day 25 with Dst index value of -80 nT as shown in Fig. 5.9, while the other days were geomagnetic quiet days. The severity of geomagnetic storms is usually explained with the help of Dst index as well as weighted average of K-indices from a net work of geomagnetic observatories (Kp index). As it was indicated by

Kim et al [85], from the initially observed CME parameters, it is possible to forecast geomagnetic storm prediction for real time which will allow us to make an earlier warning of specific Dst minimum levels of geomagnetic storm 2-3 days in advance before it occurred. We analyzed the vertical electron density distribution first for the geomagnetic quiet days for different local time. The Fig. 5.10 show that the electron density structure obtained from the ionosonde data is well captured and well agreed with the result from TEC ingested NeQuick2 electron density to describe the electron density structure up to the F2 peak for these quiet days.

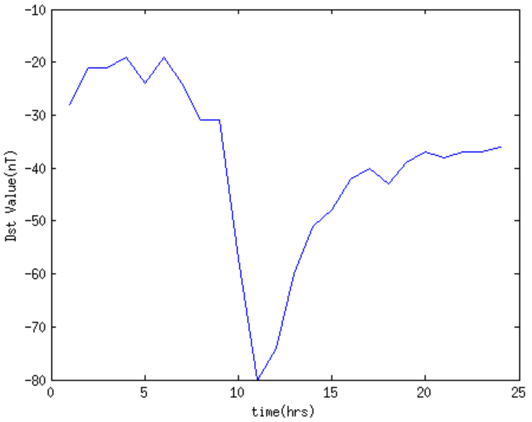

Figure 5.9: Dst index for the January 25,2012 generated by WDC - Kyoto

At early morning hours (Fig. 5.11), the electron density structure observed by the the ionosonde and simulated by ingesting GPS TEC into NeQuick2 model show good agreement but in the afternoon hours results begin to disagree. On the other hand the electron density from ionosonde data (Fig. 5.11 (bottom left)) shows a spread F phenomena which is an indication of geomagnetic disturbance. This is also clearly shown on the ionograms while electron density obtained from NeQuick2 show the same

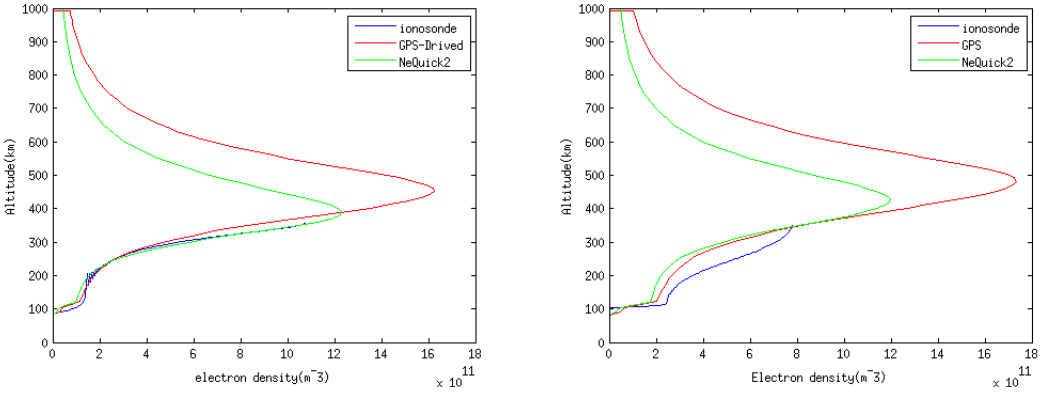

Figure 5.10: Comparison of electron density measured by ionosonde and by simulated NeQuick2 model based on ingested GPS TEC on January 16, 2012 at 13.45 UT, January 27 at 8:45 UT (left -right)respectively

trend except the magnitude difference. So the GPS TEC ingested NeQuick2 does not describe the true structure of ionospheric electron density during the disturbed days. On the other hand the NeQuick2 model for the undisturbed days of the low latitude region ionosphere agrees with that of the ionosonde electron density. But the result obtained is conclusive because the data size of the ionosonde is not large enough and also the data is not calibrated. But for the future work when the ionosonde is fully operational we will come up with a detailed analysis and a better conclusion can be given on the performance of the NeQuick2 at low latitude regions in the African sector.

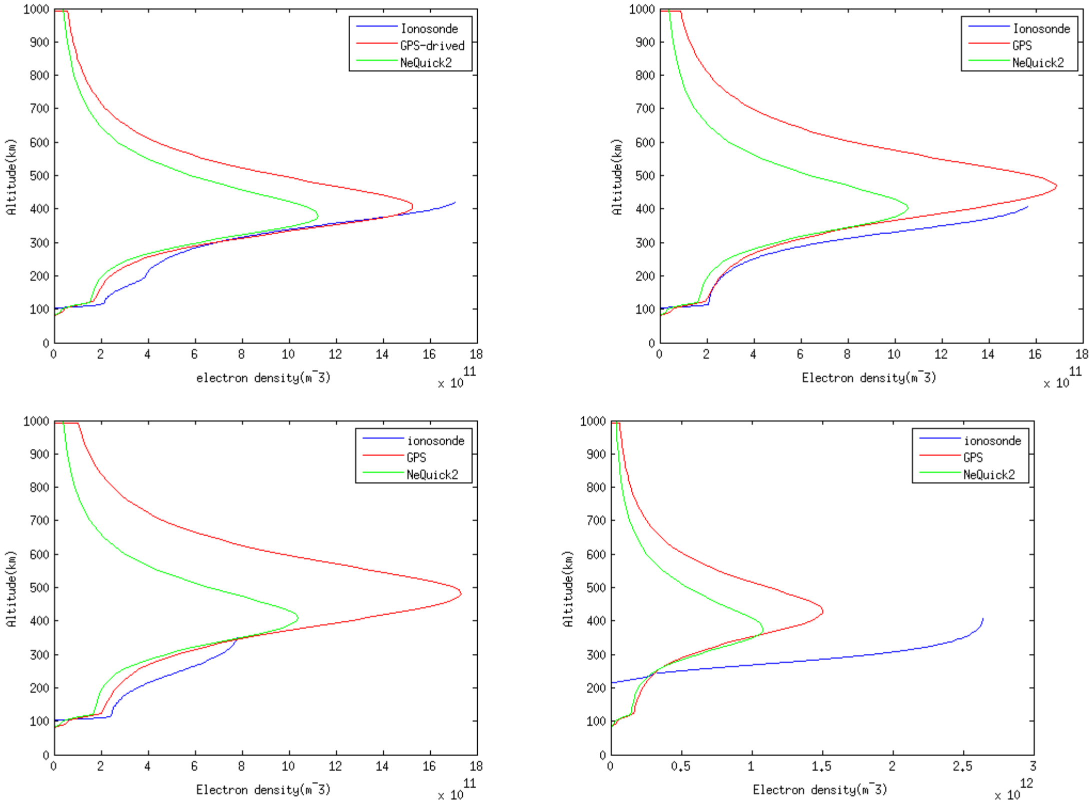

Figure 5.11: Comparison of electron density measured by ionosonde and by simulated NeQuick2 model based on ingested GPS TEC on January 25, 2012 at 7.41 UT (top-left), 8:25 UT (top-right), 8.45 (bottom-left), 12.00 UT (bottom -right)respectively

Chapter 6

Equatorial electrojet, its counter and prereversal enhancement from ground based magnetometers

Geomagnetic field components X, Y and Z are recorded at stations of Addis Ababa geographic lat/long [9.030N/38.760E], geomagnetic latitude /longitude$[0.17^0 N, 110.47^0 E]$ from intermagnet magnetometer and Adigrat station geographic lat/long $[14.28^0 N, 39.46^0 E]$, geomagnetic latitude/longitude $[6.0^0 N, 111.06^0 E]$ from AMBER magnetometer respectively. The recorded values of the X, Y and Z components are converted into H, D and Z components. The hourly mean values of the H components are analyzed to study the diurnal and seasonal variability of the equatorial electrojet (EEJ) at Addis Ababa station. It has been a long established fact that daily variations of the magnetic fields on the ground level are caused by the dynamo action in the upper atmosphere called ionosphere. Chapman [86] suggested that these daily variations in the magnetic field at the earth's surface during geomagnetically quiet conditions are known to be associated with dynamo currents originated by winds and tidal forces in the E region of the ionosphere. Polarization fields are created by differences in ion and electron numbers of 1 in 10^8 . Polarization fields are created on time scales of 10^{-6} seconds [42]. At the magnetic dip equator the eastward polarization electric field produced by the global dynamo action drives a downward Hall current and a vertical polarization electric field is set up to nullify the down ward flow of current due to the presence of non-conducting boundaries [87]. Again this field in turn gives rise to another intense Hall current which Chapman in 1951 named the equatorial electrojet (EEJ). The EEJ is caused by the ionospheric current flowing along a narrow band ($\pm 3^0$ in geomagnetic latitude range) of the enhanced ionospheric conductivity (Cowling conductivity), which is formed along the day side dip magnetic equator. The data obtained from the geomagnetic observatory at Huancayo geomagnetic observatory in Peru facilitated the discovery of EEJ for the first time in the American sector and it has been also routinely analyzed in the Indian sector too by earlier researchers [52, 88, 89]. The equatorial electrojet current can be estimated from $\triangle H$. The vertical $E \times B$ drift by the zonal and horizontal northward magnetic field significantly affects the structure and dynamics of the equatorial F-region ionosphere. The vertical $E \times B$ drift is generally upward during the daytime and downward during the nighttime. During the daytime, the eastward electric field is mainly generated by the E-region dynamo. The dynamo electric field simultaneously drives a zonal current in the E-region which is responsible for the enhancement of EEJ [52]. In this PhD dissertation we use a set of geomagnetic data obtained at Addis Ababa station and Adigrat stations to examine the solar daily variations in geomagnetic horizontal intensities under quiet conditions.

6.1 Daily variation of EEJ

Fig. 6.1 show diurnal variation of EEJ for some selected days. In the plots ADI stands

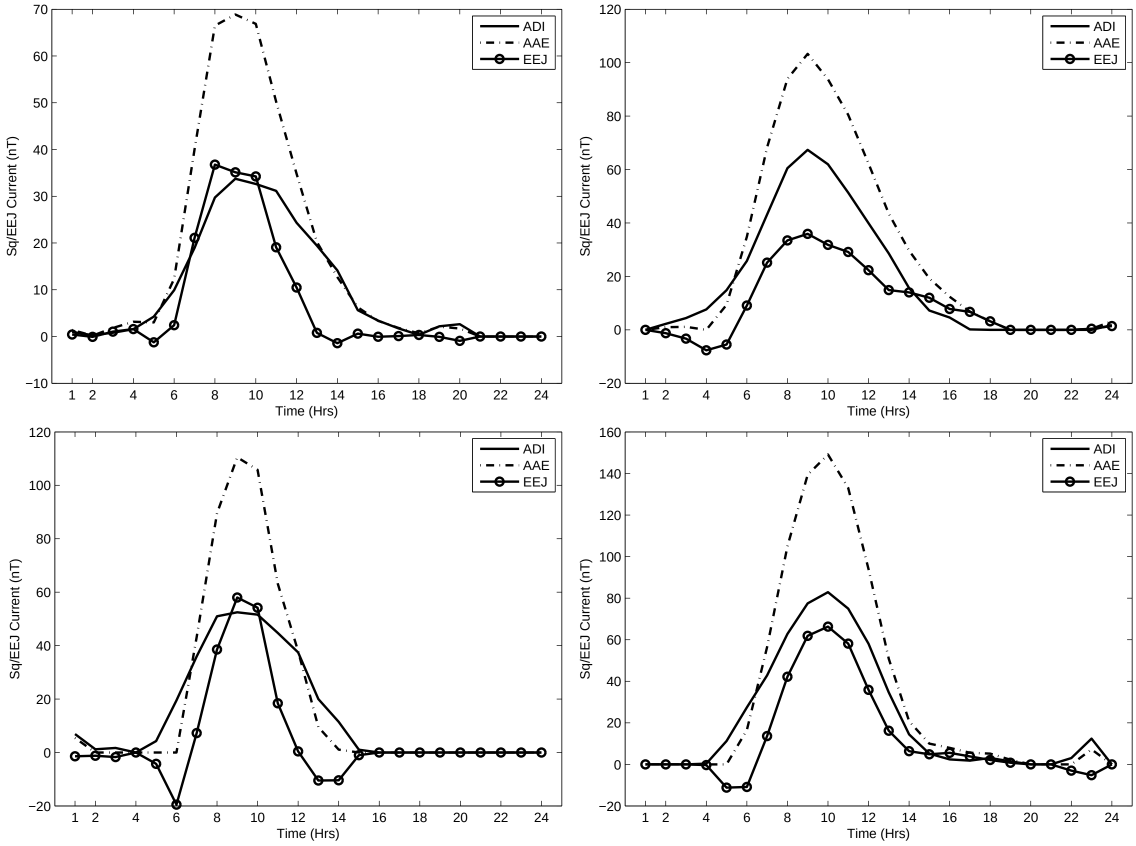

Figure 6.1: Selected plots representing diurnal variation of EEJ, on January 5 (top left), March 28 (top right), August 15 (bottom left), November 28 (bottom right)

Adigrat Sq current, AAE stands Addis Ababa Sq current. The days in the plots are selected as international quiet days from each month depending on the data availability. These plots were analyzed to study local time dependence of the Sq currents and the EEJ for different seasons of the year 2011. During the selected geomagnetic solar quiet days of the year the Sq currents and EEJ current sharply increase to their peak value from 9.00-13.00 LT, and gradually decrease and die out at around 18.00 LT which is in consistency with the dynamo action of the ionosphere which modifies the geomagnetic field. The enhancement of H component at this EEJ region is due to the intense Hall current of the dynamo action. As the plots indicate the increment in the H component at Addis Ababa location varies by a factor of 2-4 times larger compared to Adigrat. Again the Sq current at Addis Ababa station is also larger than that of the Sq at Adigrat at any time during day time.

The EEJ causes a large daily variation of the horizontal component of the earth's magnetic field intensity recorded by the magnetometers at Addis Ababa. This concentration of the ionospheric current near the magnetic equator arises from the inhibition of Hall current due to the horizontal configuration of earth's magnetic field horizontal stratification of the ionosphere.

6.2 Counter equatorial electrojet

Many mechanisms have been suggested for the generation of CEJ. The occurrence of CEJs as proposed by ([90] and references therein) are the local interaction of height varying winds, the gravity wave associated vertical winds [91] and appropriate phase combination of global scale tidal wind modes [92] are some of them. Recently, they investigate and attribute the occurrence of CEJ to the wind or additional current systems in the dynamo region. Vineeth et al [93] has shown an association of CEJ with the mesopause energetics in the form of a localized cooling in mesopause during the CEJ events. Recent studies had quantitatively established the relationships between the vertical daytime $E \times B$ drift velocity in the ionosphere in the F region and day time EEJ (e.g. [94, 95]). We have also revised that counter electrojet (CEJ) whose signature is seen under a negative depression in the horizontal magnetic field (H) at dip magnetic equatorial latitude during quiet times. The possible reversal of the east-west electric field during the above CEJ current events as explained by earlier works (e.g. Denardini [96] and references therein) are due to abnormal combination of global scale tidal wind modes such as an appropriate combination of tidal modes, like the (1, -2), (2, 2) and (2, 4) modes, would generate the reverse current at the magnetic equator which causes the negative perturbation in the ground magnetic field variations. Somayajulu et al [92], measured CEJ using coherent backscatter radar of type I waves is about -10nT, while for type II waves the measured intensity of CEJ reached a negative value of 35-40 nT and our result is not different from theirs. CEJ can occur at the morning and afternoon hours. Fig. 6.2 shows some CEJ observations at Addis Ababa station during the morning hours.

The morning counter electrojet (MCEJ) started at about 7:00 LT and lasted until around 9:10 LT, afternoon counter electrojet (ACEJ) started at about 15:00 and lasted until 17:00 LT. The CEJ is chosen based on the occurrence of negative EEJ current. Fig. 6.3 shows some of the observed CEJ in the afternoon between 15-18 hours local time on January 7, 8, 11 and August 16, 2011. In comparison afternoon CEJ occur more frequently on solstices than on equinoxes. On the contrary morning CEJ occurs more frequently on equinoxes than solstices.

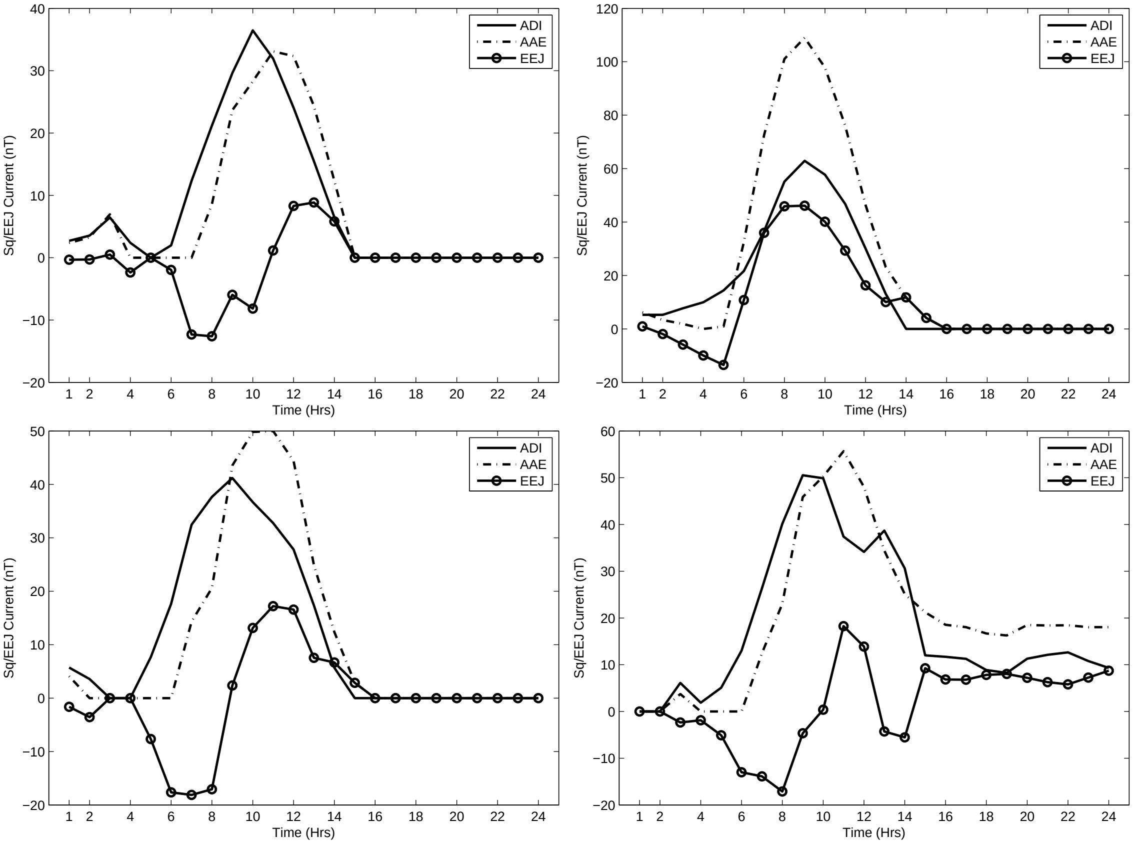

Figure 6.2: Examples of morning counter electrojets January 4 (top left), March 31 (top right), July 26 (bottom left),December 1 (bottom right) Addis Ababa respectively

6.3 The occurrence of pre-reversal enhancement during post sunset

A unique event was observed on 14/01/2011, 02/04/2011 and 02/12/2011 as shown in Fig. 6.4 although the geomagnetic indices are not shown here, reveals the selected dates are geomagnetically quiet days (available at wdc.kugi.kyto-u.ac.jp/wdc/sec3.html). Even though the EEJ current is not big enough there is significant Sq current observed

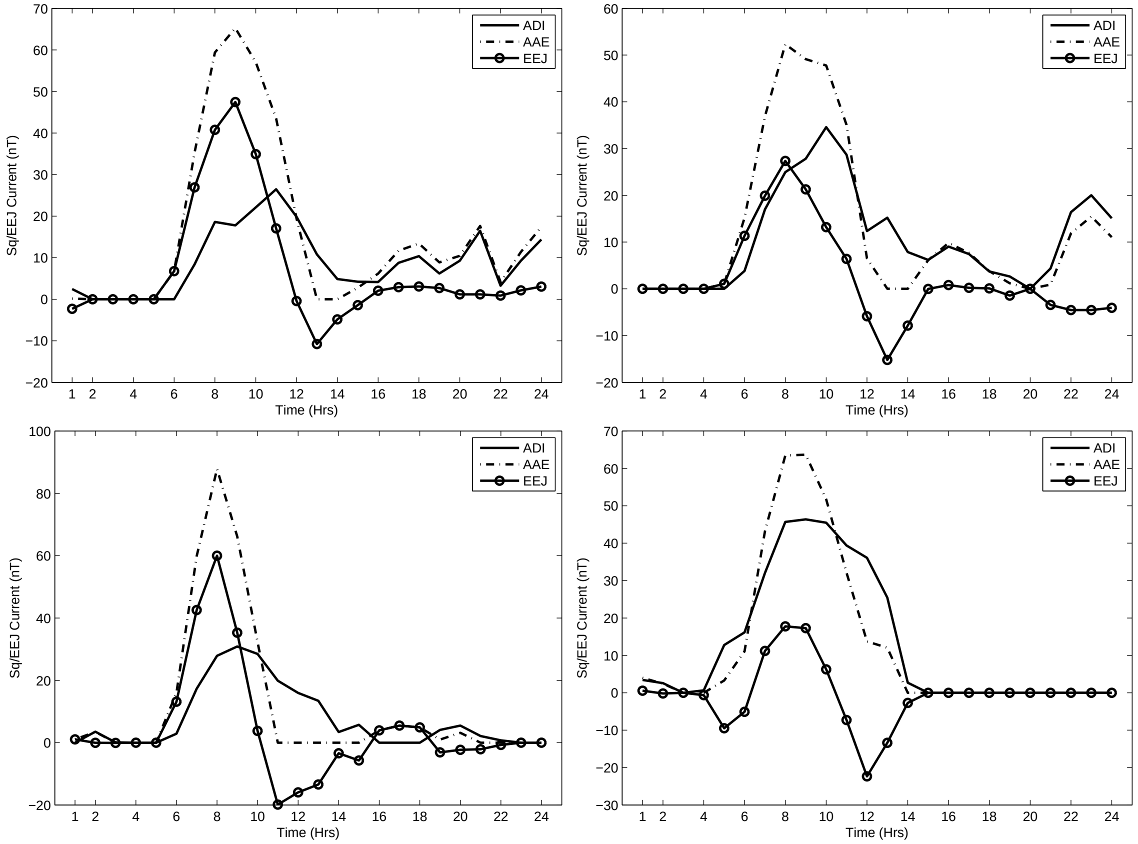

Figure 6.3: Examples of afternoon counter electrojets January (7(top left), 8 (top right), 10 (bottom left)), August 16 (bottom right), Addis Ababa respectively

during post sunset. This phenomena is called pre-reversal enhancement (PRE). According to previous results (e.g., [97, 98]) one can deduce that the magnitude and local time structure of the zonal wind as well as that of the longitudinal conductivity gradients across the terminator could control the prereversal enhancement (PRE). In general zonal E leads pre-reversal enhancement in the eastward electric field. Abdu et al [99] explained that the most observable of such process occurs at sunset when the rapid decay of field line integrated conductivity, into the night side, gives rise to an enhanced zonal eastward electric field arising from the F layer dynamo driven by

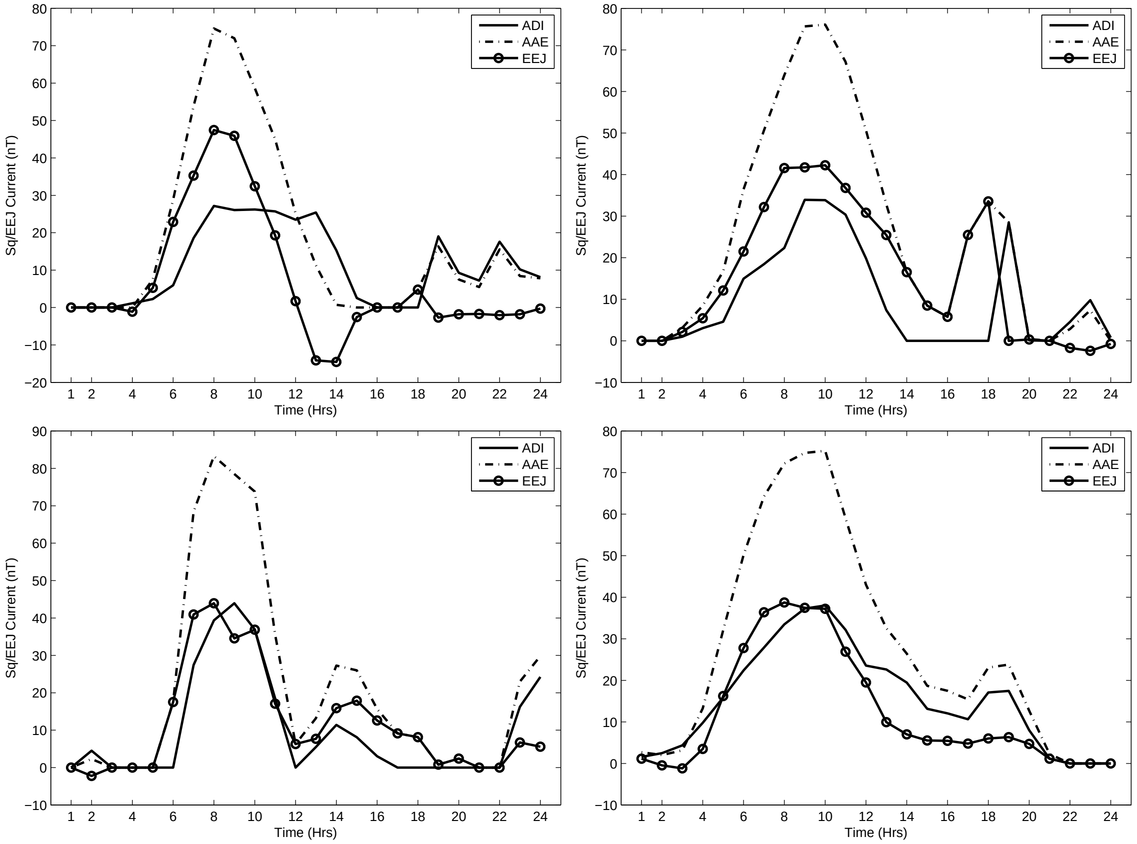

Figure 6.4: Pre-reversal enhancement during post sun set on days January 14 (top left), 31 top right), April 2 (bottom left), December 2 (bottom right), Addis Ababa respectively

the thermospheric wind movement eastward at these hours. According to the interpretation of Farely et al [54], the U wind tries to drive the field to a value of $-U \times B$ but prevented from doing so to some degree by E region based on the relative magnitude of the integrated E and F regions Pedersen conductivities. The pre-reversal enhancement is basically responsible for the formation of the evening plasma fountain and the associated large uplift of the F layer, which leads to instability development responsible for the formation of spread F events.

6.4 Seasonal variation of EEJ

To study the seasonal variability of the H component, Lloyd's seasons [70, 69], in which the whole year is allotted in to three seasons; December or D-season (December, November, January, February), equinox or E-season (March, April, September, October); June Solstice or J-season (May, June, July, August) are used. Measured results from ground based magnetometers show that the EEJ has significantly increased during E-seasons than D and J-seasons. During equinox the sun shines directly on

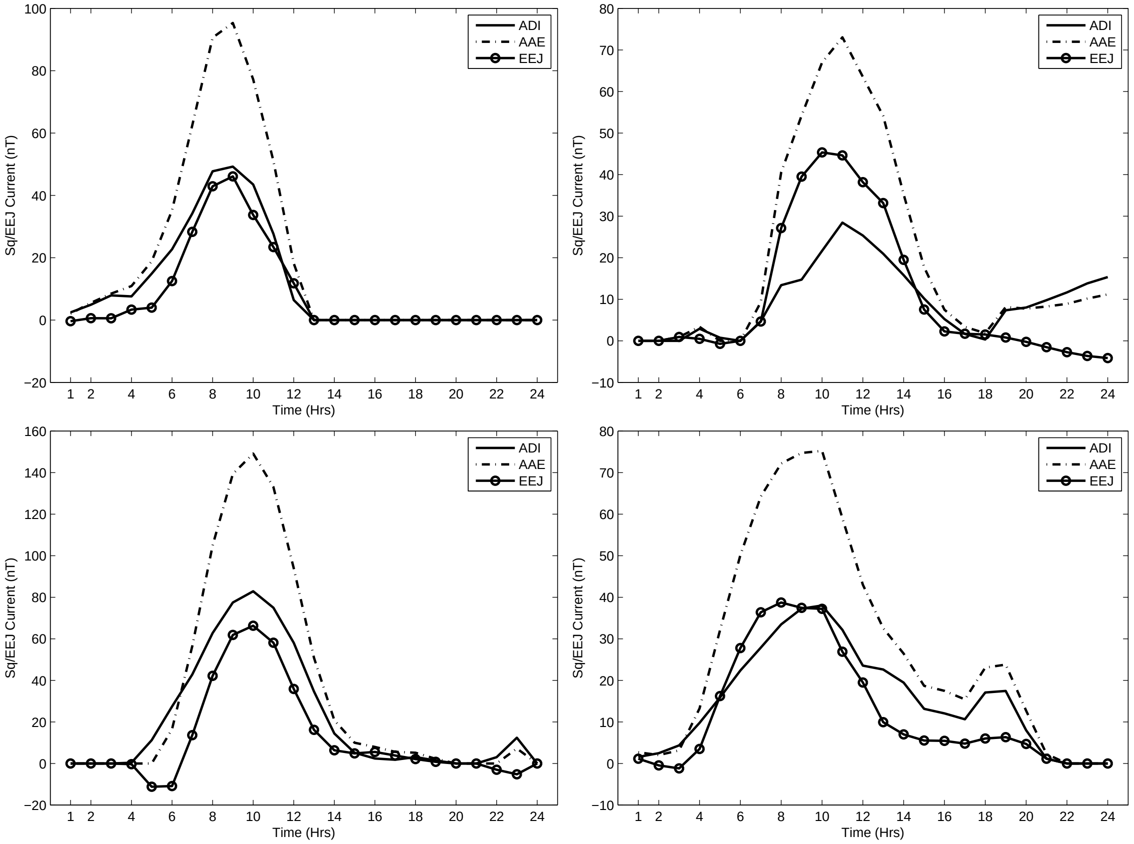

Figure 6.5: Selected plots from D season on January 19 (top left), February 12 (top right), November 28 (bottom left) and December 2(bottom right)

the equator and the length of day and night is nearly equal and because of maximum photo-ionization, maximum Sq current in the equatorial ionosphere is expected to fluctuate the magnetic field of the earth.

It is important to note that Earth does not move at a constant speed in its elliptical orbit. Therefore the seasons are not of equal length: the times taken for the sun to move from the vernal equinox to the summer solstice, to the autumnal equinox, to the winter solstice, and back to the vernal equinox are roughly 92.8, 93.6, 89.8 and 89.0 days respectively. The consolation in the northern hemisphere is that spring and summer last longer than autumn and winter (when the December solstice occurs). The relative position of the earth's axis to the sun changes during the cycle of seasons. This phenomenon is the reason why the suns height above the horizon changes throughout the year. It is also responsible for the seasons through controlling the intensity and duration of sunlight received at various locations around the planet. So during solstice the sun is not overhead at the equator that means the light intensity that pass through the ionosphere above the equator is small compared to the equinox which leads to small currents in the ionosphere which in turn produces small fluctuation on the magnetic field of the earth. For example Fig. 6.5 are some of D season EEJ currents for some selected days. During D-season the sun is in the southern hemisphere so the Sq current at the northern hemisphere is very small and still Sq current at the magnetic equator is not as such big enough. So the EEJ at this time is less than EEJ measured during equinox. When the sun is overhead over the equator, the equinox, EEJ currents observed at this time over dip magnetic equator over Addis Ababa is larger compared to that of the EEJ currents during the D-season and J- season. This is because Adigrat is on the northern hemisphere so it is expected that the Sq current at Adigrat is large compared to the other two seasons because

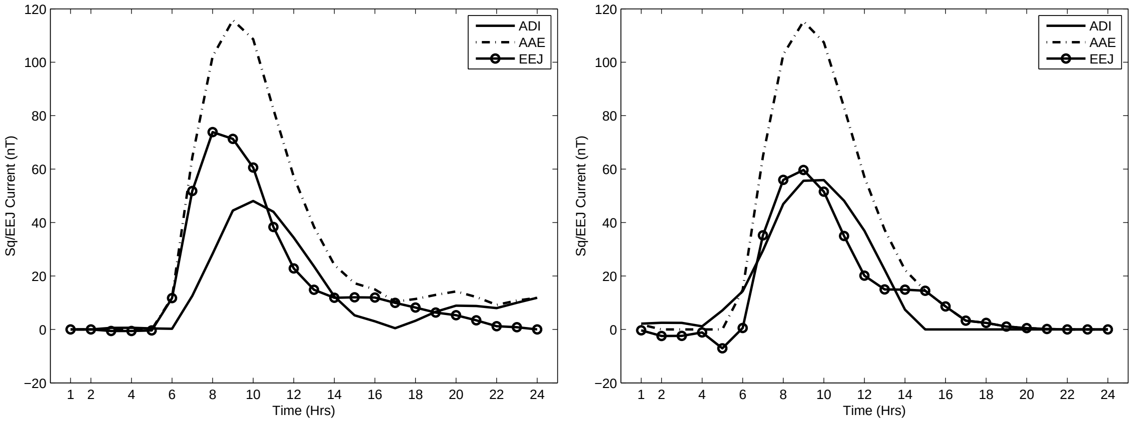

Figure 6.6: Selected plots from E season on April 21 (left), March 27 (right)

the delta Sq which is the EEJ current is small. Therefore it can be easily identified that the EEJ is directly related to the Sq current. That is the Sq current is relevant with the solar zenith angle, because the solar zenith angle decides the conductivity in the ionosphere by controlling the distribution of the electrons.

6.5 Longitudinal variation of EEJ

Understanding EEJ variation from longitude to longitude along latitude circle is not easy from ground based magnetometers since most of the earth's surface is covered by water. Here we used an empirical EEJ model version 2 EEJM2 which is available and accessible at http://www.geomag.us/models/EEJ.html., to show how the EEJ current is changing with longitude and local time. As shown in the plots the EEJ current value is not the same every where along the circle. Thus the EEJ has its maxima at 4 longitudinal sectors. The model also estimates maximum EEJ on E-season compared to the D-season and J-season.

We have computed the diurnal variation of the magnetic perturbations along the

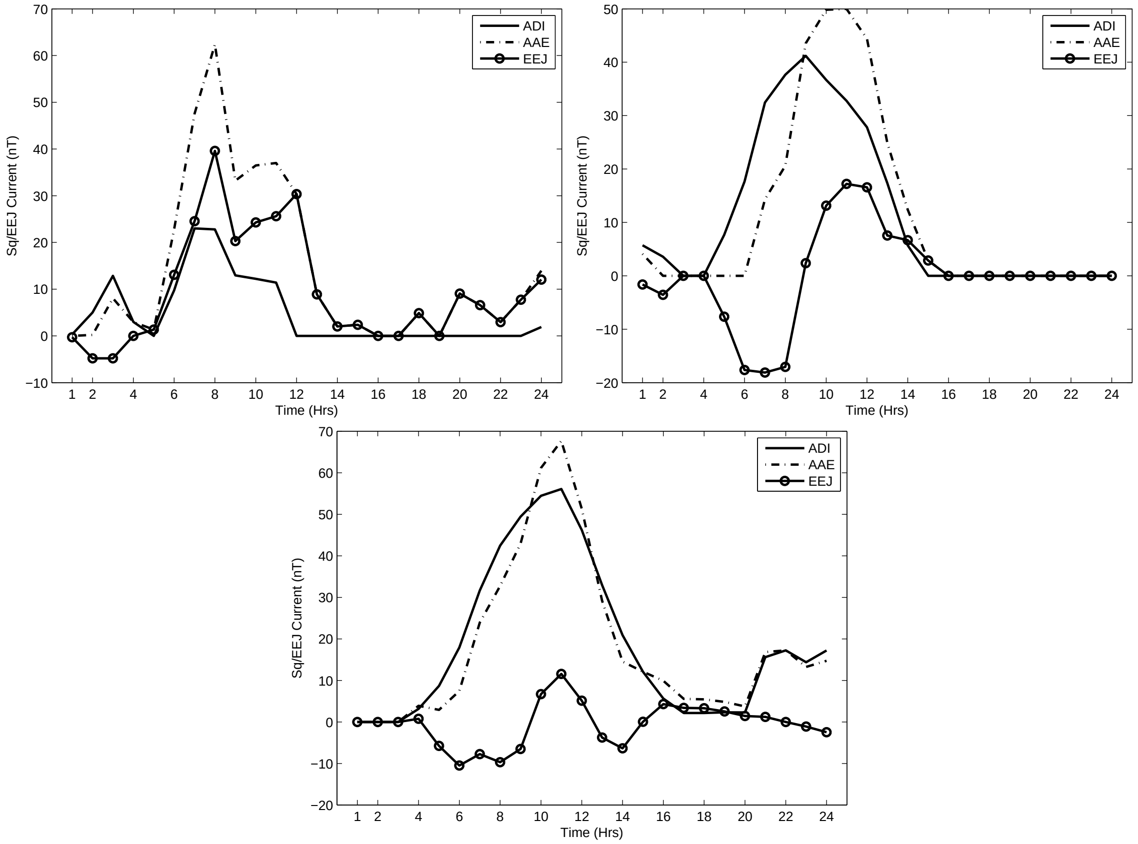

Figure 6.7: Selected plots from J season on may 2 (top left), July 26 (top right), August 11 (bottom).

dip equator in different seasons. Figs. 6.8-6.10 represent the simulated mean diurnal variation of the H component for each month. The amplitude of the H component depends on season, being highest in E season. The plots show that a net change in the amplitude and the shape shows maximum every 90^0 longitude separation. The maximum is observed at four longitude sectors. The EEJ current values on D seasons is relatively larger compared to the J-seasons. The minimum EEJ current is obtained at J-season especially on months June and July, while its peak value is on E-season especially during September and October. As shown in Fig. 6.9, the magnitude of EEJ peak values on E seasons is about 0.1 nT while peak EEJ vales are 0.08 nT for

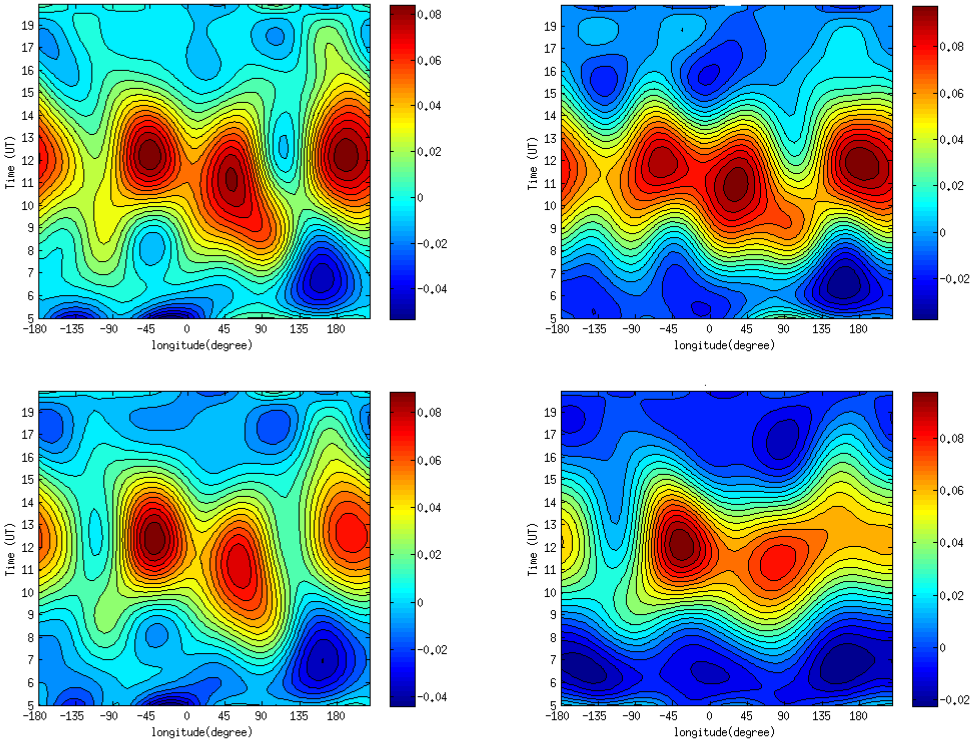

Figure 6.8: Monthly mean D seasons EEJ from model EEJM2 for months December (top left), November (top right), January (bottom left) and February (bottom right).

the solstices. The longitude dependence of EEJ current can be explained interms of the observed peak currents. As shown un Figs. 6.8-6.10, EEJ along longitude Shows oscillatory behavior. The value of EEJ oscillates between trough at 0^0 meridian and crust at 45^0 longitude and repeats the cycle every 90^0 along the circle.

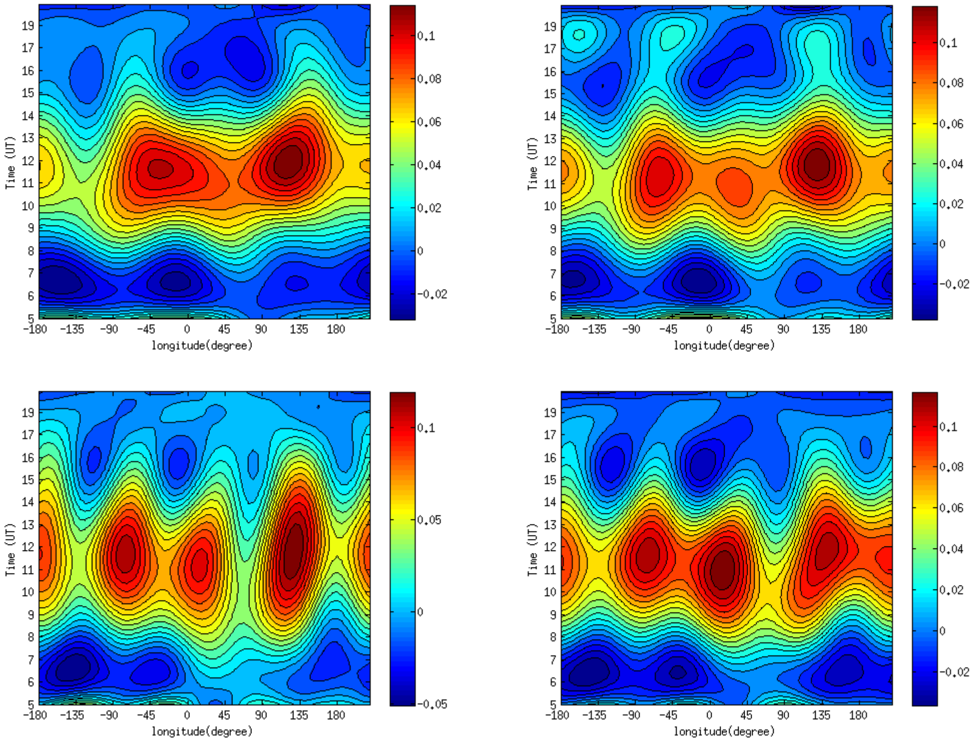

Figure 6.9: Monthly mean E seasons EEJ from model EEJM2 for months March (top left), April (top right), September (bottom left) and October (bottom right).

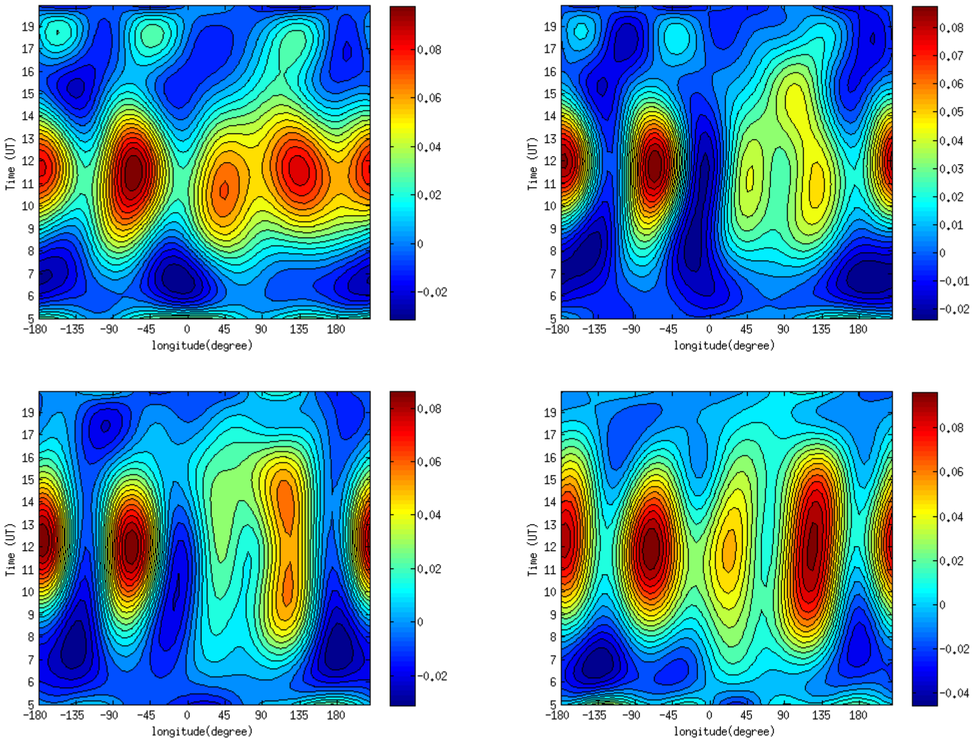

Figure 6.10: Monthly mean J seasons EEJ from model EEJM2 for months March (top left), April (top right), September (bottom left) and October (bottom right).

Chapter 7

The geomagnetic storms of January 22-25, 2012

Solar storm is a natural phenomenon which occurs as a result of the natural rises and falls in the sun's magnetic activity over an 11 years cycle. In fact geomagnetic storms can occur at any time when the sun releases magnetic energy, bursts of charged particles called CMEs head towards earth and interfere with the magnetic field of the earth. The earth's ionosphere responds dramatically to geomagnetic storms coupling the neutral thermosphere with the overlying magnetosphere. During the sever geomagnetic storms penetrating electric fields and plasma redistribution combine to produce enhancements and reduction of ionospheric TEC, steep localize density gradients and storm time space weather effects. Ionospheric measurements often indicate that during magnetically disturbed conditions the law latitude electric fields and currents large departures from their quiet time averages ([100] and references therein). The direct penetration of the high latitude electric field to the lower latitude and the ionospheric disturbance dynamo are the two major contributors to the ionospheric

electric field at low latitude during geomagnetic disturbances [9, 99]. Basically geomagnetic disturbances are caused either when the IMF is directed south ward or when the magnetosphere of the earth is stroked by solar wind. Interplanetary electric fields, caused by the convection motion of the solar wind across the interplanetary magnetic field as inferred from $\vec{E} = \vec{V} \times \vec{B}$ ([101] and references therein)., may appear almost immediately in the Earth's magnetosphere and ionosphere after these electric fields are convicted from the solar wind to the magnetosphere. This phenomenon is commonly termed as the prompt penetration of the interplanetary electric field (IEF) in to the magnetosphere/ionosphere system, or simply electric field penetration.
In this topic we tried to analyze the observed events on January starting from 22-25/2012. NASA's SOHO detected a strong M9 class solar flare and associated CME on Jan 22,2012 at about 4 UT. The CME is headed in the Earth's direction and was expected to cause a moderate geomagnetic storm. Following a Coronal Mass Ejection (CME) on 22 January 2012, we have observed the pre, during and the post events from the ground and space based instruments.

Geomagnetic activity is caused by transfer of energy and momentum from solar wind to the magnetosphere that occurs in response to the southward interplanetary magnetic field. The geomagnetic storms that have occurred between January 22-25, 2012 are characterized using observational data analysis such as the variation of the $SYM-H$, AE, V_p, IMF B_z, proton temperature and density, flow pressure, and proton flux events. Previous studies have used these parameters in part or in whole to characterize the nature of geomagnetic storms. For instance, large number of studies have associated geomagnetic storms with extreme increase in the solar wind velocity and/or southward interplanetary magnetic field (IMF) due to coronal mass ejection

(CME) and their associated interplanetary shocks.

Fig. 7.1 shows $SYM - H$ over a period of 21 days that includes few days before and after the occurrence of the storms. It is a high resolution since it has a temporal resolution of a minute and can be regarded as a high resolution Dst index. As shown in Fig. 7.1, the $SYM - H$ value on January 22 shows a sudden increase to more than 50 nT at the sudden storm commencement (SSC) and then sharp decrease to a value of -100 nT after which a recovering starts and a second SSC on January 24 followed by another shock on January 25. The compression exerted on the sunward side of the earth's magnetosphere by strong plasma cloud ejected from the sun is responsible to develop sudden storm commencement (SSC) and main phase of the storms. These SSCs before the main storms on January 22 and 25 are evidences for the occurrence of Coronal Mass Ejection (CME) which causes compression of the magnetosphere leading to fluctuation of the Earth's magnetic field. It is known that geomagnetic storms can also be driven by Corotating interaction regions (CIRs). However, the storm that have happened on January 22 and 25, 2012 are likely to be due to the CMEs because the recovery period is short unlike that of CIR driven geomagnetic storms. The $SYM - H$ value shows a sharp positive increase up to 50 nT which is a SSC before the main storm phase indicating a fast forward shock is formed. When geomagnetic storm occurs the $Dst < 0$ because there exists enough reconnection to sufficiently energize the ring current to overcome the preexisting huge magnetopause current. A fall in the $SYM - H$ index is typically accompanied by the plasma sheet moving inward of geosynchronous orbit, with the highest increase in the ion and electron densities occurring during the main phase of the storm at, or close to, minimum $SYM - H$ index value.

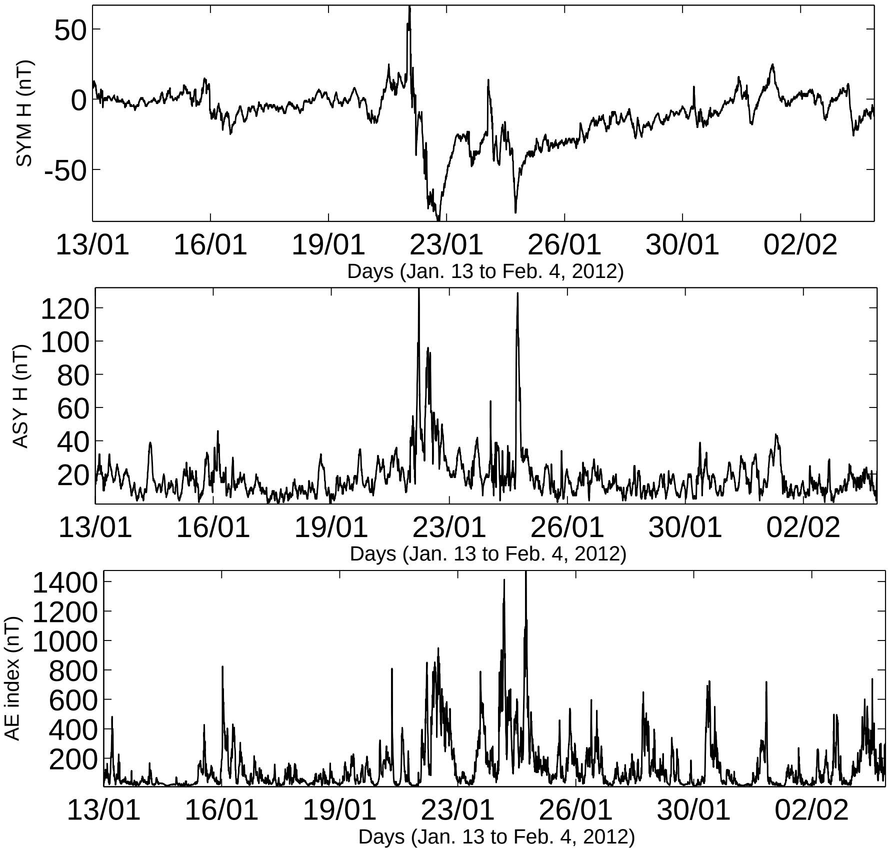

Figure 7.1: $SYM - H$, ASY and AE index time series during January 13- February 4, 2012.

Another geomagnetic disturbance index is the $ASY - H$ index which is a measure of the difference between the maximum and minimum $SYM - H$ values. Fig. 7.1, middle panel, shows that on days 22 and 25 the difference between maximum and minimum $SYM - H$ values is exceptionally large compared to the other undisturbed days.

Fig. 7.1, bottom panel, shows enhancement in AE index on days 23 and 25. This index is particularly suitable to characterize the polar region. The high values on these dates implies ionospheric perturbation. This is an indication of significant amount of energy was injected at high latitude during the storm period in contrast to the geomagnetically quiet days whose AE index value is significantly small.

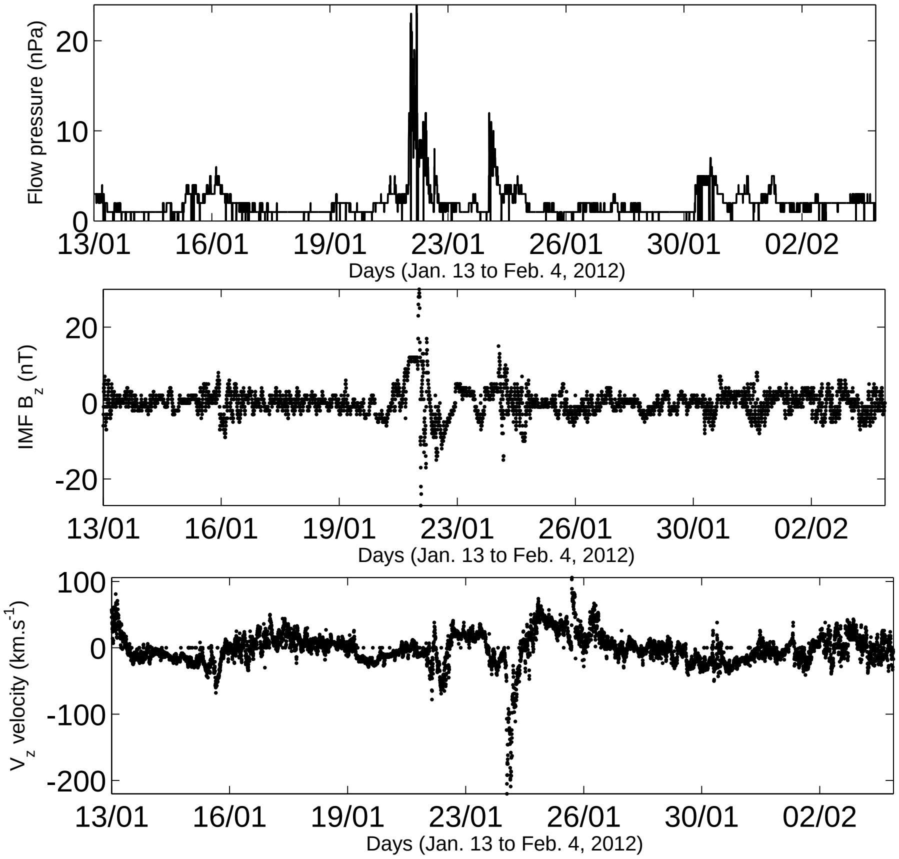

Figure 7.2: The variation of solar wind dynamic pressure in nPa (top), IMF B_z (middle) and solar wind velocity during 21 days encompassing the storm events.

The sudden jump of the solar wind dynamic pressure in Fig. 7.2, top panel, and the IMF B_z in Fig. 7.2, middle panel, corresponding to the bow shock called magnetic storm sudden commencement clearly are other indicators that the storms are driven by CMEs. As indicated in the Fig. 7.2 (top panel) a sharp enhancement of flow pressure on January 23 followed by falling into its normal value on January 24 and again sharp increment on January 25 is an evidence of two CMEs driven storms. Fig. 7.2 (middle) represents IMF B_z during the 21 days period encompassing the storm time and depicts the behavior of the IMF B_z before, during and after the occurrence of geomagnetic storms. The IMF B_z value during the quiet days was almost zero but sharply and momentarily increases signalling the onset of the storm after which it falls into its negative value until it reaches the end of the main phase of the storm. The reasons for this events are, when the interplanetary magnetic field B_z and geomagnetic field lines are oriented opposite or anti-parallel to each other a bow shock occurs and then, they can merge or reconnect resulting in the transfer of energy, mass and momentum from the solar wind flow to magnetosphere.

The IMF B_z is not highly variable except at the fast forward shock which suggests that the geomagnetic storm is CME-driven. This is in agreement with others indices so far discussed. In the case of southward B_z, more energy deposition into the higher ionospheric latitudes is observed due to the possible magnetic reconnection processes. The dawn-to- dusk disturbance electric field in the equatorial ionosphere is associated with southward turning of the interplanetary magnetic field component, B_z ([102] and references therein). The southward interplanetary magnetic field and the continuous increase of AE activity that recovers its original shape after $IMFB_z$ turns north imply the pre storm and post storm conditions have the same phenomena.

Lindsay et al [103] and many other investigators have demonstrated that geomagnetic storms are accompanied by high solar wind velocities, and enhanced solar wind dynamic pressure and CME. The southward solar wind velocity in Fig. 7.2, bottom panel, reaches -100 $\frac{m}{s}$ on January 22, 2012 and recovered on the next day followed by another maximum speed of about -200 $\frac{m}{s}$ on January 24 accompanied by recovery on January 25, 2012. These features in the solar wind velocity confirm previous indicators that two CMEs are responsible for the geomagnetic storms.

A solar proton event (SPE) occurs when protons emitted by the sun become accelerated to very high energies during a solar flare accompanied by a coronal mass ejection or in interplanetary space by the shocks associated with coronal mass ejections. Protons are finally guided by the interplanetary magnetic field lines. The energy of $E > 10\ MeV$, proton flux is nearly $5000/cm^2.s.sr$ following the storm on January 22 and and very much negligible after the one on January 25, 2012. Similarly, for $E > 30\ MeV$ energy range, proton is more than $200/cm^2.s.sr$ for the first SSC on day 22 and over $50 - 70/cm^2.s.sr$ after January 25, 2012 while the proton flux with energy $E > 60MeV$, is more than $20/cm^2.s.sr$ for the second SSC. These high energy proton flux can produce abnormal ionization in the lower ionosphere that was visible in the TEC enhancement as shown in next sections.

The huge enhancement of the proton density in Fig. 7.3 on January 22, 2012 also is an indicator for the deposition of solar materials as a result of CME that has happened on that day. The ion density enhancement at time of minimum Dst appears to be directly related to the magnitude of the Dst with larger densities during the larger storm due to CMCs [104]. Comparison of proton density during the 21 days time series show about six orders magnitude higher during sudden commencement of the storm as opposed to the remaining phases of the storms. Fig. 7.3 (bottom panel) shows maximum proton temperature on both January 22 and 25 which is consistent with the proton flux and energy category in contrast to the temperature during the rest of observation periods.

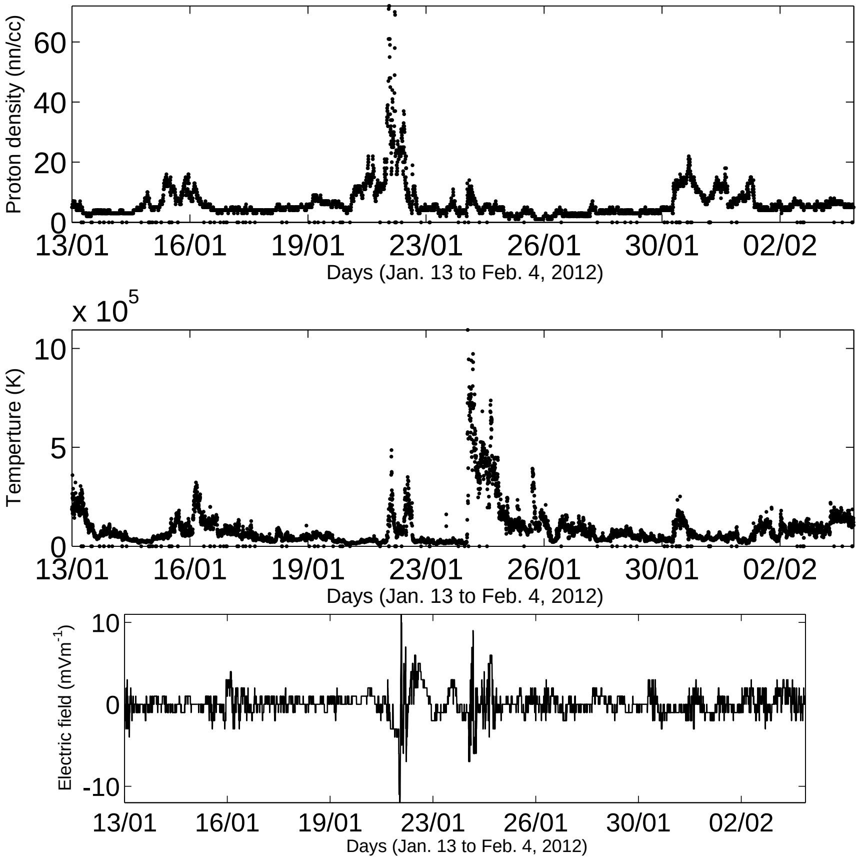

Figure 7.3: Proton density in nn/CC, temperature and derived electric field

Fig. 7.3, bottom panel, shows the east west electric field estimated from $\vec{V} \times \vec{B}$. It is clearly evident that there is prompt penetration electric field during the disturbed days. Basically the interplanetary southward magnetic field's component (B_z) introduces a dawn-to-dusk interplanetary electric field (IEF) at the magnetopause given by $E_y = -\vec{V_{sw}} \times \vec{B_z}$ so that during the time interval between connection and reconnection of geomagnetic field lines are open and IEF can penetrate to the polar regions of the ionosphere causing sudden changes in cross cap. This electric field can be instantaneously mapped to the lower latitudes to change the lower ionosphere dynamics.

7.0.1 Ionospheric response to geomagnetic storm: Spatial-temporal TEC variations

The ionosphere response to geomagnetic storm is manifested through change in TEC. However, first it is important to identify relationship between storm parameters such as $IMFBz$ and ionospheric parameter viz-vis TEC. We have used wavelet coherence analysis if the two geophysical parameters are appropriate to represent impulse-response relationship. Both $IMFBz$ and TEC are re-sampled at an interval of an hour for crosswavelet analysis. Moreover, since $IMFBz$ exhibits high frequency variability, the data is smoothed using Butherworth filter with temporal window of 12 hours. As wavelet requires two time series, a single time series representing TEC is required. We used the leading principal component (PC1) of TEC from empirical orthogonal analysis. Fig. 7.4 shows PC1 of TEC (top), smoothed $IMFBz$ (middle), wavelet power of $IMFBz$ (bottom-left) and coherence spectra (bottom-right).

The leading TEC PC accounts for over 30% of TEC variance and the corresponding EOF has a dipole pattern with one pole over west and the other over eastern hemispheres. The second PC accounts for about 20% of the variance but has no coherence with the smoothed $IMFBz$. Therefore, PC1, which has high wavelet power with a period of one day (not shown), is chosen to represent ionospheric response to the geomagnetic storm. $IMFBz$ has significant and high wavelet power with a periodicity from half day to three days during a period from day 6 (January 20, 2012) to day 18 (February 1, 2012). Though crosswavelet of the two time series (not shown) exhibits high power with a periodicity of a day, their joint variability at this frequency is incoherent as reflected by significant coherence with a periodicity centered on two days (Fig. 7.4, bottom-right). $IMFBz$ leads PC1 of TEC by approximately 90^o as shown by phase arrows which is equivalent to 12 hours for a period of 2 days. While this is a dominant mode of coherence between TEC, through its leading PC, and $IMFBz$, the response of the ionosphere to geomagnetic storm at different locations is undoubtedly diverse.

Once the general picture is attained, we can now proceed to investigate unusual change in the total electron content (TEC), i.e., both increase or decrease, in response to geomagnetic storms. The change can be used as a complimentary evidence to indicate the occurrence of geomagnetic storm as well as to study the spatial differences in the ionospheric response. Fig. 7.5, top panel, is the relative percentage change in TEC over 21 days of observation centered on days when storms have occurred at Addis Ababa location, which is arbitrarily chosen. It is clearly indicated in Fig. 7.5 that TEC increased from its normal value prior to January 20 during the following days with sharp gradient on January 22 when the first SSC was observed in conjunction with CME.

This intense TEC gradient between days before the storm and during the storms is better apparent in the lower panel of Fig. 7.5 between 5-16 UTC which shows TEC variation for six days at Addis Ababa. A jump from about 35 TECU on January 20 to 60 TECU on January 25 is observed at TEC peak hours of 9:30-10:30 UTC. Fig. 7.6 shows global map of mean daily differential TEC for the 6 days shown earlier. The relative percentage change on the first two days (Fig. 7.6, panels a and b) varies between -20 to 20% spatially. The sharp gradient shown earlier at Addis Ababa is now evident from an increase in relative TEC change exceeding 60% on January 22 relative to the first 8 quite days over regions north of $10^{o}N$. TEC is depleted the next day over polar regions to values lower than the quiet days. However, TEC increased

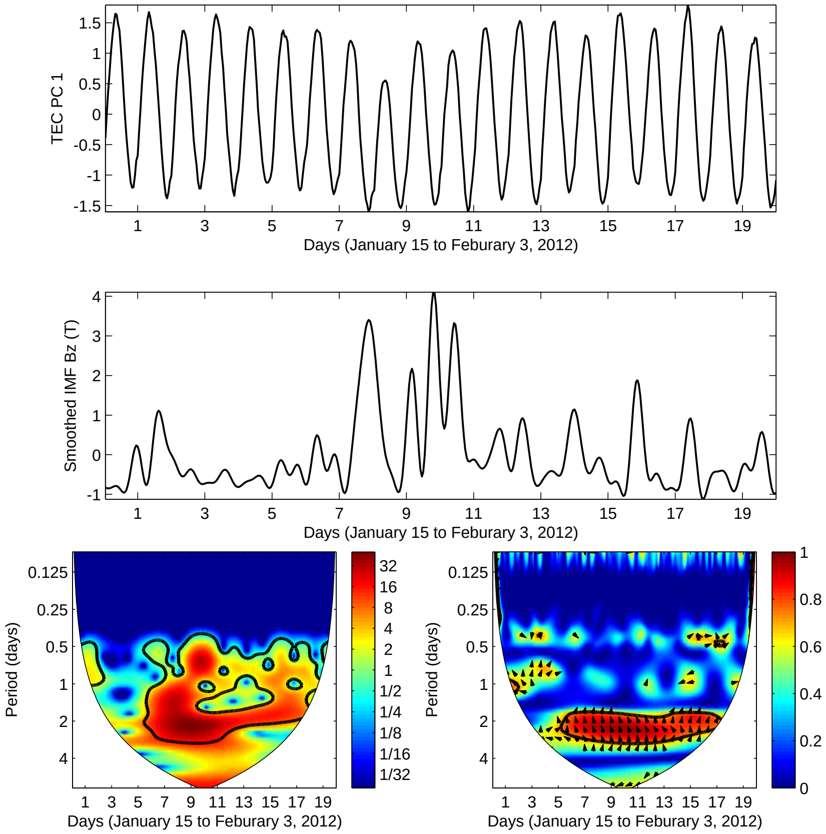

Figure 7.4: The first principal component of TEC (top), smoothed $IMFBz$ (middle), wavelet power of $IMFBz$ (bottom-left) and wavelet coherence power (bottom-right).

again over the polar region on January 24 and 25 while regions equatorward of $30^o N$ show some enhancement in the order of 30% at some isolated places in contrast to situation on January 22 when the enhancement was extensive.

Moreover, on January 23 (Fig. 7.6, panel (d))the northern polar region plasma is shifted towards the equatorial region. Again on January 24 (see Fig. 7.6, panel (e)), as characterized by the geomagnetic indices in Section 7, another storm occurred leading to maximum TEC on the same day around the northern polar region and then started spreading equatorward on the next day (Fig. 7.6, panel (f)). After the main storm the equatorward spread of TEC is a clear indicator of prompt penetration

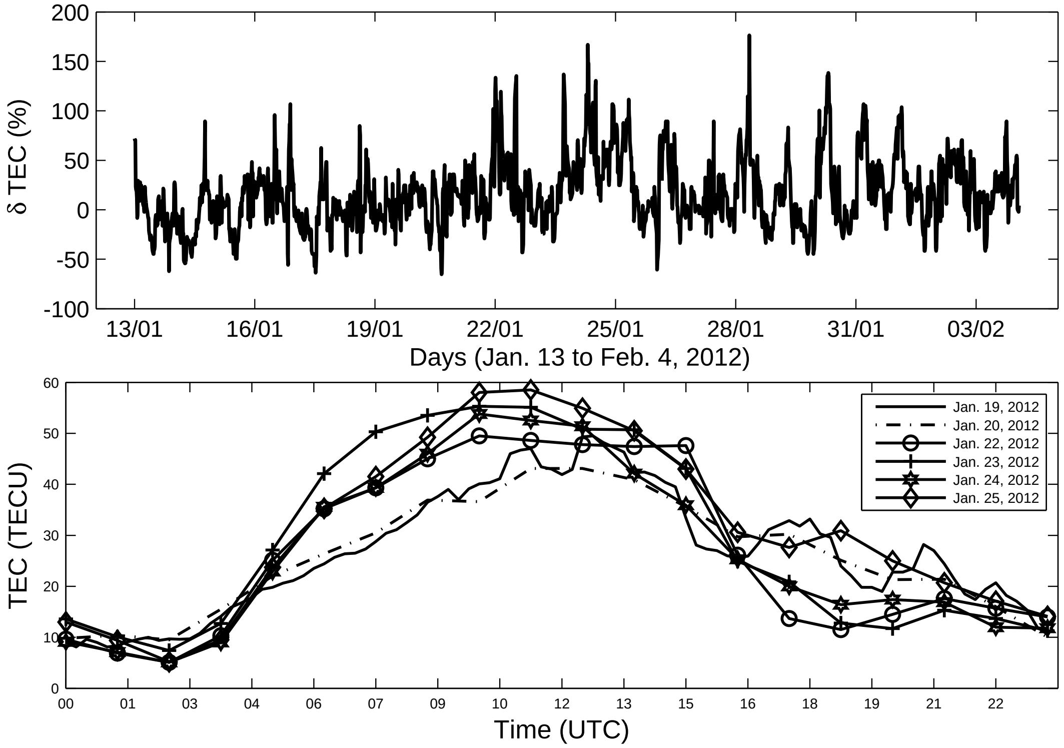

Figure 7.5: Relative change in GPS TEC values in percentage(top) and GPS-TEC extracted from global TEC at location close to Addis Ababa, Ethiopia. The median TEC is estimated for TEC observation from January 13-20, 2012 as this was a geomagnetically quite days from Dst and others indices discussed in Section 7.

of electric field towards the low latitude regions of the ionosphere as clearly exhibited on January 23-25, 2012. Moreover,during the disturbed days especially on January 23, the southern hemisphere TEC is highly depleted while TEC is accumulated over the northern hemisphere as marked by the white solid lines. The white solid lines delineate boundary between TEC enhancement and depletion. This could be an indication of transport of plasma towards the equatorward from southern hemisphere in line with the fact that in summer, the storm induced circulation augments the normal seasonal circulation from summer to winter hemisphere where the composition disturbance can easily be transported to mid- and low-latitudes. In contrast, in the winter, the storm induced circulation competes with the seasonal flow thereby constraining the composition to high latitudes as distinctly shown in Fig. 7.7c-f. To gain further insight into the changes in TEC following storm onset, we have looked at snap shot of TEC changes over 6 days at 10 and 11 UTC hrs which are time after solar noon over East Africa longitude sector. These times are chosen to coincide with the time of the peak TEC over Addis Ababa, arbitarily chosen in the earlier analysis to demonstrate the impact of the storm at low latitude, in particular at geomagenetic equator, for the sake of comparison. The two panels (a-b) in Fig. 7.7 represent the delta TEC for the quiet days at 10 hr while panels (c-f) are for geomagnetically perturbed days at 10 hr. During quiet days the delta TEC value at 10 UTC hr shows

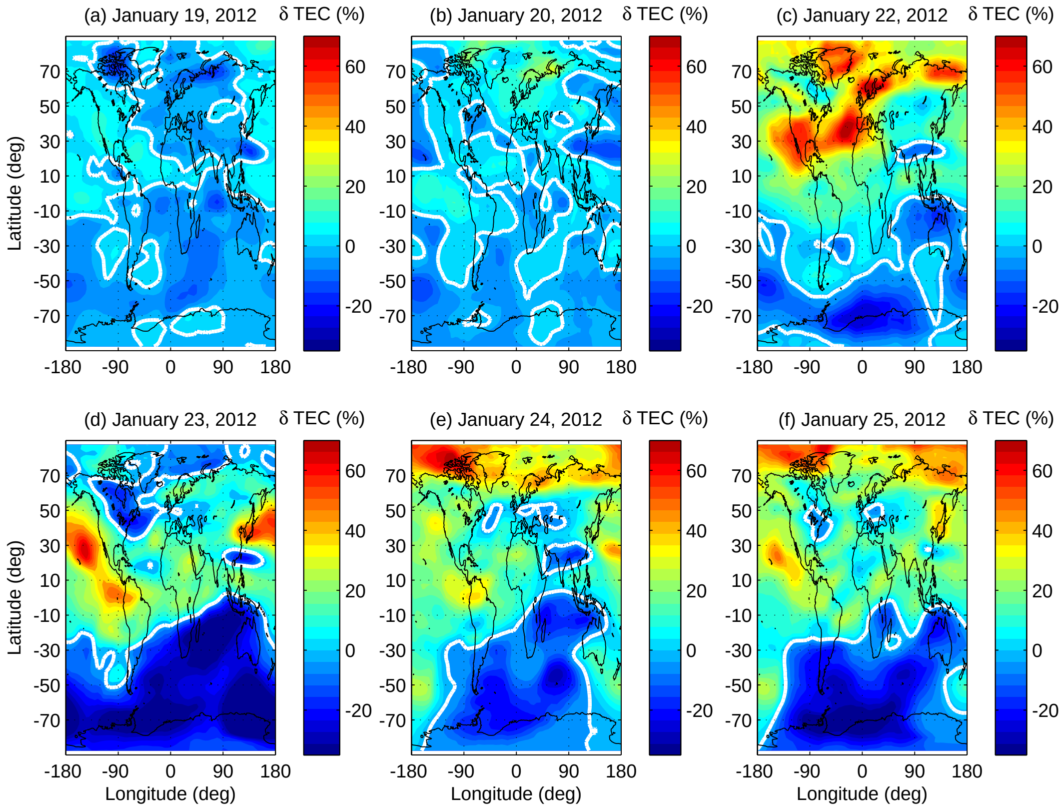

Figure 7.6: GPS-delta TEC daily mean in TECU

a good coverage from pole to pole although its peak value is over the north half of sunward side. However,during the disturbed days, the southern hemisphere TEC at 10 UTC is also depleted appreciably while TEC is enhanced over the northern hemisphere owing to the same mechanisms in which storm induced and seasonal circulations are involved. In general as compared to the quiet geomagnetic conditions the day time ionization is enhanced at high latitude during the disturbed days and subsequently moves to the low latitudes. This feature is also reflected at 11 UTC hours shown in Fig. 7.8. Another important feature marked in Figs. 7.7-7.8 is the enhancement of TEC northward of 70^oN across all longitudes regardless of difference in solar time on January 22 and 25 suggesting the geomagnetic storm diminishes the diurnal difference. In otherwords, ionospheric storms associated disturbances are rather worldwide and occur simultaneously in the day and night part of the globe.

TEC variation is mainly driven by solar forcing with peak at solar noon and minimum shortly after midnight. MTM-SVD spectral analysis reveals that diurnal TEC variations and its higher harmonics account for most of the variability including the storm period. For instance, the fractional local diurnal variance in Fig. 7.9 shows that much of the variability near the geomagnetic equator, upto a maximum of 83%, is accounted by the daily solar cycle. The localization of maximum diurnal TEC variance region in the subtropics is also consistent with the strong seasonality of solar forcing. Global TEC is more variable over wider regions in southern hemisphere than northern hemisphere ionosphere due to overhead sun during winter solstice day leading to maximum photo ionization which in turn creates sharp diurnal TEC gradient. The diurnal TEC variance shows also western and eastern interhemispheric asymmetry. The diurnal TEC variance exceeding 58% over eastern hemispheric extends as far

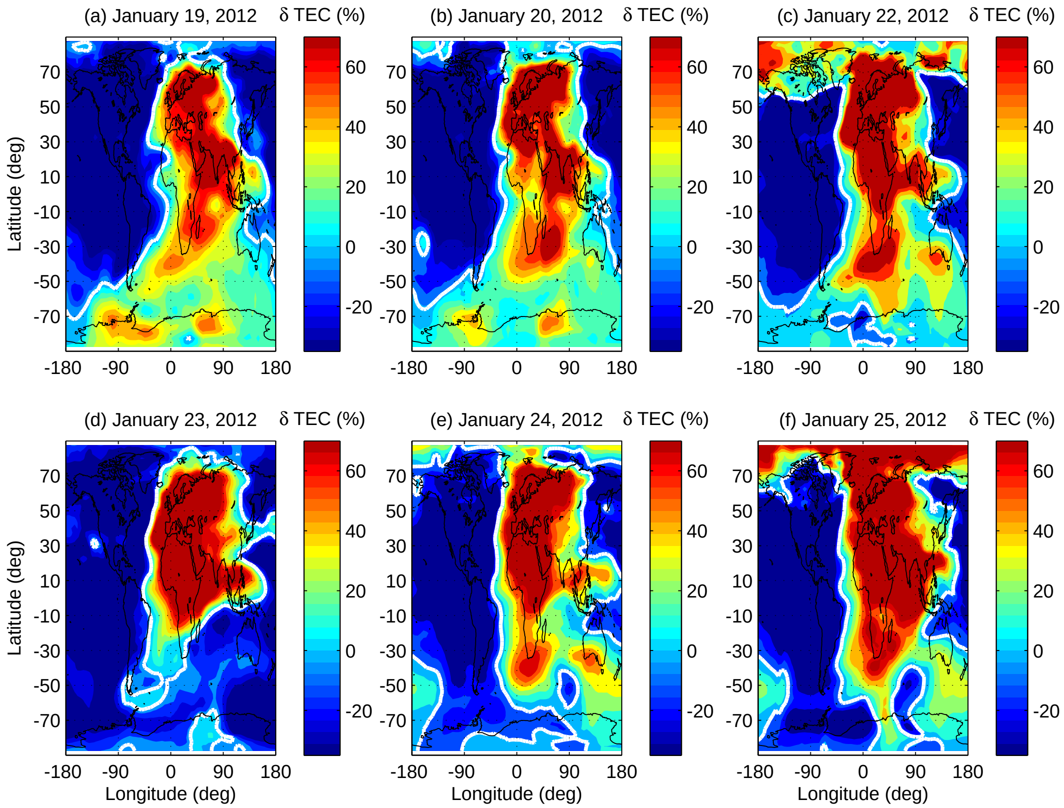

Figure 7.7: GPS-delta TEC snap shot over 6 days at 10 UTC hr.

north as 70^0 N while this value hardly extends upto 50^o N in the western hemisphere. In contrast, the 58% contour line extends as far as 80^oS in the western hemisphere whereas this contour hardly reaches 70^o S in the eastern hemisphere.

There is a peak TEC semidiurnal variance of upto 30% extending along 70^oS latitude belt and 50-70^oN over North America and Atlantic Ocean Fig. 7.10. The TEC semidiurnal variance is localized in such a way that interhemispheric asymmtry observed in the diurnal TEC is maintained but with opposite sign to the diurnal TEC variance. However, the hemispheric asymmetries persist even when the the two variances are combined albeit the asymmetry is weak. The persistence in the interhemispheric asymmetries suggests that other wave components such as non-migrating

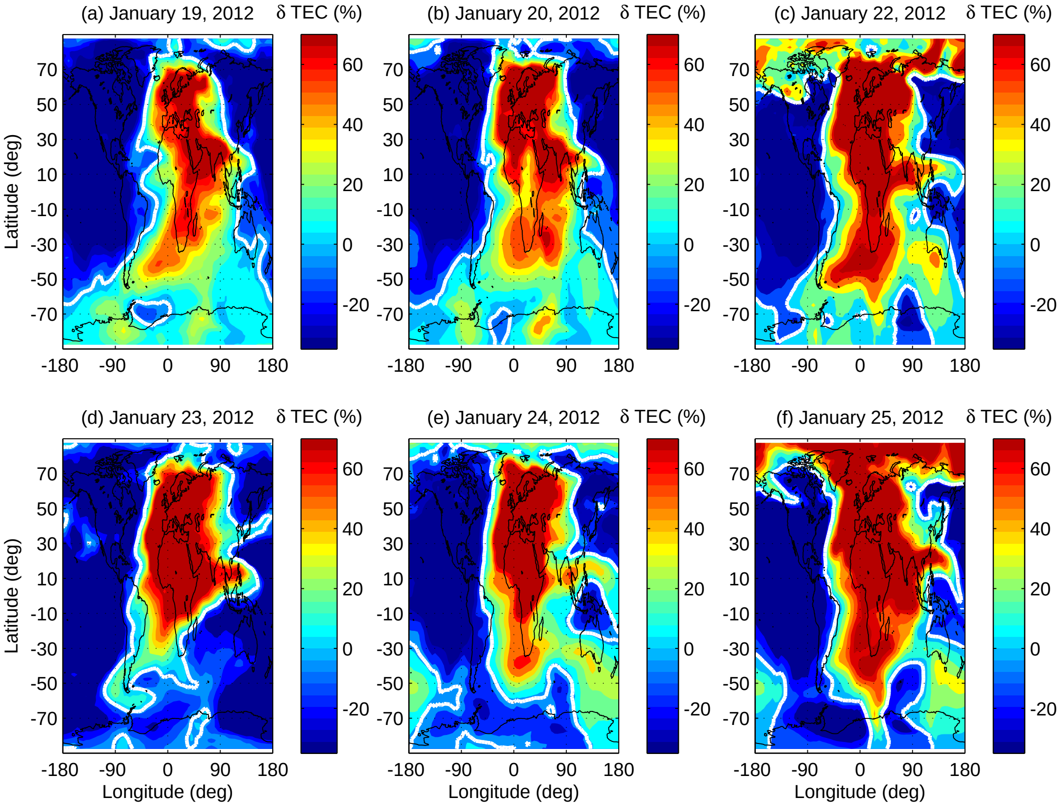

Figure 7.8: GPS-delta TEC snap shot over 6 days at 11 UTC hr.

and stationary planetary waves might have a role in creating the asymmetries. This point will be further treated later on when the impact of the geomagnetic storm on the wave components are discussed.

The main features in both diurnal and semidiurnal variances determined from the 21 days TEC time series are unlikely to be different from the climatology for this particular period as the climatology of the quiet days dominate. However, the geomagnetic storm induced TEC variations can modulate the amplitude and phase of the diurnal and semidiurnal tides in TEC time series. To this effect, we have already noted from wavelet coherence analysis that oscillations of $IMFBz$ with periodicity in the range of half to three days are coherent with the leading TEC PC at periods contained with 1.8-2.8 days Fig. 7.4 with a phase lag of 90^o. Fig. 7.11 shows the contribution of migrating diurnal tide before the storm occurrence on January 19 and during the storm events on January 22 and 25 at 12 UTC. The diurnal TEC anomaly on different days shows evidence of modulation of diurnal migrating tide by the storm as reflected in enhancement of diurnal TEC and its broader areal coverage on January 22 and 25 compared to January 19 quiet day. This difference is also apparent between the two geomagnetic storm days as shown by further increase in the diurnal TEC anomaly over East Africa longitude sector. This feature is already observed in the relative TEC change at 10 and 11 UTC in Figs. 7.7 (c, f)-7.8 (c, f).

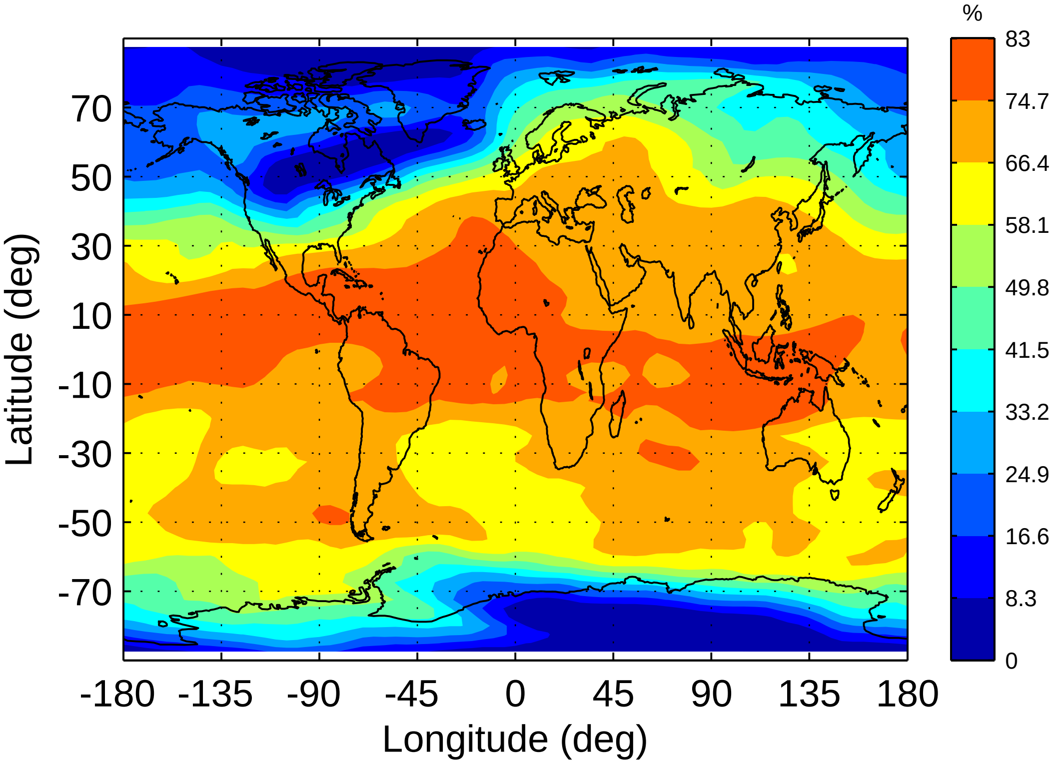

Figure 7.9: The diurnal variance of TEC

The semidiurnal global TEC variation is also analyzed. Fig (7.12) shows the

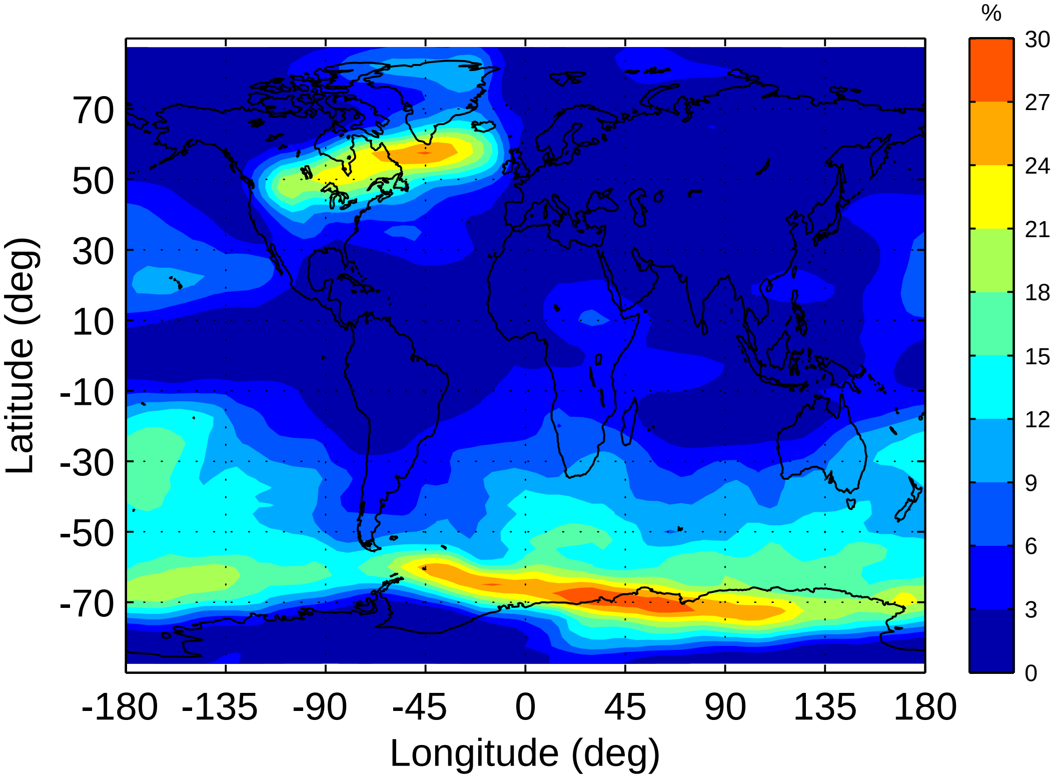

Figure 7.10: The semidiurnal variance of TEC

global semidiurnal variation of TEC at 12 UTC before and during the storm period. There is a clear change in both magnitude and phase of the semidiurnal tide from quiet day on January 19 (top panel) to geomagnetic storm days on January 22 and 25 (middle and bottom panels respectively). There is also a difference between the two storm days as marked by further enhancement of semidiurnal TEC and a shift in the locations of amplitude maxima and minima on January 25. This suggests the impact of the geomagnetic storm is not confined to initial location of the storm occurrence but covers wider area through modulation of all atmospherics waves. This disturbance can persist for a few more days beyond the life time of the storm when the modulation affects waves with longer periods.

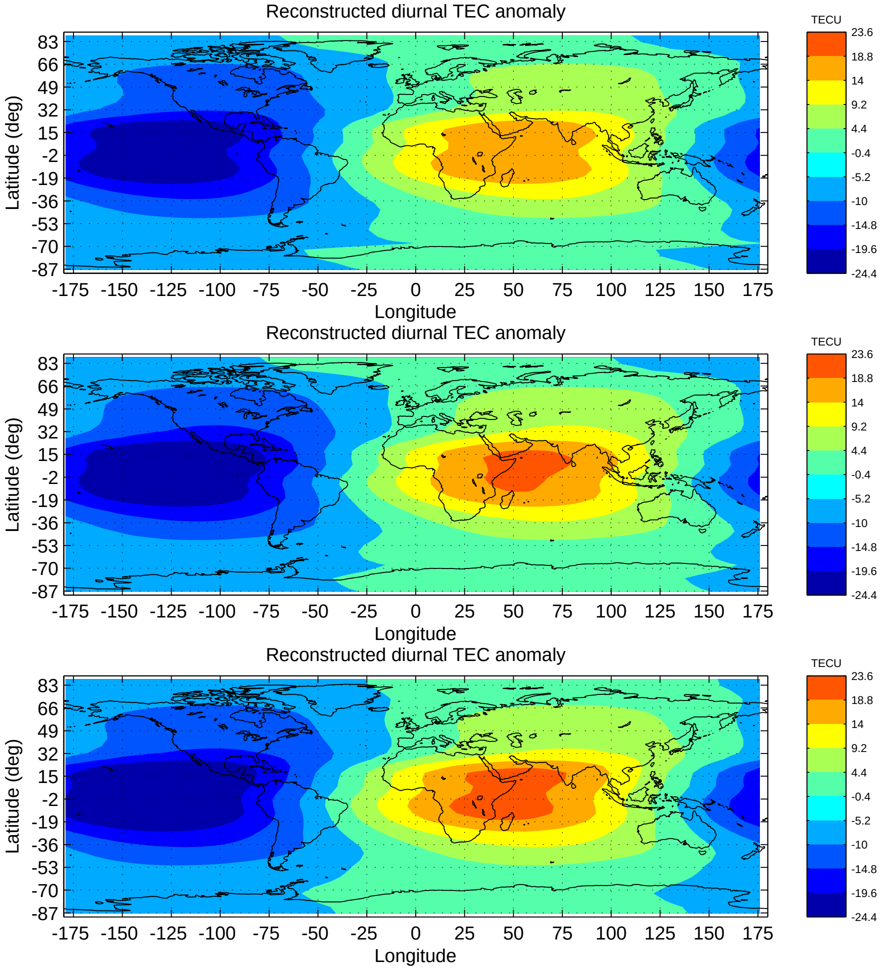

Reconstructed diurnal TEC anomaly

Reconstructed diurnal TEC anomaly

Reconstructed diurnal TEC anomaly

Figure 7.11: The variation of TEC due to diurnal tide at 12 UTC on January 19 (top), 22 (middle) and 25 (bottom).

The interhemispheric asymmetry observed in the diurnal and semidiurnal TEC variance is not observed in the reconstructed westward migrating tides in the TEC as expected confirming the asymmetry is caused by either non-migrating tides and/or stationary planetary waves that are known to introduce longitudinal TEC variability. This is because the diurnal and semidiurnal TEC variances include all signal with a period of 12 and 24 hours though the dominant ones are diurnal and semidiurnal migrating tides. To verify whether this is indeed the true reason, we reconstructed

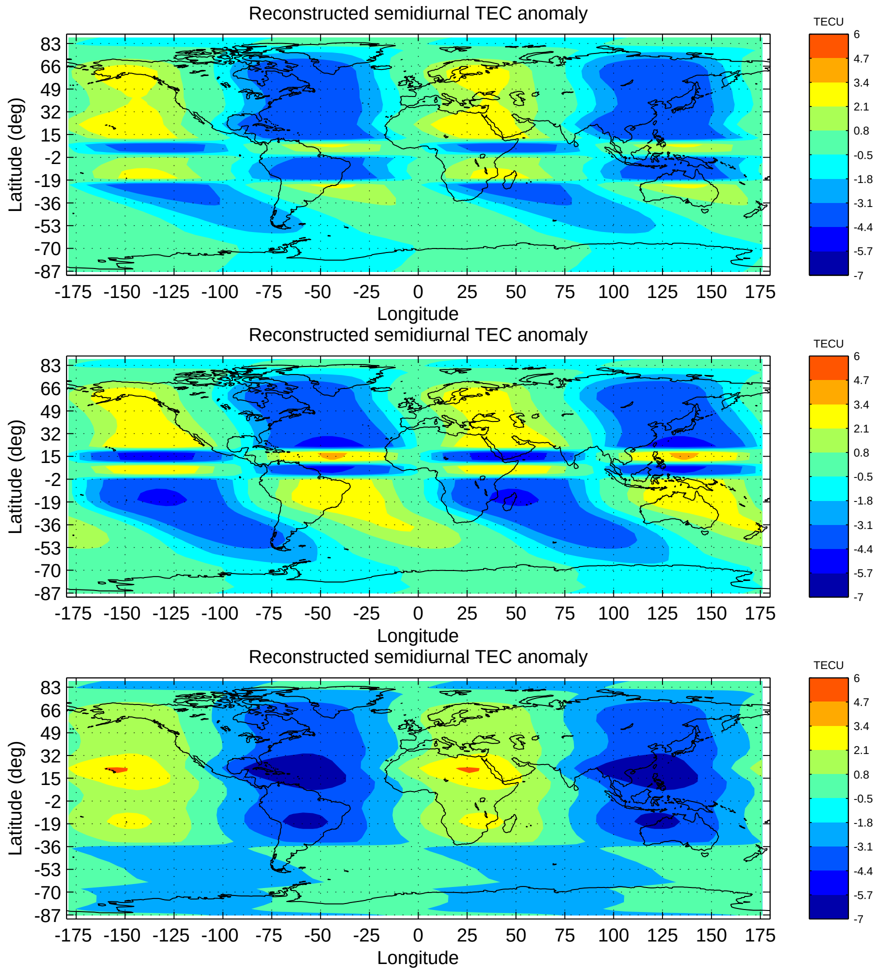

Figure 7.12: The variation of TEC due to semidiurnal tide at 12 UTC on January 19 (top), 22 (middle) and 25 (bottom).

the stationary planetary wave components of wave numbers 1 (Fig. 7.13) and 2 (not shown). Fig. 7.13 shows the stationary planetary wavenumber 1 for January 19 (top panel), 22 (middle), and 25 (bottom). The east-west interhemispheric asymmetry south of 70^oS in the TEC variances in Figs. 7.9-7.10 is the dominant feature of the stationary planetary wave with positive TEC anomaly over eastern hemisphere and negative TEC anomaly over western hemisphere as shown in Fig. 7.13 for the three days chosen to investigate the impact of the storm. This is feature holds true during all days considered in this study.

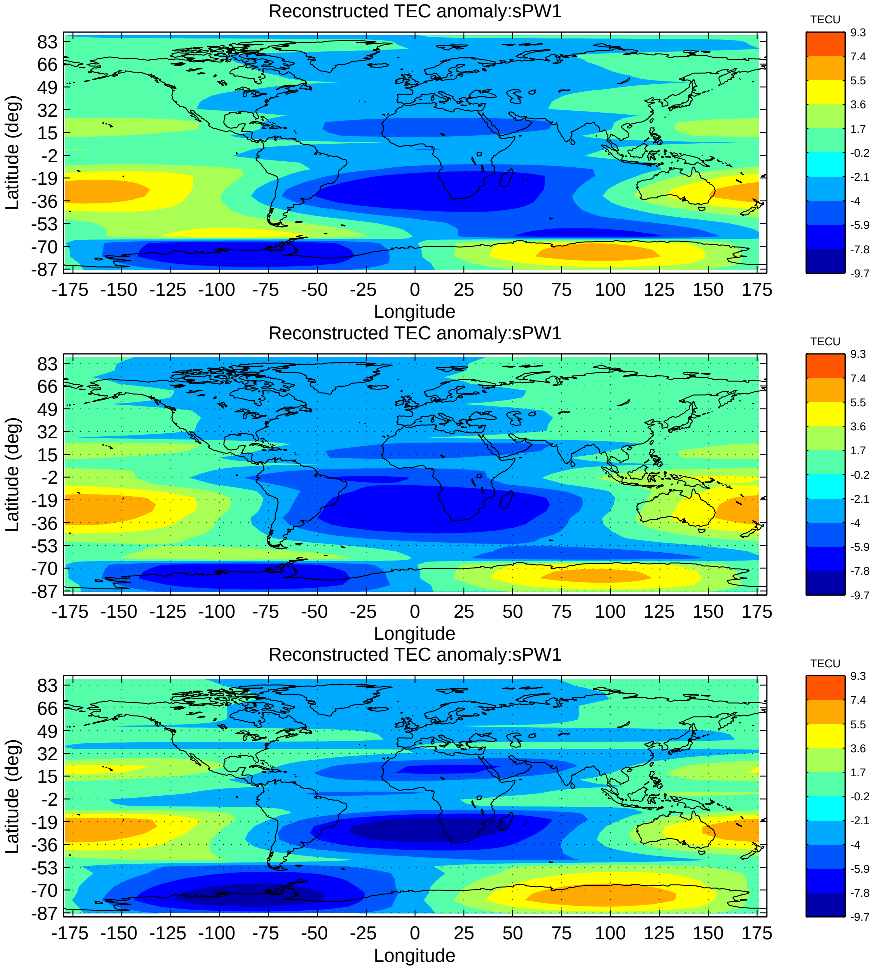
Reconstructed TEC anomaly:sPW1

Reconstructed TEC anomaly:sPW1

Reconstructed TEC anomaly:sPW1

Figure 7.13: The variation of TEC due to stationary planetary wavenumber 1 on January 19 (top), 22 (middle) and 25 (bottom).

The influence of the storm on the stationary planetary wave component of TEC is rather weak along 80^oS as seen from comparison of its component on quiet and disturbed days except enhancement that extends upto 53^oS over the eastern hemisphere on January 25. The impact of the storm can be seen in the amplitude of the stationary planetary wave with better contrast between periods before and after the storm in the following section.

7.0.2 Amplitude modulation of major wave components

To investigate the extent of storm influence on the amplitudes of prominant waves and possible modulution as already revealed for the leading principal component of TEC, we have reconstructed the daily amplitudes of diurnal and semidiurnal tide as well as that of stationary planetary waves. The influence of geomagnetic storm on diurnal and semidiurnal migrating tides can be seen distinctly from amplitude time series shown in Fig. 7.14. There is a sharp increase in the amplitude after storm occurrence on January 22 shown by dotted white line (day 8) in both diurnal and semidiurnal migrating tides for upto 5 more days. The increase in the amplitude of diurnal tide reaches upto a maximum of 5 TECU during the storm period within 10^oS-10^o N latitude band whereas the increment in the semidiurnal tide amplitude exceeds 2 TECU over the northern equatorial ionization anomaly regions. The change along the southern equatorial ionization anomaly region is quite insignificant.

The geomagnetic storm has also affected the amplitude of stationary planetary waves (Fig. 7.14, bottom). Fig. 7.14, bottom panel, has shown sharp gradient in the amplitude of wavenumber 1 after day 8 (i.e. January 22, 2012) along latitude band of 20-30^oS. There is also weak gradient beginning on day 9 (i.e. January 23) along 75-80^oS. The first distinct amplitude change is also reflected in the negative anomaly of upto 10 TECU in Fig 7.13 (bottom panel) on January 25 over southern Africa and Atlantic regions which differs from the other two days (top and middle panels) by upto 2 TECU on average. However, there is no difference over regions northward of 30^oN.

While our analysis so far shows the change in the amplitude of migrating tides and stationary planetary waves is due to the geomagnetic storm, it is not yet clear

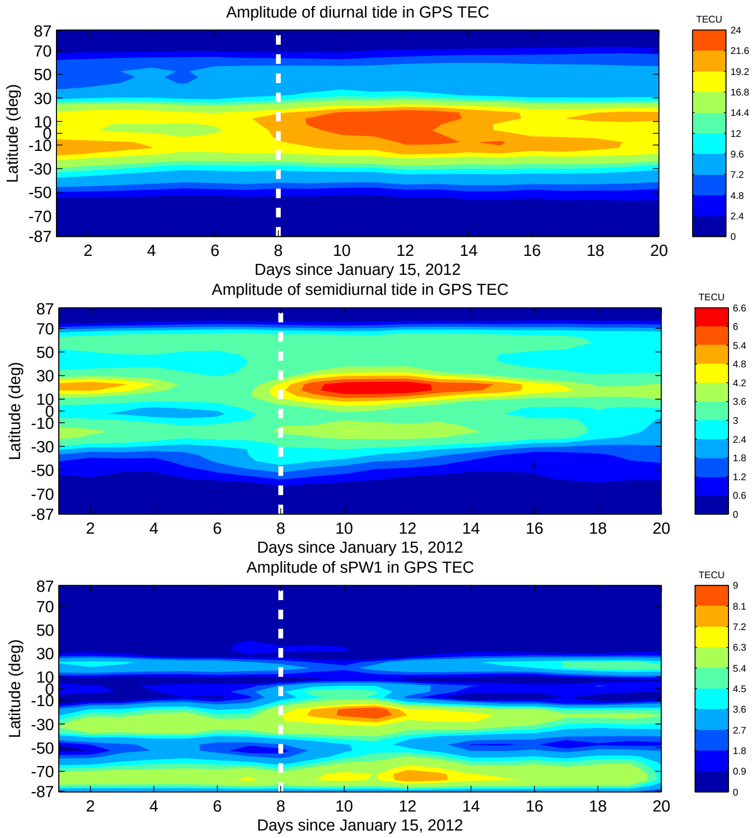

Figure 7.14: The amplitude of diurnal (top), semidiurnal (bottom) migrating tides and stationary planetary wavenumber 1 from January 15 to February 3, 2012. The white dotted line at day 8 shows January 22.

whether upward coupling from lower atmosphere through stationary and planetary waves has contributed to the modulation of the tides and stationary planetary waves observed ionospheric TEC. If this is not the case, then does the opposite occur and what is the extent of downward coupling during storm period is another interesting question to investigate. We have found from wavelet spectra of the amplitudes of the prominent waves at 17.5^o N or S that only the diurnal tides exhibit significant amplitude modulation of approximately 2.5-3 days period (Fig. 7.15) from January 22 (day 8) to January 30 (day 16) for about 9 days. Fig. 7.15 also shows there is

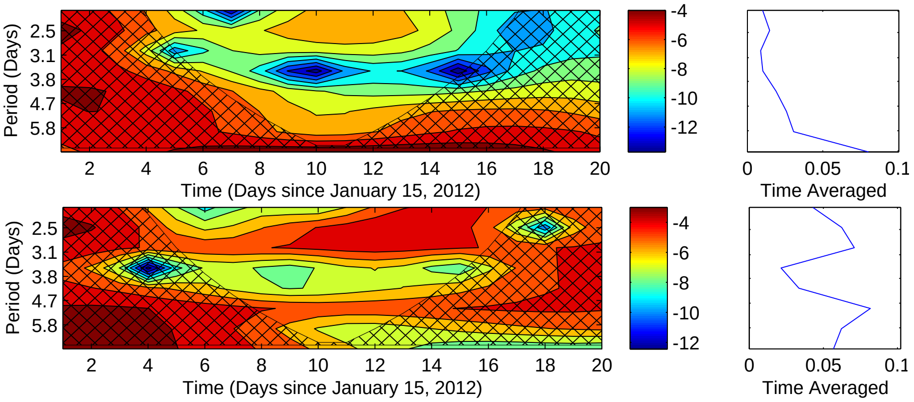

Figure 7.15: The wavelet power (left) and global wavelet spectra (right) for diurnal tide amplitude at 17.5 N (top) and 17.5 S (bottom).

a modulation of diurnal tide amplitude at 17.5^{o}S with a period of approximately 5 days. The former is similar to coherent oscillation observed in $IMFBz$ and TEC PC1 wavelet coherence spectra and therefore it is linked to the geomagnetic storm itself. However, since the 5-day modulation is not detected in the large scale TEC PC1 and $IMFBz$, it is either a localized feature not captured by the leading PC or planetary wave signal due to upward coupling. The former possibility is unlikely as there is no significant signal in the wavelet power of $IMFBz$ (see Fig. 7.4, middle panel). In this paper, as we focus on storm related impact on both ionosphere and lower atmosphere, we explore the modulation with periods within 2-3 days further in waves derived from both ionospheric TEC and microwave limb sounding (MLS) temperature in the upper mesosphere region. First, we ask whether the coherent oscillations of $IMFBz$ and TEC PC1 with a phase that characterizes impulse-response relationship between them has altered only the amplitudes of the diurnal, semidiurnal tides, stationary planetary waves as noted earlier or the geomagnetic storm has also induced new planetary waves or forced existing planetary waves at these particular frequencies (2-3 days cycle) in both the ionosphere and upper mesosphere.

Fig. 7.16 shows amplitude of planetary wavenumbers 1-3 signals with 2.4 days period in ionospheric TEC during January 15 to February 3, 2012. There is a distinct signals even before the geomagnetic storm occurrence for all three wavenumbers suggesting that the geomagnetic storm does not induce planetary waves at least with these particular specifications. However, there is prominent and significant amplitude modulations of the three planetary waves over equatorial ionization anomaly region beginning approximately on January 22 with minor difference between them on the onset of the amplitude modulations. The fact that the amplitudes of the planetary waves, in particular that of wavenumber 1, are already prominent before the storm indicates the coupling between lower atmosphere through E-region dynamo as discussed by several authors(refer here).

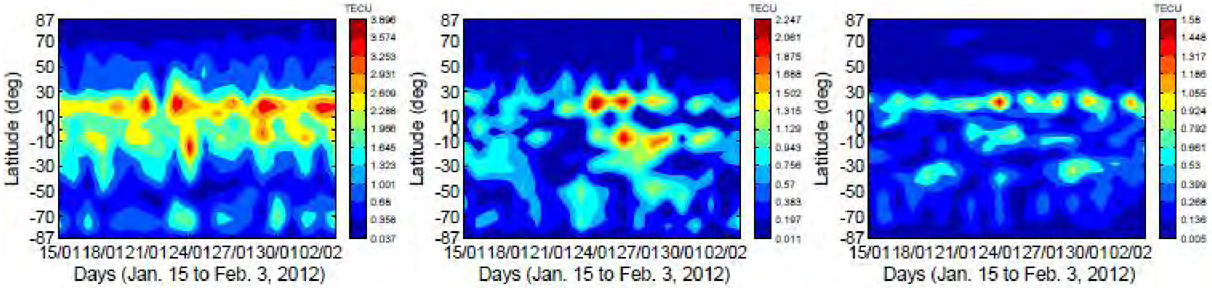

Figure 7.16: The amplitude of planetary waves determined from ionospheric TEC with period of 2.4 days for wavenumbers 1-3 (left to right).

This suggestion is also consistent with existence of planetary wave signals over northern hemisphere at all zonal wavenumbers detected from the upper mesospheric temperature measurement by MLS satellite before the geomagnetic storm occurrence (Fig. 7.17). However, the amplitudes planetary waves weakened after the storm over these latitudes for all the zonal wavenumbers. In contrast, the planetary waves, which was either nonexistent in the cases of zonal wavenumber 1-2 and weak in the case of wavenumber 3 over southern hemisphere, appeared or became stronger afterwards as shown in Fig. 7.17. To address whether the intense modulation of planetary waves in the ionospheric TEC and weakening over mesospheric altitude in northern hemisphere in conjunction with occurrence and/or strengthening of the same planetary waves over the opposite hemisphere following the storm occurrence are related to each other through vertical and horizontal couplings or not, we employed wind and temperature data from European Center for Medium Range Weather Forecasting (ECMWF) reanalysis to calculate Eliassen-Palm (EP) flux and divergence for use as diagnostic tools of wave activity between 10-1 hPa pressure level. This altitude region is the maximum covered by ECMWF reanalysis. We opted for the reanalysis data instead of using MLS geopotential heights to drive wind fields based on thermal wind relationship which is a crude approximation. The choice of a few pressure levels within 10-1 hPa in the lower mesosphere region while MLS covers much of the mesosphere is a choice over accuracy of the reanalysis wind as compared to thermal wind from MLS geopotential heights since calculation of EP flux and its divergence are sensitive to accuracy of the wind fields. The effect of tidal and planetary waves on the zonal mean wind can be investigated by diagnosing the momentum budget or EP flux divergence. EP flux divergence is a quantitative measure of the eddy forcing of the zonal mean flow. The utility of the EP flux as a diagnostic of wave propagation and wavemean flow interaction has been demonstrated successfully in a number of previous studies.

Fig. 7.18 shows EP flux and its divergence for four selected days representing pre-storm, storm and post-storm periods. During pre-storm period, e.g., on January 19,

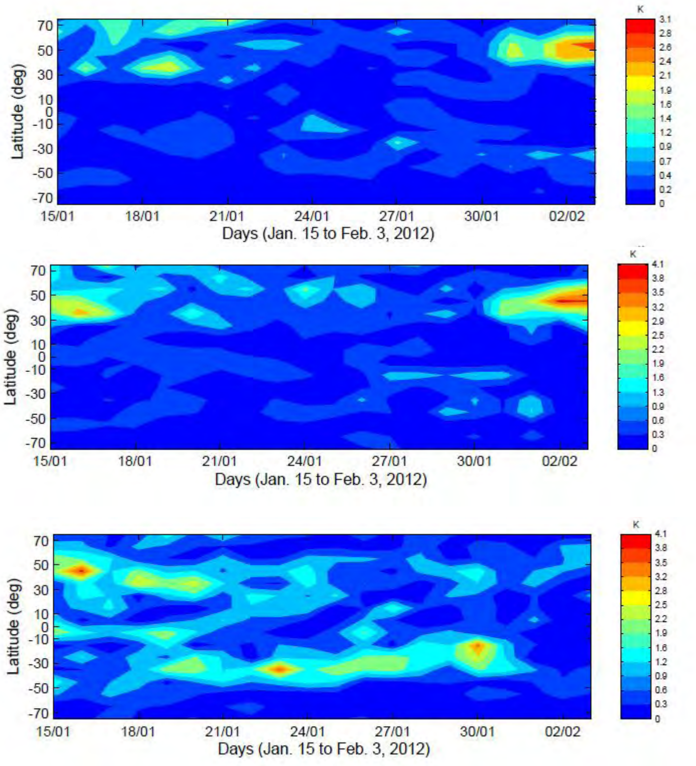

Figure 7.17: The amplitude of planetary waves determined from MLS temperature measurements with period of 2.4 days for wavenumbers 1-3 (top-bottom).

2012 (left-top panel), the EP flux points downward over regions poleward of 40^o N within the 10-1 hPa pressure levels implying poleward heat transport. This is infact the climatological feature of winter hemisphere circulation. However, on January 24 (top-right) and 25 (bottom-left), the EP flux vectors reverse directions poleward of 60^oN and their magnitude enhanced significantly. Though the region within 40-60^oN remains under downward pointing EP flux, the magnitude of the vectors were diminished drastically and at some altitudes reduced none. The intense upward flux, poleward of 60^o N, implies equatorward heat transport. A few days later on January 29, 2012 (bottom-right panel), the EP flux reversed direction pointing downward.

Under this circuminstances, the heat is transported poleward by eddies. The fact that during the two days of geomagnetic storm periods, the polar region is a heat source implies the auroral heating due to momentum and heat dissipation into these regions after the CME.

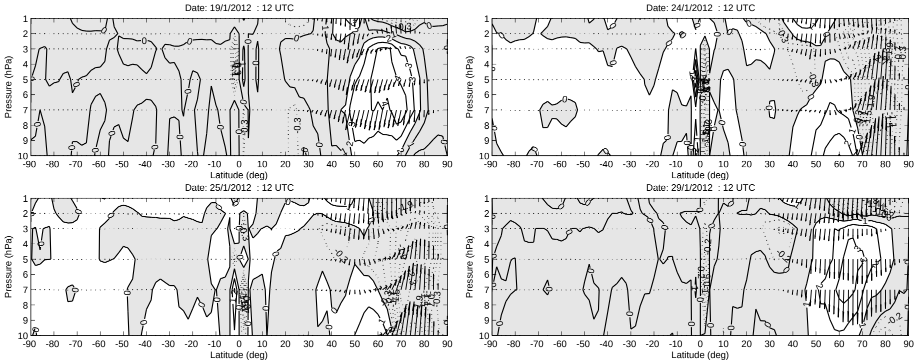

Figure 7.18: EP flux (vector) and divergence (contour). The negative EP flux divergence is shown by gray shade and dashed contours while positive values are shown by solid contours for January 19, 24, 25 and 29, 2012.

This reversal in the climatological directions of EP flux vectors over the lower mesosphere as determined from ECMWF reanalysis data can not be attributed to any other heat source due to the strength of the flux vectors and also the reversal is confined to the storm period. The question is how then these led to weakening of planetary waves of period 2.4 days in the mesosphere as determined from MLS temperature while on the otherhand, the same processes strengthened the planetary waves in the ionosphere. The forcing by CME is through energy dissipation by the precipitating particles into the mesosphere which alters the climatological circulation in almost reverse direction thereby weakening or completely reversing the zonal flow. This in turn interact with the wave in the context of wave propagation and wavemean flow interaction scheme thereby weakening or total dissipation of the waves in the northern hemisphere. However, the reverse circulation initiated by energy injection into the mesosphere is in phase with circulation in the southern hemisphere thereby triggering planetary waves. Therefore, the two wave processes in the ionosphere and the mesosphere regions are related.

Chapter 8

Conclusions

We have reviewed physics of Mesosphere, stratosphere and lower thermosphere that the equatorial plasma density distribution is modified by the zonal electric field at the magnetic equator, being the horizontal nature of the magnetic field at the magnetic equator leads to upward flow of plasma as a result of $E \times B$ drift. The formation of ionization trough at the magnetic equator and crests at $\pm 15^0$ is due to the pressure forces and gravity. The storm-time behavior of low latitude ionosphere is influenced by PPE and DDE. we have also reviewed that the amplitude and phase of atmospheric tides vary both with local time and annually.

The climatology from NeQuick and comparison to ionosond observations at low latitude electron density structure is analyzed using the simulated by ingesting GPS TEC into NeQuick2 model data and ionosonde data . The results show good agreement on quiet days but in the afternoon hours of the disturbed days the results begin to disagree. The spread F phenomena observed from ionosonde data which is not seen in the GPS TEC ingested into model data is an indication of geomagnetic disturbance. This is also clearly shown on the ionograms while electron density obtained from NeQuick2 show the same trend as the quiet days except the magnitude difference.

The EEJ diurnal and seasonal dependence are analyzed using model EEJM2 data and ground based magnetometers data. The result shows the diurnal EEJ current peaks at noon time due to the upward polarization electric field, which inturn produces an eastward Hall current. Both results from model data and measured data show strong seasonal variability. However the magnitude of EEJ is not the same throughout the year. Thus E season EEJ current is larger in magnitude than D and J seasons. Analysis of CEJ current shows that CEJs are not a night and noon time phenomena rather they occur at morning and afternoon hours while PRE is a post sunset phenomena.

Geomagnetic storms have occurred during January 22-25, 2012 period. The Dst values for the period shows that they are moderate intensity geomagnetic storms. The $SYM-H$ value on January 22 shows a sudden increase to more than 50 nT at the sudden storm commencement (SSC) and followed by sharp decrease to a value of -100 nT after which a recovering starts. A second SSC on January 24 followed by a shock on January 25. The SSCs before the main storms on January 22 and 25 are evidences for the occurrence of Coronal Mass Ejection (CME). Moreover, the short recovery period, unlike that of Corotating Interaction Regions (CIR) driven geomagnetic storms, implies the geomagnetic storm is a CME-driven. The sudden jump of the solar wind dynamic pressure and the IMF B_z are also consistent with occurrence of CME. Proton fluxes of high energy ranges and increase in proton density are also other indicators for occurrence of CME.

The high values auroral electrojet (AE) index on these dates implies ionospheric perturbation in response to the storm. This is also reflected in the total electron content (TEC) change during the storm relative to quiet day TEC over the polar regions. A jump from about 35 TECU on January 20 to 60 TECU on January 25 is observed at TEC peak hours of 9:30-10:30 UTC over geomagnetic equator at Addis Ababa, Ethiopia. Moreover,during the disturbed days especially on January 23, the southern hemisphere TEC is highly depleted while TEC is accumulated over the northern hemisphere. This could be an indication of transport of plasma towards the equatorward from southern hemisphere in line with the fact that in summer, the storm induced circulation augments the normal seasonal circulation from summer to winter hemisphere where the composition disturbance can easily be transported to mid- and low-latitudes. In contrast, in the winter, the storm induced circulation competes with the seasonal flow thereby constraining the composition to high latitudes as distinctly exhibited over polar regions.

The response of the ionospheric to geomagnetic storms is also investigated from amplitude modulation of wave components that account for the majority of TEC variance during the period. The diurnal and semidiurnal TEC variances account upto a maximum of 83% and 30% of the TEC variance over fairly exclusive ionospheric regions respectively. The diurnal variability dominates the subtropical latitude where the solar cycle is an important factor while the semidiurnal variance is limited to higher latitudes. The diurnal and semidiurnal TEC variances show hemispheric asymmetries. The hemispheric asymmetry observed in the diurnal and semidiurnal TEC variance is not observed in the reconstructed westward migrating tides in the TEC as expected confirming the asymmetry is caused by either non-migrating tides and/or stationary planetary waves. The stationary planetary waves also account for TEC variances that exceed semidiurnal TEC variance and exhibit hemispheric asymmetry of opposite sign to diurnal TEC variance. These features of TEC variance are climatology of TEC variability during the analysis time window irrespective of the storms. However, the impact of the geomagnetic storms are distinctly marked in the daily time series of amplitudes of diurnal and semidiurnal migrating tides and stationary planetary waves. The abrupt changes in amplitudes, in response to the geomagnetic storms, of diurnal (upto 5 TECU) and semidiurnal (upto 2 TECU) migrating tides are observed within the 20^oS-20^o latitude band and along 20^o N respectively while that of stationary planetary wavenumber 1 is in the order of 3 TECU and is mainly localized along 20^oS.

In summary, we have shown for the first time to our knowledge how geomagnetic storms influence the wave dynamics that control ionospheric TEC variability. However, more silent features of the causal relationship between the storms and wave dynamics can be revealed with further analysis of more geomagnetic storms during different seasons. This will be our future focus area.

Bibliography

[1] M. Moldwin. *An introduction to space weather.* Cambridge University Press, New York, 2008.

[2] Nat Gopalswamy. Coronal mass ejections and space weather. *Selected papers from the 2007 Kyoto Symposium*, pages 77–120, 2009.

[3] J. K. Hargreaves. *The solar-terrestrial environment: An introductory to geosphace-the science of the terrestrial upper atmosphere, ionosphere and magnetosphere.* Cambridge University Press, New York, 1992.

[4] E. I. Astafyeva. Effects of strong IMF B_z southward events on the equatorial and mid-latitude ionosphere. *Ann. Geophys.*, 27:1175–1187, 2009.

[5] M. A. Abdu, G. O. Walker, G. B. M. Reddy, J. H. A. Sobral, B. G. Fejer, T. Kikuchi, N. B. Trivedi, and E. P. Szuszczewicz. Electric field versus neutral wind control of the equatorial anomaly under quiet and disturbed conditions: A global perspective from SUNDIAL-86. *Ann. Geophys.*, 8:419–430, 1990.

[6] M. Forster and N. Jakowski. Geomagnetic storm effects on the topside ionosphere and plasmasphere: a compact tutorial and new results. *Surv. Geophys.*, 21:47–87, 2000.

[7] E. I. Astafyeva, E. L. Afraimovich, and E. A. Kosogorov. Dynamics of total electron content distribution during strong geomagnetic storms. *Adv. Space Res.*, 39:1313–1317, doi:10.1016/j.asr.2007.03.006, 2007.

[8] S. Basu, Su. Basu, F. J. Rich, K. M. Groves, E. MacKenzie, C. Coker, Y. Sahai, P. R. Fagundes, and F. Becker-Guedes. Response of the equatorial ionosphere at dusk to penetration electric fields during intense magnetic storms. *J. Geophys. Res.*, 12:A08308, doi:10.1029/2006JA012192, 2007.

[9] B. T. Tsurutani, A.Mannucci, B. Iijima, M. A. Abdu, J. H. A. Sobral, W. Gonzalez, F. Guarneri, and T. Tsuda. Global dayside ionospheric uplift and enhancement associated with in terplanetary electric fields. *J. Geophys. Res.*, 109:A08302, doi:10.1029/2003JA010342, 2004.

[10] A. J. Mannucci, B. T. Tsurutani, B. A. Iijima, A. Komjathy, A. Saito, W.D. Gonzalez, F. L. Guarnieri, J. U. Kozyra, and R. Skoug. Dayside global ionospheric response to the major interplanetary events of October 29-30, 2003 ”Halloween Storms”. *Geophys. Res. Lett.*, D, 32:12, doi:10.29/2004GL021467, 2005.

[11] B. T. Tsurutani, O. P. Verkhoglyadova, A.J. Mannucci, T. Araki, A. Sato, T. Tsuda, and K. Yumoto. Oxygen ion uplift and satellite drag effects during the 30 October 2003 daytime super fountain event. *Ann. Geophys.*, 25:569–574, http://www.ann–geophys.net/25/569/2007/, 2007.

[12] B. T. Tsurutani, O. P. Verkhoglyadova, A.J. Mannucci, A. Saito, T. Araki, K. Yumoto, T. Tsuda, M. A. Abdu, J. H. A. Sobral, W. D. Gonzalez, H. McCreadie, G.S. Lakhina, and V. M. Vasyliunas. Prompt penetration electric fields (PPEFs) and their ionospheric effects during the great magnetic storm of 30-31 October 2003. *J. Geophys. Res.*, 113:A05311, doi:10.1029/2007JA012879, 2008.

[13] A. D. Danilov and L. D. Belik. Thermosphere composition and the positive phase of an ionospheric storm. *Adv. Space Res.*, 12:257–260, 1992.

[14] A. D. Danilov and Lastovicka. Effects of Geomagnetic storms on the ionosphere and atmosphere. *Int. J. Geomagn. Aero.*, 2:209–284, 2001.

[15] C.-S. Huang, J. C. Foster, and M. C. Kelley. Long-duration penetration of the interplanetary electric field to the low-latitude ionosphere during the main phase of magnetic storms. *J. Geophys. Res.*, 110:A11309, doi:10.1029/2005JA011202, 2005.

[16] Y. Wei, M. Hong, W. Wan, A. Du, J. Lei, B. Zhao, W. Wang, Z. Ren, and X. Yue. Unusually long lasting multiple penetration of interplanetary electric field to equatorial ionosphere under oscillating IMF Bz. *Geophys. Res. Lett.*, 35:L02102, doi:10.1029/2007GL032305, 2008.

[17] X. Zhang, J. M. Forbes, and M. E. Hagan. Longitudinal variation of tides in the MLT region :tides driven by tropospheric net radiative heating. *Geophys. Res. Lett.*, 115:A06316, doi:10.1029/2009JA014897, 2010.

[18] Q. Wu, D. A. Ortland, T. L. Killeen, R. G. Roble, M. E. Hagan, H.-L. Liu, S. C. Solomon, Jiyao Xu, W. R. Skinner, and R. J. Niciejewski. Global distribution and interannual variation of mesospheric and lower thermospheric neutral wind diurnal tide. *Geophys. Res. Lett.*, 113:A05308, doi:10.1029/2007JA012542, 2008.

[19] H. Limura, S. E. Palo, and Q. Wu. Nonmigrating Semidiurnal tide over Arctic determined from TIMED Interferometer wind observations. *J. Geophys. Res.*, 115:D06109, doi: 10.1029/2009JD012733, 2010.

[20] J. H. A. Sobral, M. A. Abdu, C. S. Yamashita, A. C. Gonzales, I. S. de Batista, C. J. Zamlutti, and B. T. Tsurutani. Responses of the low latitude ionosphere to very intense geomagnetic storms. *J. Atmos. Solar. Phys.*, 63:965–974, 2001.

[21] J.O. Adeniyi. Magnetic storm effect on the morphology of the equatorial F2-layer. *J. Atmos. Terr. Phys.*, 48:695–702, 1986.

[22] T. Turunen and M. N. Rao. Examples of the influence of strong magnetic storms on the equatorial F-layer. *J. Atmos. Terr. Phys.*, 42:323–330, 1980.

[23] T. Maruyama, G. Ma, and M. Nakamura. Signature of TEC storm on 6 November 2001 derived from dense GPS receiver network and ionosonde chain over Japan. *J. Geophys. Res.*, 109:A10302, doi:http://dx.doi.org/10.1029/2004JA010451, 2004.

[24] H. Jin and T. Maruyama. Temporary decrease in daytime F-region peak electron density due to eastward electric field penetration during magnetic storm. *J. Geophys. Res.*, 113:A05305, doi:http://dx.doi.org/10.1029/2006JA011928, 2008.

[25] C.-S. Huang, J. C. Foster, L.P. Goncharenko, P.J. Erickson, W. Rideout, and A.J. Coster. A strong positive phase of ionospheric storms observed by the millstone hill incoherent scatter radar and global gps network. *J. Geophys. Res.*, 110:A06303, doi:10.1029/2004JA010865, 2005.

[26] M. Swisdak, J.D. Huba, G. Joyce, and C.-S. Huang. Simulation study of a positive ionospheric storm phase observed at Millstone Hill. *Geophys. Res. Lett.*, 33:L02104, doi:10.1029/ 2005GL024973, 2006.

[27] M. C. Kelley. *The earth's atmosphere plasma physics and electrodynamics.* Academic press, Sandiago, 1989.

[28] Asgier Brekke. *TPhysics of upper polar atmosphere.* John Wiley and sons., Praxis publishing Chichester, 1995.

[29] M. G. Kivelson and C. T. Russell. *Introduction to Space Physics.* Cambridge university press, United States of America, 1995.

[30] W. Lee, H. Kil, Q. Wu, J. Chung, and J. Park. Seasonal variation of the ionospheric f2-layer intensity at midlatitudes during the solar cycle 23. *Geophysical Union*, 35:AGUFMSA51B1227L, 2009.

[31] L. Liu, B. Zhao, W. Wan, B. Ning, M-L. Zhang, and M. He. Seasonal variations of the ionospheric electron densities retrieved from Constellation Observing System for Meteorology, Ionosphere, and Climate mission radio occultation measurements. *J. Geophys. res.*, 114:A02302, doi:10.1029/2008JA013819, 2009.

[32] A. M. Rahman, P. K. Manoharan, and S. Umpathy. Propagation characteristics of coronal mass ejections and their effects at the near-earth environment. *Indian J. radio and space Phys.*, 39:276–279, 2010.

[33] B. G. Fejer and L. Scherlies. Time dependent response of equatorial ionospheric electric fields to magnetospheric disturbances. *Geophys. Res. lett.*, 22:851, 1995.

[34] R. Schunk and A. Nagy. *Ionospheres Physics, Plasma physics, and Chemistry.* Cambridge University press, New York, 2009.

[35] A. Schuster. The diurnal variation of terrestrial magnetism. *Philos. Trans. R. Soc. London*, 208:Ser. A, 208, 163–204., 1889.

[36] D. Anderson, A. Anghel, J. Chau, and O. Veliz. Daytime vertical $E \times B$ drift velocities inferred from ground-based magnetometer observations at low latitudes. *Space Weather*, 2:S11001, http://dx.doi.org/10.1029/2004SW000095, 2004.

[37] Y. Yamazaki, K.Yumoto, T. Uozumi, S. Abe, M. G. Cardinal, D. MacNamara, R. Marshal, B. M. Shevtsov, and S. I. Solouyev. Reexamination of the sq eej relationship based on extendedmagnetometer networks in the east Esian region. *J. Geophys. res.*, 115:A09319, doi:10.1029/2010JA015339, 2010.

[38] J Forbes. The equatorial electrojet. *Rev. Geophys.*, 19:469–504, 1981.

[39] R. Rastogi. The equatorial electrojet, in geomagnetism. *Academic, San Diego*, 3:461525, 1983.

[40] A. Kuvshinov, C. Manoj, N. Olsen, and T. Sabaka. On induction effects of geomagnetic daily variations from equatorial electrojet and solar queit sources at low and middle latitudes. *J. Geophys. res.*, 112:B10102, doi:10.10292007JB004955, 2007.

[41] J. Park, H. Luhr, and K. W. Min. Climatology of the inter-hemispheric field-aligned current system in the equatorial ionosphere as observed by CHAMP. *Ann. Geophys.*, 29:573582, 2011.

[42] R. S. Heelis. Equatorial in the low and middle latitude ionosphere: A tutorial. *J.Atmos. Sol.Terr. phys.*, 66:815–838, doi: 10.1016/j.jastp.2004.01.034, 2004.

[43] H. Rishbeth. The ionosphere E-layer and F-layer dynamos -a tutorial review. *J.Atmos. Sol.Terr. phys.*, 59 (15):1873–1880, 1997.

[44] W. G. Barker and D. F. Martyn. Electric currents in the ionosphere I. the conductivity. *Royal Society of London*, 246:281–294, 1953.

[45] M. C. Kelley, R. R. Ilma, and G. Crowley. On the origin of pre-reversal enhancement of the zonal equatorial electric field. *Ann. Geophys.*, 27:2053–2056, 2009.

[46] N. Maruyama, S. Watanabe, and T. J. Fuller-Rowell. Dynamic and energetic coupling in the equatorial ionopsphere and theremosphere. *J. Geophys. res.*, 108:A11, 1396, doi:10.1029/2002JA009599, 2003.

[47] T. W. Fang, A. D. Richmond, J. Y. Liu, and A. Maute. Wind dynamo effects on ground magnetic perturbations and vertical drifts. *J. Geophys. Res.*, 113:A11313, doi:10.1029/2008JA013513., 2008.

[48] D. N. Anderson, A. Anghel, K. Yumoto, M. Ishitsuka, and E. Kudeki. Estimating deytime vertical $e \times b$ drift velocities in the equatorial f region using ground based magnetometer observations. *Geophys. Res. Lett.*, 29:doi:10.1029/2001GL014562, 2002.

[49] K. Davies. *Ionospheric Radio, radio waves Propagation of effects on ionosphere.* Peter peregrinnes Ltd., Lonodon, United Kingdom, 1989.

[50] S. Maus, M. Rother, C. Stolle, W. Mai, Choi S, H. Luhr, D. Cooke, and C. Roth. Third generation of the postdom magnetic model of the earth (POMME). *Geochem. Geophys. Geosyst.*, 7:Q67008, doi: 10.1029/2006GC001269, 2006.

[51] D. Russell. The equatorial electrojet. *Res. Society Quarterly*, 39, 2002.

[52] S. Chapman. The equatorial eletrojet as detected from the abnormal distribution above Huancayo and elsewhere. *Arch. Meteorl. Geophys. Bioclimatol.*, A4:368–392, 1951.

[53] H. Rishbeth. Polarization fields produced by winds in the equatorial F- rgion. *Planet space sci.*, 19:357–369, 1971.

[54] D. T Farely, E . Bonelli, B. G. Fejer, and M. F. Larsen. The Prereversal Enhancement of the Zonal Electric Field in the Equatorial Ionosphere. *J. Geophys. Res.*, 91:13723–13728, 1986.

[55] E. B. Shume, E. R. dePaula, S. Maus, D. L. Hysell, F. S. Rodriguess, and A. Bekele. Equatorial zonal electric field inferred from a 3-D electrostatic potential model and ground based magnetic field measurements. *J. Geophys. res.*, 114:doi:10.1029/2009JA014158, 2009.

[56] P. Muralikrishna and V. H. Kulkarni. On the height variation of the E-region cowling conductivity -effects of charged dust particles. *Ann. Geophys.*, 24:2949–2957, 2006.

[57] T. Dautermann and E. Calais. *TEC Data Processing Software.* Purdue University., 2008.

[58] B. Bidaine and R. Warnant. Assessment of the NeQuick model at mid-latitudes using GNSS TEC and ionosonde data. *Adv. space Res.*, 45:11221128, 2010.

[59] E. Yizengaw, E. A. Essex, and R. Bisra. The southern hemisphere and equatorial region ionization response for September 22, 1999 severe magnetic storm. *Ann. Geophys.*, 22(8):2765–2773, 2004.

[60] N.V. Rao, T. Madhu, and K. L. Kashore. Geomagneticstorm effects on GPS aided Navigation over low latitude south indian region. *IJCSNS International Journal of Computer science and Network Security*, 10:2765–2773, 2010.

[61] Z. Li, F. Wei, X. Feng, J. Guo, B. A. Emery, and X. Zhao. Large ionospheric disturbances during a minor geomagnetic storm on june 23, 2000. *Ann. Geophys.*, 55:2, doi: 10.4401/ag–5409, 2012.

[62] S. M. Radicella and R. Lietinger. The Evolution of the DGR approach to model electron density profiles. *Adv, space Res.*, 27:35–40, 2001.

[63] S. M. Radicella and M. L. Zhang. The Improved DGR analytical model of electron density height profile and total electron content in the ionosphere. *Ann. Geophys.*, 1:35–41, 1995.

[64] B. Nava, P. Coisson, G. M. Amarante, F. Aziplicueta, and S. M. Radicella. A model assisted reconstraction method based on verical TEC data ingestion. *Annals of Geophysics*, 42 (2):107–119, 2005.

[65] B. Nava, P. Coisson, and S. M. Radicella. A new version of NeQuick ionosphere electron density model. *J.Atmos. Sol.Terr. phys.*, 70:1856–1862, 2008.

[66] P. Coisson, S.M Radicella, R. Leitinger, and B. Nava. Topside electron density in iri and nequick: Features and limitations. *ann. Geophys.*, 37:937–942, 2006.

[67] R. Leitinger, M. L. Zhang, and S. M. Radicella. An improved bottomside for the ionospheric electron density model NeQuick. *Ann. Geophys.*, 11:17–25, 2005.

[68] C. Manoj, H. Luhr, S. Maus, and N. Nagarajan. Evidence for short spatial correlation lengths of the noontime equatorial electrojet inferred from a comparison of satellite and ground magnetic data. *Ann. Geophys.*, 111:A11312, doi:10.1029/2006JA011855, 2006.

[69] R. G. Rastogi, H. Chandra, and M. E. James. Characteristics of equatorial electrojet current in the central regions of South America. *Earth Planets Space*, 60:623–632, 2008.

[70] A. B. Rabiu, A. I. Mamukuyomi, and E. O. Joshua. Variability of equatorial ionosphere inferred from geomagnetic field measurements. *Bull. Astr. Soc. India*, 35:607–618, 2007.

[71] M. E. Mann and J. Park. Joint spatiotemporal modes of surface temperature and sea level pressure variability in the northern hemisphere during the last century. *J. Climate*, 9:2137–2162., 1996.

[72] M. E. Mann and J. Park. Greenhouse warming and changes in the seasonal cycle of temperature: Model versus observations. *Geophys. Res. Lett.*, 23:1111–1114., 1996.

[73] M. E. Mann, U.Lall, and B. Saltzm. Decadal-to- centennial-scale climate variability: Insights into the rise and fall of the great salt lake. *J. Geophys. Res.*, 28:937940., 1995.

[74] T. L. Delworth and M. E. Mann. Observed and simulated multidecadal variability in the Northern Hemisphere. *Climate Dynamics*, 16:661–676, 2000.

[75] P. Somkiat, G. J. Mccabe, B. Rajagopalan, and S. Gangopadhyay. Joint Spatiotemporal Variability of Global Sea Surface Temperatures and Global Palmer Drought Severity Index values. *J. Climate*, 22:6251–6267, 2009.

[76] Tsidu G. Mengistu and K. Ture. Mechanisms of ozone enhancement during stratospheric intrusion coupled with convection over upper troposphere equatorial africa. *Atmospheric Environment*, 70:410424, http://dx.doi.org/10.1016/j.atmosenv.2013.01.024., 2013.

[77] Tsidu G. Mengistu, K. Ture, and V. Sivakumar. Observational evidence of planetary wave influences on ozone enhancements over upper troposphere north africa. *Atmospheric Research*, 70:129–130, 1–19, http://dx.doi.org/10.1016/j.atmosres.2013.04.001, 2013.

[78] D. Pancheva, P. Mukhtarov, and B. Andonov. Nonmigrating tidal activity related to the sudden stratospheric warming in the arctic winter of 2003/2004. *Ann. Geophys.*, 27:975–987, 2009.

[79] L. He, L. Wu, S. Pulinets, S. Liu, and F. Yang. A nonlinear background removal method for seismo-ionospheric anomaly analysis under a complex solar activity scenario: A case study of the M9.0 Tohoku earthquake. *Advances in Space Research*, 50:211220, 2012.

[80] E. Eliassen and E. Palm. On the transfer of energy in stationary mountain waves. *Geofys. publ.*, 22:No3, 123, 1961.

[81] D. G. Andrews, D. J. Mahlman, and R. W. Sinclair. Eliassen-Palm Diagnostics of wave-mean flow interaction in the GFDL "SKYHI" General Circulation Model. *J. Atmos. Science*, 40:27682784, 1983.

[82] A. R. Plumb and R. Ferrari. Transformed Eulerian-Mean Theory. Part I: Nonquasigeostrophic Theory for Eddies on a Zonal-Mean Flow. *American meteorological society*, 35:165174, 2005.

[83] H. Yang, K. K. Tung, and E. Olaguer. Nongeostrophic theory of zonally averaged circulation part II:Eliassen-Palm flux divergence and isotropic mixing coefficents. *American meteorological society*, 47:215241, 1990.

[84] M. Nigussie, S. M. Radicella, B. Damtie, B. Nava, E.Yizengaw, and L. Ciraolo. TEC ingestion in to NeQuick2 to model the East African equatorial ionosphere. *Radio Science*, 47:RS5002, doi: 10.1029/2012RS004981, 2012.

[85] R.-S. Kim, K.-S. Cho, Y.-J. Moon amd M. Dryer, J. Lee, Y. Y., K.-H. Kim, H. Wang, Y.D. Park, and Y. H. Kim. An empirical model for prediction of geomagnetic storms using initially observed CME parameters at the Sun. *J. Geophys, res.*, 115:A12108, doi:10.1029/2010JA015322, 2010.

[86] S. Chapman. The solar and lunar diurnal variation of the earth's magnetism. *Phil. Trans Roy. sol. Lond.*, A218:1–118, 1919.

[87] F. N. Okeke and Y. Hamano. Daily variations of geomagnetic H D and Z-fields at equatorial latitudes. *Earth Planets Space*, 52:237–243, 2000.

[88] J. Egedal. The magnetic diurnal variation of the horizontal force near the magnetic equator. *Terr. Magn. Atmos.*, 52:449–451, 1947.

[89] F. N. Okeke, C. A. Onwumechili, and B. A. Rabiu. Day-to-day variability of geomagnetic hourly amplitudes at low latitudes. *Geophys. J. Int.*, 134:484–500, 1998.

[90] B. G. Anandarao and R. Raghavarao. Structural changes in the currents and fields of the equatorial electrojet due to zonal and meridional winds. *J. Geophys. Res.*, 92:2514–2526, 1987.

[91] R Raghvarao and B. G. Anandarao. Vertical winds as a plausible cause for equatorial counter electrojet. *Geophys. Res. Lett.*, 7:357–360, 1980.

[92] V. V. Somayajulu, R. Selvamurugan, C. V. Devasia, and L. Cherian. VHR back scatter radar observations of type i waves during a counter electrojet events. *Geophys. Res. Lett.*, 21:2047–2050, 1994.

[93] C. Vineeth, T. K. Pant, C. V. Devasia, and R. Sridharan. Highly localized cooling in daytime mesopause temperature over the dip equator during counter electrojet events: First results. *Geophys. Res. Lett.*, 34:L14101, doi:10.1029/2007GL030298., 2007.

[94] D. Anderson, Araujo-pradere E, and L. Scherliess. Comparing daytime, equatorial $e \times b$ drift velocities and TOPEX/TEC observations associated with the 4-cell, non-migrating tidal structure. *Ann. Geophys.*, 27:2861–2867, 2009.

[95] E. Yizengaw, J. Dewar, J. MacNeil, M. B. Moldwin, D. Galvan, J. Sanny, D. Berube, and Bill Sandel. The occurrence of ionospheric signitures of plasmaspheric plumes over different longitudinal sector. *J. Atmos. Sol. Terr. Phys.*, 113:A08318, doi:10.1029/2007JA012925, 2008.

[96] C. M. Denardini, M. A. Abdu, H. C. Aveiro, L. C. A. Resende, P. D. S. C. Almeida, E. P. A. Olivio, J. H. A. Sobral, and C. M. Wrasse. Counter electrojet features in the brazilian sector: Simultaneous observation by radar, digital sounder and magenetometers. *Ann. Geophys.*, 27:1593–1603, 2009.

[97] I. S. Batista, M. A. Abdu, and J. A. Bittencourt. Equatorial F region vertical drifts: Seasonal and longitudinal asymmetries in the American sector. *J. Geophys. res.*, 91:12055–12064, 1986.

[98] M. A. Abdu, I. S. Batista, G. O. Walker, J. H. A. Sobral, N. B. Trivedi, and E. R. de Paula. Equatorial ionospheric electric fields during magnetospheric

disturbances: local time/longitude dependences from recent EITS campaigns. *J. Atmos. Sol. Terr. Phys.*, 57:1065–1083, 1995.

[99] M. A Abdu, J.W.MacDougall, I.S. Batista, J. H. A. Sobral, and P. T. Jayachandran. Equatorial evening prereversal electric field enhancement and sporadic E layer disruption. A manifestation of E and F region coupling. *J. Geophys. Res.*, 108:A6, 1254, doi:10,1029/2002JA009285, 2003.

[100] J. H. Sastri. Equatorial Ionosphere-Thermosphere System During Geomagnetic Storms. *Geophysical mongraph series.*, 142:185–203, 10.1029/142GM16, 2003.

[101] J. Guo, X. Feng, P. Zuo, J. Zhang, Y. Wei, and Q. Zong. Interplanetary drivers of ionospheric prompt penetration electric fields. *J. Atmos. Sol. Terr. Phys.*, 73:130–136, 2011.

[102] A.S. Pavlov, S. Fukao, and S. Kawamura. F -region ionospheric perturbations in the low-latitude ionosphere during the geomagnetic storm of 25-27 August 1987. *Ann. Geophys.*, 22:3479–3501, SRef–ID: 1432–0576/ag/2004–22–3479, 2004.

[103] G.M. Lindsay, C.T. Russell, and J. G. Luhmann. Coronal mass ejection and steam interaction region characteristics and their potential geomagnetic effectiveness. *J. Geophys. Res.*, 100:A9, 16999–17013, 1995.

[104] M. H. Denton, J. E. Borovsky, R. M. Skoug, M. F. Thomsen, B. Lavraud, M. G. Henderson, R. L. McPherron, J. C. Zhang, and M. W. Liemohn. Geomagnetic storms driven by ICME- and CIR-dominated solar wind. *J. Geophys. Res.*, 111:A07S07, doi:10.1029/2005JA011436, 2006.